UNIVERSITAT DE BARCELONA

Radar-based nowcasting of severe thunderstorms:

A better understanding of the dynamical influence of complex topography and the sea

Anna del Moral Méndez

Ph.D Thesis

Radar-based nowcasting of severe thunderstorms: A better understanding of the dynamical influence of complex topography and the sea

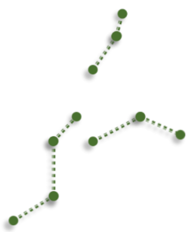

Author

Anna del Moral Méndez

Universitat de Barcelona

Radar-based nowcasting of severe thunderstorms: A better understanding of the dynamical influence of complex topography and the sea

Memòria presentada per optar al grau de doctor per la Universitat de Barcelona

Programa de doctorat en Física

Autora:
Anna del Moral Méndez

Directors:
Dr. Tomeu Rigo Ribas
Dra. María Carmen Llasat Botija
Tutor:
Dr. Alberto Manrique Oliva

Dept. de Física Aplicada

Facultat de Física

Barcelona, Maig del 2020

Universitat de Barcelona

This Ph.D. dissertation has been carried on under the framework of a Teaching and Research Assistant fellowship (*Ajut en Docència i Recerca*) funded by the University of Barcelona (UB). It also has been partially based upon work done under an Advanced Study Program grant, supported by the National Center for Atmospheric Research, which is a major facility sponsored by the National Science Foundation under Cooperative Agreement No. 1852977. In this sense, any opinions, findings and conclusions or recommendations expressed in this material do not necessarily reflect the views of the National Science Foundation. Finally, the outreach of the present work in international and national conferences and peer-review publications have been also sponsored by the Spanish projects HOPE (CGL2014-52571-R) and M-CostAdapt (CTM2017-83655-C2-2-R) of the Ministry of Economy, Industry and Competitiveness (Spanish Government), and by the Water Research Institute of the UB (*Institut de Recerca de l'Aigua*, IdRA).

Agraïments

"It is not knowledge, but the act of learning, not possession but the act of getting there, which grants the greatest enjoyment."

– Carl Friedrich Gauss

Aquest llibre conté un treball i uns resultats que han estat elaborats gràcies a l'ajut professional i emocional de molta gent durant aquests darrers quasi sis anys i a qui vull agrair l'acompanyament en aquest camí. Sobretot en el context actual en el que ens trobem mundialment, de confinament, degut a la pandèmia del COVID-19. Aviat tot passarà i ens podrem tornar a abraçar.

Primer, vull agrair als qui em van embarcar en aquesta aventura, als qui van confiar en mi quasi amb els ulls tancats des del principi i els qui em van obrir les portes del seu grup de recerca: els meus supervisors *Carme Llasat* i *Tomeu Rigo*. Gràcies per fer-me créixer professional i personalment, per descobrir-me l'apassionant món de la recerca i de la divulgació, pel suport en els moments durs, entenent els temps, i per l'esforç ajudant-me a recórrer el món tot i comptar amb limitats recursos.

I also need to mention all the people that gave me the incredible professional experiences I have enjoyed between 2018 and 2019. To *Karen Kosiba* and *Joshua Wurman* for giving me the amazing opportunity to join the CSWR team during the RELAMPAGO field campaign in 2018, making some of my childhood dreams come true: chasing tornadoes and a hurricane, and working with mobile radars. To *Rebecca Haacker* and the ASP group at NCAR, for awarding me with one of the 2018 grants and making possible my visit at NCAR. To my host *Tammy Weckwerth*, who opened me the doors to work with her without even knowing me, and helped me unconditionally during my stay. For contributing to my professional growth during these last Ph.D. months, and for allowing me to keep learning by joining her team as a future postdoctoral fellow. Of course, I need to thank all the new friends that have become my family away from home in the last year: the CSWR, the "Gophers", the NCAR family and the Boulder friends.

Haig d'agrair també enormement al meu grup de recerca, GAMA, i als "DamNyam", als "Meteofreaks", informàtics i la secretaria de l'antic departament d'Astronomia i Meteorologia. Als qui hi eren a l'inici i als qui han estat al final. Amb vosaltres ha estat un plaer anar a treballar. M'heu demostrat que no només tinc companys de feina sinó amics, i heu fet que el dia a dia fos una alegria al vostre costat. Hem compartit pastissos, celebracions, vermuts, dinars i ens hem ajudat en els moments difícils. En especial, vull agrair a la *Yolanda*, el *Jordi*, l'*Oriol*, l'*Enric*, el *Raül*, la *Montse* i el *Joan*, per haver-me ajudat tant, en molts i molts moments. Per donar-me els millors consells i per estar sempre disponible tant sols trucar a la porta. To *Wael*, the new "MeteoFreak", who demonstrated me that you can meet new people in conferences and become real friends. Thank you for giving me support in really crucial moments of this Ph.D. trip and for connecting Damascus and Barcelona through our friendship. I a l'*Aitor*, que després de que GAMA ens unís quasi per casualitat, s'ha convertit en un amic i un referent per mi en el món de la ciència.

Per descomptat, als meus imprescindibles. A la *Maria*, per no deixar-me defallir, per ser la meva cervesa i el descobriment de Barcelona dels divendres, pels dinars i sopars de la volta al món, un "roadtrip" per Portugal i desenes de congressos. Perquè això no hagués estat el mateix sense ella. A la *Patri*, que sempre ha estat disponible a toc de trucada. Que ha estat un pilar en tot aquest camí i desde els inicis. De la que he après infinites coses, i perquè les seves abraçades i paraules han estat pura medicina al llarg d'aquests anys. A la *Coral*, la *Mari*, l'*Abigail* i als "Físics". Per haver-me acompanyat fins i tot en la distància, per haver cregut més en mi que jo mateixa, per ser-hi sempre i per fer que cada retrobament fos com si no passés el temps. Per donar-li valor a la paraula amistat.

A mis abuelos, que quizás ya no se acuerdan, pero se emocionaron conmigo en los inicios. Porque sentí su orgullo en sus miradas. Porque deberían ser eternos. A mi extensa familia, pero sobretodo a mis primos, *Marc*, *Carmen*, *Yolanda* y *Núria*, por salvarme tantas veces. Porque han sido oxígeno, colchón y soporte. Por su paciencia, los vinos, los cines y las charlas. Y a mis dos primos "peques", *Pau* y *Adam*, porque su interés por lo que hacía y sus preguntas han mantenido en mí la curiosidad para seguir mirando al cielo.

To McKenna, who has ridden this past year with me, teaching me so much about science and life. For all the Chili, the beers, the guitar songs on the porch, the cookies, the creek walks, the Friday horror movies and the silent hikes that have helped me in challenging times during this last stage of the Ph.D. Thank you for being part of my laughs and my tears. For being my home in Boulder and for holding my hand in the distance.

Y para acabar, gracias a mi gato *Otto*, y a *Mickey*, nunca en el olvido. Por comerse mis apuntes y dormir a mi lado mientras escribía. Porque su ronroneo ha sido siempre mi gran compañía. Y por supuesto, GRACIAS, mamá, papá y Ferran, por ser mis raíces, mis ramas y mi nido. Esto no habría sido posible sin vosotros. Porque habéis sufrido y disfrutado TODO conmigo. Por hacerme soñar, por cogerme al caer, por no dejar que me de por vencida, por celebrar las victorias conmigo, y llorar las derrotas unidos. Por quererme en el error y en el acierto y por volar conmigo en Argentina y en Estados Unidos. Porque esto es tan vuestro como mío.

Abstract

Natural disasters of hydro-meteorological origin (floods and severe weather) are the biggest risk worldwide (71.6 % of the total, according to 2017 data from the EMergency events DATabase, EM-DAT). These disasters have resulted in a total of $1,980 trillion in economic losses and more than 880,000 deaths worldwide in the period 1998-2017. In Catalonia (NE of the Iberian Peninsula), different episodes of severe weather (heavy rains, hailstorms, strong convective winds and /or tornadoes) and flash floods occur each year, resulting, as well, in major damage to property, large losses in agriculture, and unfortunately, also loss of human lives. Besides, recent studies show that the current accused conditions of global warming can significantly impact factors triggering these storms, making them more intense or lasting, especially in the Mediterranean area. To reduce the impact of these phenomena and consequently the aforementioned figures, we need to improve early warning systems and short-term forecasting, along with the monitoring of the meteorology causing these phenomena. These tasks entail the need to gain ithorough knowledge of severe thunderstorm dynamics, which can often be considered out of the ordinary in terms of their characteristics: their duration, intensity, or the direction in which they move. While it should be noted that there are numerous studies on severe weather or floods, there are no studies that deal in-depth with the dynamics of such storms to improve the tracking and short-term forecasting.

In this context, the main objective of the present thesis is to enhance the knowledge of severe thunderstorm dynamics and how to improve their identification and monitoring in real time, to help prevent their surface effects on the citizens. The study addresses an unsolved problem regarding the anomalous movement of these thunderstorms (splitting or merging, stationarity, unexpected changes in direction, etc.), as it becomes a great challenge to predict their evolution in the next few hours, and therefore its impact.

To achieve these goals, the region of Catalonia has been chosen as the area of study for this analysis. Its proximity to the Mediterranean Sea and complex to-

pography are often key factors in varying the weather at a local scale, almost at the municipality level. There is also the advantage of having good radar coverage, which will be an essential tool for characterizing storms.

We first propose a methodology that identifies potentially convective days from daily cumulative rainfall fields, selects them to search for thunderstorms and determines if their propagation is anomalous (del Moral et al., 2017). This has helped us to analyze a large amount of data in a short time (2,920 daily precipitation fields), finding that the area with the highest convective activity in the period 2008-2015 in Catalonia was located in the eastern Pre-Pyrenees, due to the possible creation of a convergence line thanks to the topography and the sea. It has also been identified that there are more convective structures with possible anomalous propagation in summer and spring, with the main patterns being the V- or U-shape (splitting/merging), circular (stationary) and elongated (long-lasting thunderstorms).

Once our study sample has been defined, an algorithm has been developed to improve the identification and tracking of these thunderstorms, especially those with anomalous propagations (del Moral et al., 2018b). The keys of the improvement have been based on proposing new techniques in the three main algorithm modules; 2D and 3D identification, and tracking. The algorithm, which is currently being optimized for future operative functionality, incorporates a pre-processing stage, two filterings with seven reflectivity thresholds, an overlay-based volumetric cell construction technique, and tracking of thunderstorms between consecutive radar images based on size and intensity thresholds. Also, it incorporates warnings before possible cell splitting or merging. The aforementioned changes have shown that the algorithm can faithfully reproduce storm life cycle, correctly identify in advanced anomalous cell propagation, and correctly distinguish storms in highly dense convective situations (several cells together that can make it difficult to distinguish the individual ones).

The algorithm has been verified first over 30 severe weather cases, proving that it can identify anomalous movements with a mean 30-min lead-time, being the splitting, the easiest movement to identify, since the storms show a pattern of splitting beginning at high and spreading to low levels (del Moral et al., 2018a). It has also been demonstrated a good ability to not only identifying these movements but also separate cases with and without anomalous propagation. On the other hand, the algorithm has demonstrated a good performance in cases of heavy rainfall on the coast. In this case, the analysis has been done in a flood-prone area of touristic interest (coast of Tarragona, in particular, Salou). It is identified that storms are usually organized in convergence lines in front of the coastline, and that topography and the sea play a very important role, whether affecting the storm movement, the time of exposure, or the amount of precipitable water causing flash floods (del Moral et al., 2020a).

Finally, it has been introduced the multiple-Doppler technique, and more specifically the dual-Doppler technique (obtaining dynamic variables from purely radar observations within the thunderstorms themselves). This technique is usually applied in field campaigns in the United States, since it allows getting complete information of the internal dynamics of a thunderstorm, without the need of running idealized models. For the first time, and thanks to the geographical configuration of the Radar Network of the SMC, the XRAD, this technique is applied in Catalonia to investigate the local topographic influence on the evolution and organization of severe thunderstorms (del Moral et al., 2020b), being also the first time applied in a South European country. It is demonstrated that the complexity and sudden changes of elevation in local and small areas, change and/or amplify the wind flow inside and near thunderstorms, modifying completely their life cycle and their possible interactions with neighbor cells (for instance, amplifying the cold pool or rear gust front that helps to generate new cells, among other factors). It is also shown that this qualitative leap forward into the storm-scale dynamic knowledge can improve the nowcasting techniques, and therefore, the early warning systems in the future.

In conclusion, the results reaffirm the thesis that anomalous thunderstorm propagations are evidence of severe weather events, and that complex topography, as well as the maritime influence, play a very important role in their dynamics and life cycle. For instance, it has been detected the internal patterns within thunderstorms' dynamics, pointing out the influence of high levels during a splitting movement. Besides, improving thunderstorm-scale knowledge helps to better forecast their evolution and potential impact on society. In this case, following the same example of a thunderstorm splitting, the detection of the precursor patterns can be an essential tool in the future in surveillance operative tasks. Finally, thanks to the exclusive use and development of open-source tools and software, it is demonstrated an important science application component, as well as a knowledge transfer of the research performed, and its insertion into the development of new technologies.

Resum

Els desastres naturals d'origen hidro-meteorològic (inundacions i temps sever) constitueixen el major risc a nivell mundial (71.6 % sobre el total, segons dades actualitzades l'any 2017 del EMergency events DATabase, EM-DAT). Aquest tipus de desastres han causat un total de 1,980 bilions de dòlars en pèrdues econòmiques i més de 880,000 morts arreu del món en el període 1998-2017. A Catalunya (NE de la Península Ibèrica), cada any es succeeixen diferents episodis de temps sever (pluges intenses, pedregades, vents forts d'origen convectiu i/o tornados) i inundacions, provocant també danys importants en béns materials, pèrdues quantioses en l'agricultura, i malauradament, també pèrdua de vides humanes. A més, estudis recents demostren que les condicions cada cop més acusades d'escalfament global, poden impactar de manera notòria en algun dels factors desencadenants d'aquest tipus de tempestes, fent-les més intenses o duradores, especialment a l'àrea de la Mediterrània. Per reduir l'impacte d'aquests fenòmens i conseqüentment les xifres esmentades, és necessari millorar els sistemes d'alerta primerenca a molt curt termini, així com la monitorització dels sistemes meteorològics causants d'aquests fenòmens. Aquesta tasca comporta la necessitat de conèixer en profunditat la dinàmica de les tempestes que donen aquest temps advers, i que sovint es poden considerar fora de la normalitat pel que fa a les seves característiques, ja sigui per la seva durada, intensitat, o la direcció en què es mouen. Si bé cal dir que existeixen nombrosos estudis sobre temps sever o inundacions, no hi ha estudis que tractin en profunditat la dinàmica d'aquest tipus de tempestes i la millora de la seva predicció a molt curt termini i seguiment.

En aquest context, l'objectiu principal d'aquesta tesi doctoral es millorar el coneixement profund de la dinàmica de les tempestes severes, la seva identificació, predicció a molt curt termini, i monitoratge en temps real. Assolir aquest objectiu implica millorar la prevenció dels seus efectes en superfície. La tesi aborda una problemàtica encara no resolta sobre la propagació anòmala d'aquestes tempestes (partició o junció, estacionarietat, canvis bruscos de direcció, etc.), que esdevé un

gran repte a l'hora de pronosticar-ne la seva evolució en les properes hores, i per tant, el seu impacte.

Per assolir aquests objectius, s'ha triat Catalunya com a regió d'estudi. La seva proximitat al Mar Mediterrani i la complexa topografia, sovint esdevenen factors claus resultants en una meteorologia variada quasi a nivell de municipi. A més hi ha l'avantatge de disposar d'una bona cobertura radar, que serà l'eina essencial per la caracterització de les tempestes.

En primer lloc, s'ha proposat una metodologia que permet identificar les situacions potencialment convectives a partir de camps de precipitació acumulada diària, seleccionar aquests per identificar les tempestes i determinar si el seu moviment és anòmal (del Moral et al., 2017). Això ha ajudat a poder analitzar una gran quantitat de dades en poc temps (2,920 camps de precipitació diària), trobant que la zona amb major activitat convectiva en el període 2008-2015 a Catalunya es situa en el Pre-Pirineu oriental, degut a la possible creació d'una línia de convergència, gràcies a la complexa topografia i la proximitat al mar. També s'ha identificat que hi ha més estructures convectives amb possible propagació anòmala a l'estiu i la primavera, essent els principals patrons trobats els de forma en V o U (partició/junció), el circular (estacionarietat) i l'allargat (tempestes de gran durada).

Un cop definida la nostra mostra d'estudi, s'ha procedit a desenvolupar un algorisme que permeti millorar la identificació i seguiment d'aquestes tempestes, sobretot quan es tracta d'aquelles amb moviment anòmal (del Moral et al., 2018b). Les claus de millora s'han basat en proposar noves tècniques en els tres mòduls principals; identificació 2D, 3D ,i seguiment. L'algorisme, que actualment s'està optimitzant per a una futura posada en operatiu, incorpora un pre-processament de les dades, un segon filtratge amb set llindars de reflectivitat, una tècnica de construcció volumètrica d'estructures per superposició, i una connexió de tempestes entre imatges radar consecutives a partir de llindars de grandària i intensitat. A més, incorpora emissions d'alertes abans de possibles moviments de partició o junció de tempestes. Els canvis esmentats han demostrat que l'algorisme és capaç de reproduir amb més fidelitat el cicle de vida de les tempestes, identifica correctament particions i/o juncions per avançat i és capaç de distingir correctament tempestes en situacions amb alta densitat convectiva (moltes celÂ · les juntes que poden dificultar la identificació correcte individualment).

El funcionament de l'algorisme s'ha verificat sobre 30 casos severs, on s'ha demostrat que és capaç d'identificar moviments anòmals amb un marge de 30 minuts per avançat, essent el moviment més fàcil de detectar el de partició, ja que les tempestes mostren un patró de separació començant per nivells alts i acabant en els baixos (del Moral et al., 2018a). A més s'ha demostrat la bona habilitat en separar casos amb i sense moviment anòmal. D'altra banda, també queda palès el bon funcionament de l'algorisme sobre casos de pluges intenses a la costa. En aquest cas, en una zona d'alt risc d'inundació i de gran interès turístic (costa de Tarragona, en concret, Salou), s'identifica que les tempestes solen organitzar-se en línies de convergència davant la costa, i es demostra que la topografia i el mar juguen un paper molt important, ja sigui afectant-ne el moviment, el temps d'exposició de la zona, o l'aigua precipitable, causant inundacions sobtades (del Moral et al., 2020a).

Finalment, s'ha introduit la tècina *multiple-Doppler*, més en concret la *dual-Doppler*, és a dir, l'obtenció de variables dinàmiques dins de les pròpies tempestes a partir, purament, d'observacions radar. Aquesta tècnica, usada sovint en campanyes experimentals als Estats Units, permet tenir informació completa a alta resolució de la dinàmica interna de les tempestes, sense haver de recórrer a models idealitzats. Per primer cop, i gràcies a la configuració geogràfica de la Xarxa de Radars del SMC, la XRAD, s'aplica aquesta tècnica a Catalunya per investigar la influència topogràfica local en l'evolució i organització de tempestes severes (del Moral et al., 2020b). Es demostra que la complexitat i canvis sobtats de terreny en àrees petites, modifica i/o amplifica el camp de vent propi de les tempestes, variant-ne completament el cicle de vida i les possibles interaccions amb tempestes veïnes (per exemple, amplificant el front de ratxa que afavorirà crear noves tempestes, entre d'altres factors). Queda palès que, amb aquest salt qualitatiu en conèixer la dinàmica a escala de tempesta, es poden millorar les eines de pronòstic a temps real i, per tant, les alertes per a la ciutadania en un futur proper.

En conclusió, els resultats reafirmen la tesi de que els moviments anòmals de tempestes són una evidència de temps sever i que la complexa topografia, així com la influència marítima juguen un paper molt important en la dinàmica i cicle de vida d'aquestes. Per exemple, s'han detectat els patrons interns dins de la dinàmica de les tempestes, assenyalant la influència dels nivells alts durant un moviment de partició. A més, queda de manifest que una millora del coneixement a escala de tempesta, ajuda a pronosticar millor la seva evolució i possible impacte en la societat. En aquest cas, seguint el mateix exemple de partició de tempestes, la detecció dels patrons precursors pot ser una eina essencial en el futur en les tasques operatives de vigilància. Finalment, gràcies a l'ús i desenvolupament exclusiu d'eines i programari de codi lliure en la present tesi, es demostra la important component d'aplicació i transferència de coneixement de la recerca duta a terme, així com la seva inserció en el desenvolupament de noves tecnologies.

List of Acronyms

2D	2-Dimensional
3D	3-Dimensional
AEMET	Agencia Estatal de Meteorología (Spanish Meteorological Agency)
AGL	Above Ground Level
ASL	Above Sea Level
AWP	Adverse Weather Phenomena
AWS	Automatic Weather Station
CAPE	Convective Available Potential Energy
CAPPI	Constant Altitude Plan Position Indicator
CCS	Consorcio de Compensación de Seguros (Spanish insurance compensation consortium)
CDV	Creu Del Vent radar
CEDRIC	Custom Editing and Display of Reduced Information on Cartesian space
CG	Cloud-to-Ground lightning
CI	Convective Initiation
CIRA	Cooperative Institute for Research in the Atmosphere
COW	C-band doppler On Wheels (radar)
CSR	Clutter-to-Signal Ratio
CSU	Colorado State University
CSWR	Center for Severe Weather Research
DOW	Doppler On Wheels (radar)
DPS	Daily Precipitation Structures

DWD	Deutscher Wetterdienst (German Weather Service)
E	Elliptical (structures)
EF	Enhanced Fujita
EHIMI	Hydrometeorological Integrated Forecasted Tool
EM-DAT	EMergency events DATabase
EOL	Earth Observing Laboratory
ERAD	European Conference on RADar in Meteorology and Hydrology
ETITAN	Enhanced Thunderstorm Identification, Tracking, Analysis and Nowcasting
FFD	Forward-Flank Downdraft
FRACTL	Fast Reorder and CEDRIC Technique in LROSE multi-Doppler retrieval
GAMA	Grup d'Anàlisi de situacions Meteorològiques Adverses (Group of Analysis of Adverse Meteorological Situations)
GPRS	General Packet Radio Service
HAL	Hurricanes At Landfall
HP	High Precipitation
HTOP	Height of the echo TOP (minimum 30 dBZ)
HTOP40	Height of the 40 dBZ echo TOP
IC	Intra-Cloud lightning
IOP	Intensive Operations Practice
KED	Kriging with External Drift
LAT	Latitude
LFC	Level of Free Convection
LJ	Lightning Jump
LM	Left Mover (storm)
LMI	La Miranda radar
LON	Longitude
LROSE	Lidar and Radar Open Software Environment
M2D	Multiplicity of 2D structures
MA	Massa d'Aigua precipitable (Precipitable Water Content)

MAP	Mesoscale Alpine Program
MCS	Mesoscale Convective System
MDF	Magnetic Direction Finding
METAR	METeorological Aerodrome Report
MUSCAT	MUltiple-doppler Synthesis and Continuity Adjustment Technique
NAM	Non-Anomalous Movement
NASA	National Aeronautics and Space Administration
NCAR	National Center for Atmospheric Research
NCORE	Number of pixels of the cell CORE
NE	Non-Elliptical (structures)
NOAA	National Oceanic and Atmospheric Administration
NPA	Neighbouring Pixel Adjacency
NPC	Non-Potentially Convective
NPIX	Number of PIXels
NR	No Rain
NWP	Numerical Weather Prediction
PBE	Puig Bernat radar
PC	Potentially Convective
PCS	Potentially Convective Structures (PCS)
PDA	Puig d'Arques radar
PI	Principal Investigator
PM	Possible Merging
POD	Probability Of Detection
PODs	Portable Observation Devices
POFD	Probability Of False Detection
PPI	Plan Position Indicator
PRF	Pulse Repetition Frequency
PS	Possible Splitting
PSS	Peirce's Skill Score
QPE	Quantitative Precipitation Estimate

RELAMPAGO	Remote sensing of Electrification, Lightning, And Mesoscale/microscale Processes with Adaptive Ground Observations
RM	Right Mover (storm)
RMSE	Root Mean Square Error
ROI	Region Of interest
SAMURAI	Spline Analysis at Mesoscale Utilizing Radar and Aircraft Instrumentation
SCIT	Storm Cell Identification and Tracking
SMC	Servei Meteorològic de Catalunya (Meteorological Service of Catalonia)
SNR	Signal-to-Noise Ratio
SQI	Signal Quality Index
SR	Succes Ratio
STAP	Servicio de Técnicas Aplicadas (Service of Applied Techniques)
TITAN	Thundestorm Identification, Tracking, Analysis and Nowcasting
TOA	Time Of Arrival
TWIRL	Tornado Winds from In-situ and Radars at Low-levels
UTC	Universal Time Coordinated
UTM	Universal Transverse Mercator
WMO	World Meteorological Organization
WRF	Weather Research and Forecasting
WTOP7	Warning of HTOP greater than 7 km
XDDE	Xarxa de Detecció de Descàrregues Elèctriques (Lightning Detection Network from the Meteorological Service of Catalonia)
XEMA	Xarxa d'Estacions Meteorològiques Automàtiques (Automatic Meteorological Station Network form the Meteorological Service of Catalonia)
XRAD	Xarxa de RADars (Radar Network from the Meteorological Service of Catalonia)
ZMAX	MAXimum reflectivity (Z)

Contents

Part I
INTRODUCTION

1

Motivation and Introduction

Climate-related natural disasters represent a major risk worldwide. Between the period 1998-2017, 91 % of all disasters were caused by floods, storms, droughts, heatwaves and other extreme events (international EMergency events-DATabase, EM-DAT, http://www.emdat.be/), representing millions of losses of human lives and billions in people injured, displaced or homeless around the world. In concrete, natural disasters of hydro-meteorological origin, this is, *adverse weather*, constitute the biggest risk of all. Adverse Weather Phenomena (AWP) are any meteorological phenomena with intensity, frequency, or extension markedly bigger or higher from normal climatic conditions, as explained in Llasat (2009) and based on the World Meteorological Organization (WMO) 1995 proposal. This type of events has resulted in a total of $1,980 trillion in economic losses and more than 880,000 deaths worldwide in the period 1998-2017 (Wallemacq, 2018), and represented 4,613 deaths, 53.6 million people affected, and $90.5 billion in economic losses only in 2018 (Cred, 2019).

The Mediterranean region follows the same pattern in natural hazards as in the rest of the world, being a major risk also those events related to floods. In concrete, due to soil erosion, among other factors, the Mediterranean area becomes a hotspot for flood risk within all Europe (Panagos et al., 2015). This pattern especially increases in the coastline, where the major concentration of the population is located, directly rising the vulnerability to natural hazards of these regions(Eurostat, 2016). More in concrete, the EM-DAT database itself lists €85 billion in damages related to river floods and flash floods since 1900 in the countries surrounding the Mediterranean Sea (Gaume et al., 2016). Also, Petrucci et al. (2019) identify 812 fatal floods with 2,466 fatalities for the period 1980-2018 in eight Mediterranean countries plus the Czech Republic, of which most of them occurred outdoors.

Nowcasting (short-term forecasting) of convective cells producing adverse weather depends on fast and reliable identification and diagnosis tools to provide clear and important information to aid operative forecasters in their decision-making process. The advances in high-resolution Numerical Weather Prediction (NWP) models have greatly enhanced the forecast of major events in the last decades (see, for instance, hurricane forecasting, Willoughby et al., 2007). However, for more local and short-lasting phenomena, as in the case of the northwestern Mediterranean coast (Llasat et al., 2016), products derived from weather radars have become a common instrument in the convective research and operative communities. In particular, either solely radar-based nowcasting or in combination with auxiliary tools such as lightning or vertical atmospheric profiles, among others, have been demonstrated to be good diagnostic and analysis tools able to provide a significant amount of information about precipitating structures with high temporal and spatial resolution (López and Sánchez, 2009; Berenguer Ferrer et al., 2015; Sempere-Torres et al., 2016; Corral et al., 2019; Hu et al., 2019; Shi et al., 2019). These integrated systems enhance the ability to analyze and greatly improve the forecast skill of adverse weather phenomena early-warning systems.

Nevertheless, there still exists a lack of a complete understanding of the local and internal dynamics of these thunderstorms. The research community is working towards identifying the features controlling storm severity while also investigating interactions between thunderstorms and how these interact with their surrounding environment (e.g. topography, mesoscale boundaries, sea-land interaction), which may influence the evolution, duration, direction, or area affected (del Moral et al., 2018b). Furthermore, in a quickly changing climate encompassing global warming scenarios, with increased adverse weather events in coastal areas, it is necessary to perform quasi-individual studies in local regions with potential high-risk factors, since interactions between social, economic, hydrological and meteorological fields are starting to play a major role.

Within the definition of adverse weather, it is included *severe weather* phenomena, which are usually caused by more local thunderstorms. This is the nature of most of the events affecting the northwestern Mediterranean, and therefore are the study target on which is based the entire thesis. According to the WMO, a severe weather event is "*any atmospheric condition potentially destructive or hazardous for human beings*". In particular, it is referred to as those events associated with "*extreme convective weather (tropical cyclones, tornadoes, severe* *thunderstorms, squalls, etc.) and with storms of freezing precipitation or blizzard conditions*" (W.M.O, 1992). This definition contains phenomena and thresholds following the local climatology. This is the case of, for instance, the area of interest of the current project, Catalonia (see Section 4.1 for more detail), where the definition of severe weather implies a thunderstorm event with hailstones ≥2 cm in diameter, wind gusts ≥25 m s^{-1} and/or tornadoes (Farnell et al., 2017). This may be also accompanied by excessive rainfall in short periods, resulting in flash floods (Martín et al., 2014; Llasat et al., 2016; Cortès et al., 2017). Severe weather is usually associated with *deep moist convection* (especially hail and wind-related events). This type of convection is likely resulting from the product of three main environmental ingredients: instability, associated with high Convective Available Potential Energy (CAPE); moisture; and a lifting mechanism (Doswell III et al., 1996; Ramis et al., 1999). Severe thunderstorms present a vertical updraft more intense than usual and a strong vertical wind shear (i.e. Bunkers, 2002; Markowski et al., 2003; Markowski and Richardson, 2011; Dennis and Kumjian, 2017). However, severe phenomena can also occur in low shear or CAPE environments if it exists a forced lifting mechanism, which will help to raise the air parcels to a level on where these reach a positive buoyancy state and can lift naturally. These may imply, for instance, upscale growth and convection organization, which can generate outflow boundaries that may enhance thunderstorm-scale dynamics. Other mechanisms may be mesoscale thermal boundaries (frontal passages) or topography (upslope flow), among other (see, for instance, Grasmick et al., 2018; Mulholland et al., 2019; Weckwerth et al., 2019).

1.1 Fundamentals of thunderstorm initiation, organization, and propagation

The nature phenomena causing severe weather are thunderstorms, which can last from several minutes to hours (usually from 30 min to 2 h). Thunderstorms present three stages during their life cycle, mainly differentiated by the direction of the vertical wind flows and the effects on the surface (Byers and Braham, 1949; Doswell III, 1985). The first stage is the *cumulus* or *developing* phase, which is characterized by a predominant updraft (positive – away from the surface, vertical wind flow) that makes the small hydrometeors to grow as droplets. This is done by means of the rising of a moist air parcel to its level of condensation. The growth lasts until the particles have the weight needed to cancel the upward force, coinciding with the beginning of the *mature* phase, which is the second phase. In this second phase, it begins the precipitation of hydrometeors, creating a downdraft (negative – towards the surface, vertical wind flow) that counteracts the updraft. This triggers an evaporation process that produces the cooling of the air temperature and accelerates the downward motion. Once the downdraft reaches the surface, a relatively small mass of cold air and a gust front are usually generated. This is the phase where the thunderstorm becomes severe and/or present complex dynamic features and interactions that may influence its intensity, duration, and propagation. Finally, in the *dissipation* phase, the downdraft predominates and disappears, in a relatively quick period of time (Wilhelmson, 1974; Doswell III, 1985; Martín et al., 2007).

Every pair of updraft and downdraft recognized in weather radar images, is what we call *convective cells*, the smaller entity to define a thunderstorm (Wilk et al., 1979; Weckwerth and Wakimoto, 1992; Zipser and Lutz, 1994). Depending on how a cell organizes and evolves with the environmental shear and instability we can distinguish three types of thunderstorms; single cell, multicell or supercell. A *single cell* is a thunderstorm that consists of one single isolated updraft and with a weak gust front unable to initiate new cells. The bulk wind shear between 0 and 6 km (the layer that differentiates the most between cell organization) is usually below $10\,\mathrm{m\,s^{-1}}$. This kind of thunderstorm is usually referred to as *ordinary* or *pulse* thunderstorm (Miller and Mote, 2017), and the lifetime is approximately 30 to 60 min. *Multicell* thunderstorms (Mazur et al., 1986; Lin et al., 1998; Rigo and Pineda, 2016) are a form of single-cell organization in which the original cell gust front (mature stage of old cells) is strong enough to lift again air parcels to their Level of Free Convection (LFC), and therefore to form new thunderstorms. These are usually developed in environments with 0-6 km bulk shear between 10 to $20\,\mathrm{m\,s^{-1}}$. Due to their organization, these tend to last longer, and sometimes may organize as even major systems covering extended areas (more than $100\,\mathrm{km^2}$) in what is named as Mesoscale Convective Systems (MCS, Parker and Johnson, 2000; Schumacher and Johnson, 2005; Houze Jr, 2018). Finally, *supercells* are, as their name indicates, the “mother” of all the thunderstorms, as they have the more complex dynamic configuration and they can last up to several hours (commonly 1-4 hours, but some observations indicate even longer). Markowski and Richardson (2011), describes this type of thunderstorm as containing a deep mesocyclone; a region of vertical vorticity with a width of 3 to 8 km, and a depth of approximately half that of the updraft. This mesocyclone is usually persistent enough to make an air parcel to go through the entire updraft, which takes approximately 20 min, and is a clear sign of possible severe weather, especially tornadoes and large hailstones.

According to Cotton et al. (2011), the displacement of a thunderstorm is basically composed of three types of movement: the *translation* (synoptic factors), the *forced propagation* (mesoscale factors), and the *auto propagation* (thunderstorm factors). These two last factors, from mesoscale and from the thunderstorm itself, may force the thunderstorm to present what we define in the present work as *anomalous propagation*, this is, unexpected movement patterns. In the present thesis the concept *anomalous propagation* and *anomalous movement* will be used in the same way, since some of these will be momentaneous (movement) and others will last for a longer period (propagation). This is observed when the movement performed by the thunderstorm does not follow the mean wind at the cores' altitude (i.e. sharp changes of direction, stationarity, splitting, merging, and trajectories opposite to the neighbor cells). Anomalous propagation usually takes place during the mature stage of the thunderstorm, and it is an indicator of thunderstorm severity. Although an erratic propagation may hamper the ability to forecast the path of the thunderstorm, it is a good signal of possible severe weather. For this reason, the identification of such propagation may help a forecaster to take a decision on which area is going to suffer severe weather phenomena, and therefore to help saving human lives and goods. Some of the well-known anomalous propagation patterns are, for instance, splitting supercells (Rotunno and Klemp, 1985; Bunkers et al., 2000; Weisman and Rotunno, 2000) and back building multicell systems (Bluestein and Jain, 1985; Houston and Wilhelmson, 2007), since these have been studied in research field campaigns mainly in the United States (Nesbitt et al., 2017; Peters et al., 2017; Houston et al., 2020, among others). However, the internal thunderstorm dynamics (the tilting of updrafts, or the creation of vorticity rolls and/or cold pools, etc.), coupled with mesoscale factors (i.e. orographic borders, sea boundaries, or thermal convergence lines), may trigger complex processes as, for instance, multicell systems evolving in supercells (Rigo and Pineda, 2016), or splitting process in non-supercell thunderstorms, which present a challenge in surveillance tasks (see Chapter 6 and Chapter 9).

1.2 Severe weather in Catalonia

Catalonia is a small region in the northeastern corner of the Iberian Peninsula. The complex topography (see Chapter 4, for more details) and the proximity to the sea, make this region prone to suffer severe weather frequently. This type of weather has been studied in many published climatology-based works (Ceperuelo et al., 2009; Llasat et al., 2010; Gayà et al., 2011; Farnell and Llasat, 2013; Rodríguez and Bech, 2018, among others), and other numerous analyses have focused on post-event research for particular cases (see, for instance, Homar et al., 2003; Llasat et al., 2003; Pineda et al., 2009; Bech et al., 2015; Rigo and Pineda, 2016). These events, especially hail-related and flash floods resulting from heavy precipitation, cause important economic losses in infrastructures, agricultural exploitations or human lives, due to their high frequency of occurrence. For instance, Aran et al. (2011) found that the yearly average economical losses produced only by hail events in the western area of Catalonia were of €15 million for the period 2000-2009. Cortès et al. (2018) show how between 1996 and 2015, the Spanish insurance company (Consorcio de Compensación de Seguros, CCS, 2018) paid more than €430 million in damages due to floods and flash floods, mostly related to heavy precipitation events. In the case of straight-line winds or tornadoes, the frequency of occurrence is lower. However, when these events affect densely populated areas, the economic impact can result even higher. That is the case, for instance, of the tornado outbreak that affected the Barcelona Airport on September 7, 2005, and which recorded €1.7 million only in the airport insurance claims (excluding the surrounding areas affectations or the cost of diverting, canceling and delaying commercial flights, Bech et al., 2007).

Despite the recent improvements in forecasting possible severe weather events in Catalonia, there are still some challenges to face in the operational nowcasting system, such a radar-based tracker capable to retrieve a more realistic life cycle of the thunderstorms, or capable of forecasting anomalous movements. Furthermore, even improving the nowcasting tools, it still exists a lack of knowledge of the dynamical processes within the storms and how the complex topography might modulate their behavior. The advances in the last years in the use of, for instance, near-real-time multiple-Doppler techniques with operational radar networks, the improvements achieved in complex terrain, or the increase in extreme events in the Mediterranean regions due to global warming, has provided the sufficient motivation and base for the study presented here.

2

Objectives and structure

The present thesis has been based on the main hypothesis, reached after the broad experience of researchers and forecasters in our region:

The complex topography and the proximity to the sea play a major role in mesoscale dynamics, impacting directly in thunderstorms producing severe weather phenomena.

However, there is still a lack of knowledge of thunderstorm-scale dynamics, which has motivated the entire thesis here presented. In this sense, and bearing in mind the known hypothesis mentioned above, the main objective of the present work has been established:

To advance in the knowledge of thunderstorm-scale dynamics in Catalonia (applicable also in other world regions), identifying the influence of complex topography and the sea in their life cycle, and especially in their propagation, as well as their capacity of producing severe weather, in order to improve the nowcasting of these thunderstorms and phenomena.

The objectives have been defined to solve the different stages that the present thesis has followed: identification of the current status of severe weather and anomalous propagation in Catalonia; improvement of current nowcasting tools; identification of the influence of topography and the sea in severe weather producing-thunderstorms in two different convective regimes (inland isolated thunderstorms and coastal convection); and storm-scale dynamical study with a new proposed technique and with case studies.

2.1 Specific objectives

Based on the main objective explained above, the following eight specific objectives have been established:

1. **To create a fast and reliable method to identify thunderstorm propagation patterns, to be applied not just in our region but also in areas where no weather radars are available.**

2. **To retrieve a climatology of thunderstorms occurrence and anomalous propagation in the area of Catalonia, to establish the main patterns in our region.**

3. **To improve the algorithm for identification and tracking of thunderstorms from the SMC. In concrete:**

    - To differentiate thunderstorm tracks when there is a high convective activity (cell clusters)
    - To retrieve more realistic thunderstorm life cycles, getting better continuity in shape and intensity.
    - To identify, in advance of occurrence, possible splitting of thunderstorms and/or merging processes.

4. **To verify the improved identification and tracking algorithm in different convection regimes: severe weather and coastal adverse weather.**

5. **To identify the main thunderstorm features and the influence of the topography and the sea over a touristic coastal area with a high occurrence of flash floods.**

6. **To identify how to adapt the early warning systems for flash floods in coastal areas for future global warming scenarios.**

7. **To explore the capabilities of an operative regional C-band radar network to retrieve dual-Doppler thunderstorm-scale winds in complex terrain.**

8. **To demonstrate the big impact of the topography in the dynamics, propagation, and severity of thunderstorms, and the variability of phenomena in local scales in a case study.**

The present thesis has been a collaborative effort between the GAMA team at the University of Barcelona and the Remote Sensing Unit at the SMC, and therefore the main purpose during all the process has been to keep the link between both the academic and the operative environments. It is for that reason that this work is framed with the purpose to get the applicability of the knowledge obtained in the research field and to improve the service to our society. For this reason, the algorithms and techniques here developed are based on the main foundation: the availability to be easily applied in the operative chain at the weather service. In this sense, the algorithms and the analyses conducted in all chapters, have been done with open source tools (R Core Team, 2019; Python Core Team, 2001; QGIS Development Team, 2009; LROSE Development Team, 2019), to be not just applicable at our weather service but also to be applicable in other areas that might consider our techniques interesting. Also, this allows the SMC not just to set up new tools without an economical cost, but also to open the door to improve them with open collaboration.

2.2 Structure of the thesis

The present Ph.D. thesis manuscript is structured in four different parts as it follows:

Part I: Introduction. The Introduction part describes the current state of adverse weather impact worldwide, and in concrete in the Mediterranean region, as well as it introduces the main challenges that the weather community is facing nowadays trying to better understand and forecast this type of events. It also covers the definition of the concept of "severe weather", as well as a review on thunderstorm initiation, dynamics, and propagation. All this is seen in Chapter 1. The current Chapter 2 lists the objectives that have been the main target to solve in the present thesis and the structure of the thesis (current section). Finally, Chapter 3, describes a review of the current status of the diagnostic techniques available to forecast such events.

Part II: Area of Study and data. This section, presented in Chapter 4, covers the region of study for the present thesis, Catalonia, and the data and instrumentation sources used in its development.

Part III: Results. This is the main section of the manuscript and is divided into four chapters that follow the specific objectives presented in the preceding lines. First, Chapter 5, presents the identification of anomalous propagation patterns in the area of Catalonia, with a technique that can be applied in regions where no weather radar is available. Chapter 6 describes the new radar-based identification and tracking algorithm for surveillance purposes, which is able to identify in advance if a split or merge process will occur. Chapter 7 presents the validation of the algorithm over 30 severe weather events that presented anomalous propagation patterns. A second application of the algorithm described in Chapter 6 is presented in Chapter 8; a study on a touristic coastal area prone to suffer flash floods. This study shows a deep analysis of the thunderstorm features and propagation, and the influence of the sea and the topography in order to adapt the Early Warning systems to face future global warming scenarios. Finally, Chapter 9 explores for the first time in a south-European country, dual-Doppler retrievals. It presents promising results by using the software within The Lidar Radar Open Software Environment (LROSE) project: the Spline Analysis at Mesoscale Utilizing Radar and Aircraft Instrumentation (SAMURAI, LROSE Development Team, 2019), with an operational radar network and with complex topography. It is explored more in deep a case presented in Chapter 6, and it is shown the impact of topography in storm-scale dynamics, and the complex evolution of a multicell storm evolving into two split supercells. The result from Chapter 5 to Chapter 8 are three published peer-review papers (del Moral et al., 2017, 2018b, 2020a), and an extended proceeding presented as a *keynote* at the 10th European Radar Conference (ERAD) in Ede, The Netherlands (del Moral et al., 2018a). A final paper, currently in preparation, is expected to be published with respect to the work of Chapter 9 (del Moral et al., 2020b).

Part IV: Conclusions. This final part is, as its name indicates, the concluding chapter of the Ph.D. thesis. It summarizes all the findings and challenges overcome in the present work. More in concrete, it shows the answers of the objectives that are proposed in this same chapter, it presents some advice and possible improvements on the operational nowcasting of severe weather events in Catalonia, as well as it describes future work that may be explored to answer some unsolved questions arisen in this work.

3

Studying and monitoring severe weather using Doppler radar: *State of the art* review

One of the most used instruments to study and monitor thunderstorms and their associated phenomena in real time is the weather radar. Weather radars are remote sensing instruments, this is, electromechanical systems able to obtain properties and information of an object without being physically in contact (AMS, 2020). More in concrete, a weather radar can detect the presence of hydrometeors (objects) in the atmosphere, by emitting electromagnetic energy, and receiving the backscattered echo (Meischner, 2005; Fabry, 2015). The latter, which is the power returned from the hydrometeors, is converted into what we call radar *reflectivity factor* or reflectivity, Z, and its measure in decibels (dBZ) (Schmidt et al., 2019). Reflectivity is the *moment* or quantity that is commonly displayed on radar images. It is the amount of backscattered transmitted power compared to a reference power density, usually taken at a distance of 1 m from the radar (Probert-Jones, 1962; Li and Kiang, 2005), and which allows the estimation of the precipitation rate (Marshall and Palmer, 1948). The azimuth ϕ, range, r, and elevation angle, ϵ, of the backscattered echoes are also obtained to locate the hydrometeor in space (Rauber and Nesbitt, 2018). Most of the weather services in developed countries nowadays use Doppler radars; by means of this effect properties (Doviak and Zrnic, 2014), they can retrieve the velocity of the hydrometeor when this is moving towards or against the radar. This moment, called *radial* or *Doppler velocity* is really important when monitoring severe thunderstorms since it will depict information about the propagation and some dynamics taking place (i.e. mesocyclones, convergence, wind gust fronts, etc.). The Doppler velocity, along with the reflectivity, will help the forecaster to take decisions in an operational environment. Another capacity that some more advanced radar networks have is the dual-polarization, this is, radars that are capable of distinguishing between the polarization phase of the emitted and received pulse. This type of radar is demonstrated to have a better performance in surveillance tasks than the single-polarization radar, since not only can retrieve other valuable information about the hydrometeors in severe thunderstorms, such as their size or composition, but it also allows to obtain different types of clear air echo returns, and other information in non-convective precipitation (see, for instance, Zhang et al., 2001; Keeler et al., 2000; Weckwerth et al., 2005). Although there exist multiple sources of errors to bear in mind when dealing with radar data (some of them explained in further sections), it is clear that the Doppler radar constitutes a basic instrument when studying and tracking in real time different weather phenomena, especially thunderstorms. In this sense, the weather radar is one of the fundamental instruments of every consolidated weather service, and it has been present in multiple research projects in the past 30 years (i.e. Geerts et al., 2017; Bodine and Kurdzo, 2018; Witze, 2018; Tessendorf et al., 2019).

3.1 Nowcasting

Nowcasting (short-term forecasting), constitutes the basis of severe weather warning operations (Hering et al., 2004; Brovelli et al., 2005; Roberts et al., 2006), and one of the most important techniques in research of severe phenomena. Although it exists numerous nowcasting techniques, including those based on Numerical Weather Prediction (NWP) models, complex topography or storm-scale interactions are some of the factors that hamper their operative surveillance tasks since they many difficulties in reproducing the interactions of these factors with a thunderstorm. This does not affect just on reproducing the location and intensity of thunderstorms in convection-allowing models but also the capability to get their fast-changing mesoscale-related interactions, which represent the main feature to nowcast possible severe weather phenomena. Because of this, remote sensing instrumentation, especially weather radar, results in a fundamental tool when it comes to dealing with complex severe weather events in areas with high spatial variability and a number of local phenomena, at least in the immediate period. Knowledge-based algorithms (based on human expertise), and especially those based in the extrapolation of radar echoes (not retrieving initiation and dissipation of thunderstorms from NWP), are what we call radar-based nowcasting techniques (Figure 3.1). The primary aim of these techniques is to identify, to track in real time, and to extrapolate the future path of a thunderstorm. They also allow us to retrieve rapidly and with acceptable accuracy, different thunderstorm valuable features, which help a forecaster in a decision-making process. Since the main body of the present work has been to develop different improvements in some modules of an extrapolation radar-based technique, in concrete a centroid-type tracker, we are going to focus only on this type of technique. For more detailed information on the other techniques, readers are referred to Wilson et al. (2004, 2010) and Kiktev et al. (2017), and their cited bibliography.

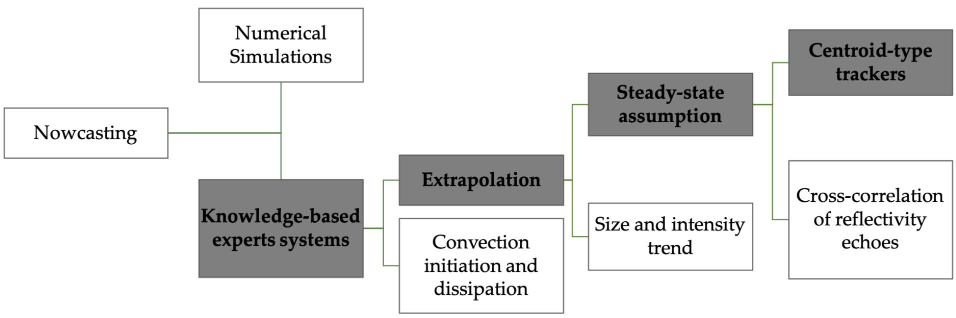

Figure 3.1: Main nowcasting techniques (Wilson et al., 1998). Grey boxes indicate the type of technique on which the present work is based on.

According to Wilson et al. (1998, 2004) the historical treatment of thunderstorm extrapolation techniques can be divided into two main groups: assuming no change in motion, size, and intensity (steady-state assumption) and, on the other hand, allowing changes based on past trends, although Tsonis and Austin (1981), for instance, proved that the latter doesn't necessarily improve the nowcasting techniques. Within the steady-state assumption algorithms, it can be found also two main groups depending on the way they track the identified thunderstorms: cross-correlation tracking, and centroid tracking and matching (Figure 3.1). The cross-correlation technique uses consecutive radar images to calculate the displacement vector between them. It then extrapolates the area of the thunderstorm to future images separated in time and takes the translation vector (motion at constant velocity) that gives the maximum correlation, resulting as the final echo displacement. This technique is really effective when it comes to nowcast convective precipitation embedded in stratiform systems, because of its capability to distinguish between both types of precipitation (see, for instance, Ligda, 1953; Kessler, 1966; Wilson, 1966; Rinehart, 1981; Novák et al., 2009; Berenguer and Zawadzki, 2009). However, it is not so efficient for identifying and tracking individual convective cells. The second methodology, the centroid tracker, is based on the identification and tracking of the centroid of every single cell within a convective system, obtaining not only two-dimensional information but also volumetric properties. This type of technique is most of the time unable to identify stratiform precipitation because it is focused on deep convection analysis. However, and also for the same reason, it becomes a powerful tool to diagnose in real time the potential severity of a thunderstorm, during severe weather surveillance tasks.

Two of the most famous centroid-trackers algorithms are the TITAN (Thunderstorm Identification, Tracking, Analysis, and Nowcasting, Dixon and Wiener, 1993), and the SCIT (Storm Cell Identification and Tracking Algorithm, Witt and Johnson, 1993), which has served as the basis for the project of the present research and are explained as follow. The TITAN algorithm is a real-time centroid-type tracker algorithm developed at the National Center for Atmospheric Research (NCAR), which is nowadays still operative (also available in the open-source Lidar Radar Open Software Environment, LROSE, project (`http://lrose.net`). This algorithm uses unique and fixed reflectivity and volume thresholds to define convective cells (minimum entity). Then, cells are tracked across consecutive radar scans, applying a combinatorial optimization technique (Papadimitriou and Steiglitz, 1998) plus a geometric algorithm (Preparata and Shamos, 2012), which allows dealing with splitting or merging thunderstorm processes. Based on the TITAN foundation, the Enhanced TITAN algorithm (Han et al., 2009) goes one step further and introduces a dual-threshold process during the convective cells' identification. This is followed by a growth and dilation operation (image processing) to avoid false mergers in events with a high amount of convective cells (i.e. cluster of cells embedded in a mesoscale system). Besides, it introduces an overlapping technique during the tracking module which, combined with a dynamic constraint-based combinatorial optimization method, handles possible violations of the maximum speed constrain when cells shapes change constantly and rapidly. The TITAN algorithm was introduced in Spain by the group of Meteorology of the University of León (ULE) to monitor and analyze hail events (see, for instance, Ceperuelo et al., 2006; López et al., 2008; López and Sánchez, 2009)

The SCIT algorithm, the second world-wide known centroid-type tracker, performs the volumetric (3D) cell identification in two stages. First, two-dimensional

(2D) thunderstorm structures are created using seven reflectivity thresholds, isolating the convective cells from surrounding areas of lower reflectivity, and obtaining their centroids. Second, 3D cells are obtained by associating 2D storm centroids in consecutive elevation scans and connecting them through distance constraints. In this latter step, possible multiple associations or non-associated cells are solved by considering the equivalent liquid water content estimated from the reflectivity, or by imposing larger research distances. In the tracking module, the SCIT algorithm makes a first guess of the cells' locations by computing the motion vector of the past scans, using a linear least-square fit. Finally, the current cells' locations are compared to the first guess, and the track is constructed by connecting the centroids, matching again a distance constraint. This algorithm was adapted to the entire Spanish region by the Service of Applied Techniques (*Servicio de Técnicas Aplicadas*, STAP, Martín et al., 2001, 2002; Martín et al., 2007), in the Spanish Meteorological Agency (*Agencia Española de METeorología*, AEMET), and to the Catalan area by the Meteorological Hazards Analysis Team (*Grup d'Anàlisi de situacions Meteorològiques Adverses*, GAMA) from the University of Barcelona (Rigo and Llasat, 2002, 2004; Rigo et al., 2010).

3.1.1 Nowcasting status at the Meteorological Service of Catalonia

Concerning the nowcasting techniques at the Meteorological Service of Catalonia (*Servei Meteorològic de Catalunya*, SMC) two processes are working together for the same purpose. The first one is based on mesoscale NWP models, in concrete on the Weather Research and Forecasting model (WRF, Skamarock et al., 2008). This runs at 3-km resolution, which is the finest operational resolution at the SMC. During this process, data from METeorological Aerodrome Reports (METARs, from airports), Automatic Weather Stations (AWS), and weather radar, are assimilated into the simulations, resulting in good forecast outputs for events related to meso-β systems or greater (>10 km in horizontal length scale, Markowski and Richardson, 2011; Fujita, 1981). However, Catalonia has a complex topography resulting, as stated previously, in a big handicap when trying to reproduce smaller convective scales.

The second procedure considers exclusively remote sensing data sources (lightning and weather radar) and is the operational procedure working nowadays. For this purpose, different tools/algorithms are working for the same objective: severe weather surveillance. On one hand, there is the Lightning Jump (LJ) algorithm

(Farnell et al., 2017), which computes, in real time, sudden increases of total lightning 1-min rates occurring within a thunderstorm. This tool runs each minute and considers exclusively lightning data, and once a LJ is triggered, an alert (e-mail) is sent to the forecasting team. Running in parallel to the previous one, but with a time resolution of 6 min (the time of generation of the radar volumes at the SMC), the radar-based centroid-type identification, characterization, and tracking of thunderstorms algorithm (the SCIT adaptation to the Catalan area) analyzes the volumetric data of the Catalan radar network (explained in Chapter 4).

The final product generated from combining the LJ and the radar-based tracker is obtained when the latter considers the thunderstorm associated with LJ and generates a cone of probabilities of occurrence of severe weather in the next 2 hours. This final product is planned to be completely operative in May 2020, which will be evaluated by a forecaster, the responsible person for creating the final warning map for the area and sending it to Civil Protection of Catalonia (the organism responsible for warning the population and managing the emergency systems in Catalonia).

3.2 Multiple-Doppler retrievals

Going a step further, another important technique for studying thunderstorms, which has also become a pursuit in several weather services worldwide, is the multiple-Doppler radar retrieval (obtaining 3D wind fields within a thunderstorm from radar observations). Getting to know the entire wind field within a storm allows an understanding of how it may interact not just with its environment but also with its internal evolution during its life cycle, and therefore, to improve the nowcasting. Furthermore, the derived fields may be used to feed high-resolution models which can allow us to forecast and understand complex cases in the future (Klemp and Wilhelmson, 1978; Rotunno and Ferretti, 2003). Retrieving the 3D wind field with multiple-Doppler techniques can be achieved using the radial observed velocity from two or more non-collinearly located Doppler radars (Figure 3.2).

Different techniques using Cylindrical and Cartesian coordinates systems are explained, for instance, in Armijo (1969), Ray and Wagner (1976) and Ray and Sangren (1983), which are the basis for more advanced techniques presented in the following paragraphs. The mean radial velocity from every single radar is related to the rectangular components of the mean velocity of the hydrometeors (u,v,w) through the azimuth, ϕ, and elevation, ϵ, angles. Therefore, it is possible to obtain

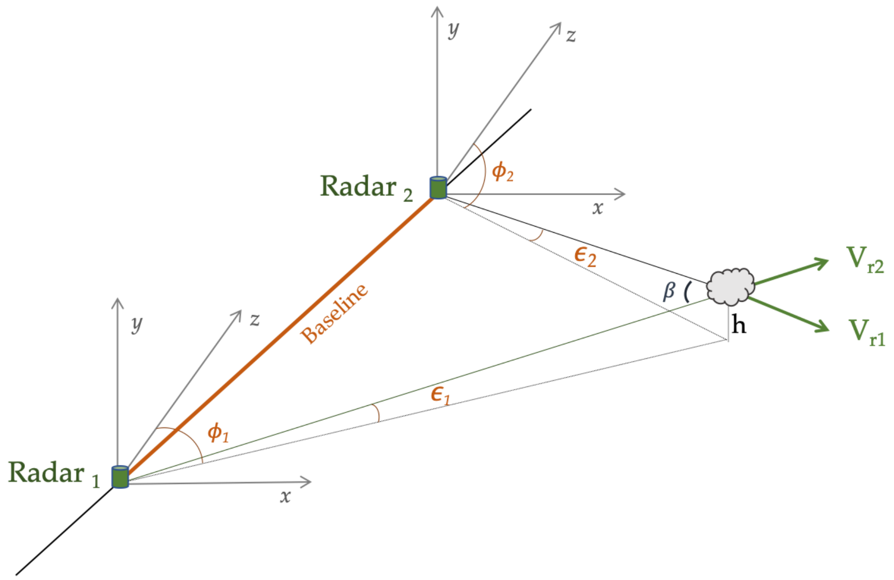

Figure 3.2: Dual-Doppler Cartesian geometry from two radars viewing the same point of a thunderstorm, from two different locations (the Cartesian wind components are Vr_1 and Vr_2). ϵ indicates the elevation angle, ϕ is the azimuth angle, h shows the height from the ground to the target, β is the beam-crossing angle, and the *baseline* indicates the distance from one radar to another. *Adapted from Rauber and Nesbitt (2018)*

a unique solution for the horizontal and vertical velocities at a point by combining the radial velocities in a closed equation system or, in the case of the dual-Doppler technique (with observations from only two Doppler radars), by applying boundary conditions on the vertical velocity and the terminal velocity of the particles, (Miller and Strauch, 1974), and by integrating the mass continuity equation.

It is well known that weather radar products may be affected by sampling errors, beam effects, beam blocking or changes in spatial resolution when interpolating the data, among other problems (Doviak et al., 1976; Miller and Kropfli, 1980; Carbone et al., 1985; Berenguer et al., 2006; Trapero et al., 2009). These effects may impact especially the retrieval of the vertical component of the velocity and the integrated divergence, where most of the assumptions and boundary conditions are applied. Multiple-Doppler radar techniques have been continuously developed and enhanced, facilitating the obtention of important results such as the dynamics of supercells, tornadoes or hurricanes (Marquis et al., 2008; Frame et al., 2009; Wurman et al., 2010; Potvin et al., 2012; Kosiba and Wurman, 2014), although those results have been mostly obtained during field campaigns using mobile research radars, and therefore not facing the added problems that may arise when using an operational radar network. For instance, dealing with the *Doppler Dilemma* (Doviak and Zrnic, 2014) in an operational arena, might force to scan in a longer unambiguous range for surveillance tasks, and thus have a shorter velocity range to avoid aliasing of radial velocities outside the Nyquist interval (Doviak and Zrnic, 2014; Altube et al., 2017). Also, radar baselines (separation between both radars) are usually around 100 km or more, which impacts the coverage area and the data resolution (Davies-Jones, 1979), and sometimes the system has to deal with complex topography, which may compromise the data collected due to blockage.

Despite all the problems of dealing with operational systems, there exist some recent studies on the implementation of this technique with operational data. For instance, Chong et al. (2000) proposed for the first time a near-real-time dual-Doppler analysis, implementing the technique in the Mesoscale Alpine Program (MAP) field campaign in 1999. This technique was based on a complex terrain adapted version (Chong and Cosma, 2000) of the Multiple-Doppler Synthesis and Continuity Adjustment Technique (MUSCAT, Bousquet and Chong, 1998), with a radar baseline of about 70 km and two C-band radars. (Bousquet et al., 2007, 2008a,b) demonstrated successfully how to implement the MUSCAT algorithm to the French operational radar network, which will serve to improve their nowcasting system in the future Bousquet and Tabary (2014). Dolan and Rutledge (2007) also proposed a near-real-time integrated display and analysis tool to help scientists in field projects, as well as to improve the nowcasting in warm-season convection This was done using dual-Doppler techniques with four radars from which two of them were operational. Friedrich and Hagen (2004) demonstrated the capability of retrieving multiple-Doppler winds by using the monostatic operational German Weather Service's (DWD) radar network and a bistatic radar network (Wurman et al., 1993; Wurman, 1994) as a possible operational surveillance tool around the Frankfurt/Main International Airport.

Part II

AREA OF STUDY AND DATA

4

Area of study and data

According to the current legal framework, there are two official agencies in charge of the meteorological forecast and research and to provide the information to the civil protection authorities in Catalonia; AEMET and the SMC. Since one of the supervisors belongs to the SMC, and due to the easy acces to the data, the current project has been exclusively based on the Catalan area and the SMC instrumentation and procedures. However, with the appropiate previous data treatment, most of the techniques developed in the present study can be applied to AEMET or other meteorological/research services data.

4.1 Area of study

As stated in Chapter 1, Catalonia is located in the northeastern corner of the Iberian Peninsula, covering an area of approximately 32,000 km^2. Although it is mostly known by being surrounded by the Mediterranean Sea to the east, and the Pyrenees to the north (reaching more than 3,000 m in altitude), the complex topography makes this region perfect for local and interesting meteorological phenomena. Some of the most important geographic features are the Central Depression to the west, the Littoral and Pre-Littoral ranges parallel to the coastline, and the different mountains forming the Pre-Pyrenees (Figure 4.1), which will appear in different sections of the present thesis.

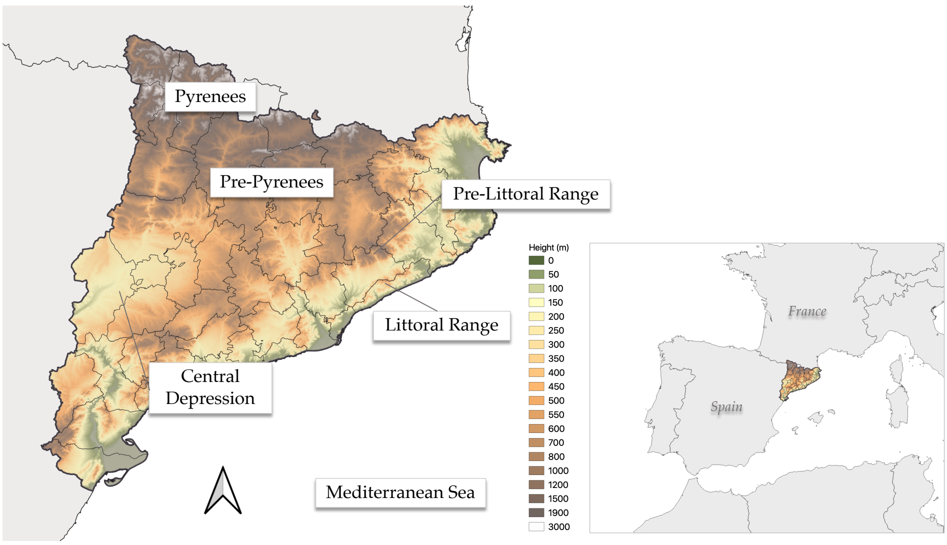

Figure 4.1: Area of study: Catalonia and its main topographic features.

4.2 Networks

The main data source used in this thesis has been from the SMC radar network, either purely weather radar, or in combination with other sources. It has been also utilized other sources or databases to validate and support the research conducted. This data is explained in Section 4.4.

4.2.1 XRAD

The radar network of the SMC, the XRAD *(Xarxa de RADars*, in Catalan) is composed of four C-band ($\lambda \approx 5.36$ cm) Doppler radar with single-polarization (see Altube et al., 2015, for more details). The network is configured with the main goal of providing the necessary information for surveillance tasks during adverse weather episodes and for hydro-meteorological purposes. Table 4.1 shows the main features of the XRAD, while Figure 4.2 presents the spatial distribution. Despite the complex topography of the territory (areas in dark grey in Figure 4.2) which still produces some partial or total blockage of the lower elevation beams for individual radars (Trapero et al., 2009), the network is configured to provide a good reflectivity composite with almost no blockage under 3,000 m height (approximately the top of the Pyrenees). Although the PBE radar was first installed in 1996 (see Table 4.1 for radar name), it was not until 2002 that it became officially an SMC facility (previously managed by the University of Barcelona for research purposes). The entire network was set to operational between 2002 and 2008, and therefore most of the studies here presented have been done using data from 2008 to today's date. It is worth to mention, though, that from 2013 to 2015, the composite data used is the result of only three radars (CDV, LMI, PDA) since PBE was being updated.

Table 4.1: Radar site name, abbreviation, installation year, altitude Above Sea Level (ASL), location (latitude and longitude), ranges, operational elevation angles, and total number of elevations of the XRAD.

Name	**Abbrev.**	**Year**	**Altitude [m ASL]**	**Lat, Lon [°]**	**Ranges [km]**	**Elev. [°] /num.**
Puig Bernat	PBE	1996	610	41.37, 1.39	130-240	0.6-27 / 16
Puig d'Arques	PDA	2002	542	41.89, 2.99	130-240	0.6-27 / 16
Creu del Vent	CDV	2003	825	41.96, 1.40	150-250	0.6-27 / 16
La Miranda	LMI	2008	910	41.09, 0.86	130-240	0.6-27 / 16

Scanning strategy

The XRAD operational chain is managed using Sigmet-Vaïsala IRIS© software (Vaisala, 2014a), and retrieves each single radar volume, PPIVOL, in a 6-minute cycle, which is composed of three different sub-tasks; VOL_A, VOL_B, and VOL_C. Each sub-task contains 16 different Plan Position Indicator (PPI) for each radar

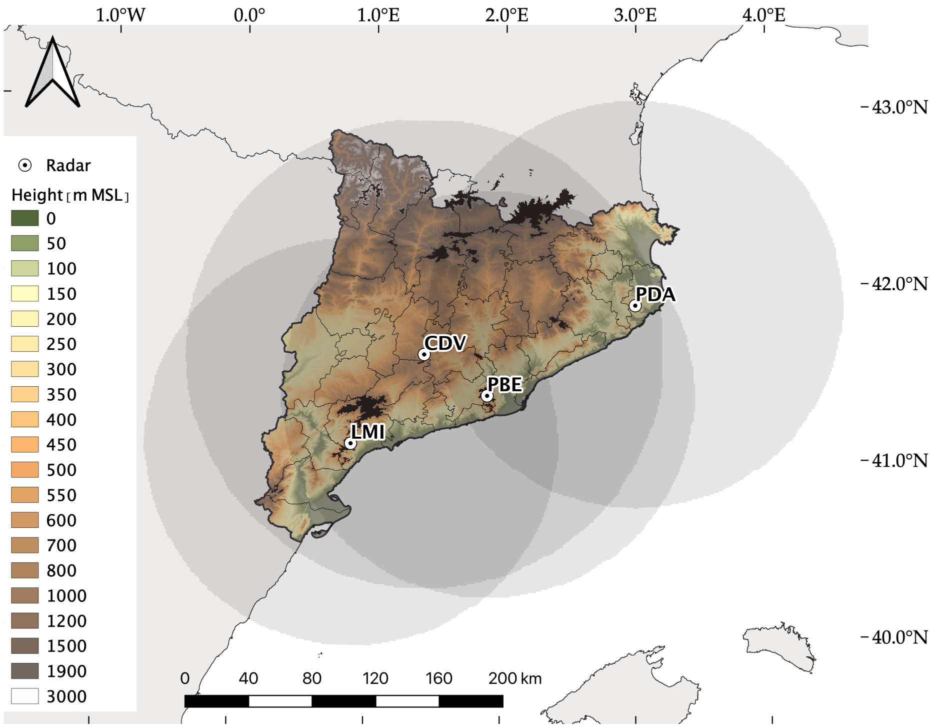

Figure 4.2: The Meteorological Service of Catalonia radar network, XRAD. Spatial coverage (shaded in grey) and topography blockage (areas in black) for a 0.6° elevation angle. All radars have a maximum range of 130 km, except for CDV (central one) which is 150 km.

(fixed elevation, ϵ, and varying azimuth, ϕ). The VOL_A is a long-range surveillance sub-task that stores only two radar moments: uncorrected reflectivity, T (noise corrected but not Doppler clutter filtered, Altube, 2016), and reflectivity, Z. VOL_B and VOL_C volumes are formed by short-range sub-tasks that include also the radial velocity, V. Table 4.2 shows the ranges, the Pulse Repetition Frequency (PRF, number of pulses of the repeted signal per second), the elevation angles, and the radar moments stored for the three sub-tasks. The reflectivity and radial wind fields are automatically filtered in the processor during a quality control procedure. This allows us to obtain the best and fastest field possible to combine and to develop the surveillance composite, removing the main topographic non-meteorological targets. The processor applies a Signal to Noise Ratio (SNR), a Clutter-to-Signal Ratio (CSR) and a Signal Quality Index (SQI) (Vaisala, 2014b) thresholds to the radar data. However, these filter values (see Altube, 2016; Altube et al., 2017, for more detail) sometimes are very aggressive, especially for the radial velocity, which then translates to missing bins in the radar image. Each of the sub-tasks is stored as raw base data (RAW volume data in polar coordinates). These volumes are compressed in 1-byte IRIS format containing the moments mentioned in Table 4.2. Althought the spectral width (distribution of velocities in a radar pixel, W) is used to correct the original data, this moment, neither the unprocessed nor the unfiltered original data, are saved in the RAW product.

Table 4.2: Sub-task name, type, ranges depending on radar (see Table 4.1), elevation angles, PRF and stored moments for the scanning strategy definded for the XRAD.

Task	Type	Ranges [km]	Elev. [°]	PRF	Moments
VOL_A	Long Range (Surveillance)	250/240	0.6	Single	T, Z
VOL_B	Short Range	150/130	0.6, 0.8, 1.0, 1.3 1.7, 2.0, 3.0	Dual	T, Z, V
VOL_C	Short Range	150/130	4.0, 5.0, 6.0, 8.0, 10.0 13.0, 16.0, 21.0, 27.0	Dual	T, Z, V

4.2.2 XEMA

The AWS network of the SMC, the XEMA (*Xarxa d'Estacions Meteorològiques Automàtiques*, in Catalan), is formed by 188 AWS (as of January 2019, `www.meteo.cat`) distributed across the entire region of Catalonia. Most of the stations have different sensors to measure the temperature and relative humidity of the air, the atmospheric pressure, the direction and velocity of the wind, the solar global irradiance and the precipitation (Llabrés-Brustenga et al., 2019). The latter is the one most used in the present work, and it is measured using rain gauges with a minimum detection threshold of 0.1 mm. For most of the stations, data collected is recorded and sent to the SMC every half an hour via GPRS (General Packet Radio Service) communications, although there still remain some stations that send the information every hour.

4.2.3 XDDE

The lightning detector network of the SMC, the XDDE (*Xarxa de Detecció de Descàrregues Elèctriques*, in Catalan) is formed by four remote VAISALA LS8000 detection stations, operative from 2004 (Pineda et al., 2011; Pineda and Rigo, 2017). The XDDE detectors include very-high and low-frequency detectors, which allow detecting Intra-Cloud (IC) and Cloud-to-Ground (CG) lightning, respectively. The sensors can detect up to 100 strikes per second which are grouped into IC or CG lightning. The geographical location is made utilizing Magnetic Direction Finding (MDF), Time of Arrival (TOA) and an interferometry technique (retrieving the difference of the wave phase measured at the same time by all the antennas located in a radial position, Cummins and Murphy, 2009). This allows the location of the emitting source (flash). The XDDE provides the time (in Universal Time Coordinated, UTC), the location (in latitude and longitude coordinates and estimated error) of isolated IC strikes and IC trajectories (starting, middle and ending nodes). It also provides the number of strikes for each CG lightning (initial and successive ones), as well as the time (UTC) the location (in latitude and longitude coordinates and estimated error) and the electrical characteristics of each strike: polarity (negative/positive), amplitude and peak current (kA). All that information is recorded every milisecond (10^{-3}s^{-1}) and feeds the operational LJ algorithm explained below.

4.3 Products

4.3.1 CAPPI

One of the products from the XRAD used in the present thesis is a volumetric composite product of 10 CAPPIs (Constant Altitude Plan Position Indicator) going from 1 to 10 km, in 1 km increments. These are horizontal cuts of interpolated data at a fixed altitude, obtained from a corrected PPI set for each radar. The product, called CAPPI_150x10, is a composite generated by combining the short-range CAPPI reflectivity volumes obtained from each one of the four radars of the XRAD, with a spatial and temporal resolution of 2x2 km^2 and 6 min, respectively.

4.3.2 QPE

Another product used has been the Hydrometeorological Integrated Forecasted Tool (EHIMI, Sánchez-Diezma et al., 2002) Quantitative Precipitation Estimates (QPE) fields. These fields are obtained by integrating corrected radar data from the EHIMI tool with XEMA rainfall observations in hourly and daily time resolution. First, radar reflectivity data is combined into CAPPI products (CAPPI_EHIMI) going through the following corrections: speckle filtering, removing echoes from anomalous propagation, monitoring signal stability, correcting the total volume available, correcting pointing errors, removing orographic echoes and reconstructing the field to compensate for orographic influence (Corral et al., 2009). Then, the reflectivity fields are converted into precipitation intensity and accumulated precipitation, including the movement of the precipitation systems, and ensuring that the rainfall field data is more continuous. Finally, QPE fields are retrieved by combining the accumulated EHIMI rainfall field with the XEMA data, utilizing a Kriging with External Drift (KED) interpolation (Trapero et al., 2009; Velasco-Forero et al., 2009). In the present thesis it has been used the 24h QPE fields, which are georeferenced raster maps (pixel or bits mesh) and a spatial resolution of 1 km^2.

4.4 Validation data

The data described below has been used especially in the last section of the thesis, the dual-Doppler study (Chapter 9).

4.4.1 Lightning Jump database

The LJ algorithm is, as stated before in Chapter 1, one of the current operational tools used in the nowcasting system at the SMC. This algorithm (see Farnell et al., 2017, for complete details) gives an alert every time that a LJ is triggered, when a sudden increase of total lightning 1-minute-rate occurs within a thunderstorm. The database contains all the LJ triggered from the period from 2006 to date (more reliable from 2008), and gives the date and time of occurrence (in UTC), the location (in latitude and longitude), and the level of the LJ (N1 if it exists multiplicity and N2 if not, the latter indicating more severity since the algorithm is more restrictive in the identification features). In the present study, it only has been used the location and time, as a proxy of severity information for the events.

4.4.2 Severe weather database

The severe weather database of the SMC is an internal information that has been under construction for the last years (Rigo et al., 2015). This database includes a total of 275 events that have been registered within the period 2001- 2019, including hail and strong wind-related events following the definition from (Farnell et al., 2017) and stated in Chapter 1. More in concrete, in this database, 67 % of the cases are hailstorms and the remaining 33 % are wind-related phenomena (14 % downburst and wind gusts and 19 % tornadoes). As it occurs with other severe weather climatology based mainly on spotters' observations, there are some factors to consider while reading the availability of records in this database (Doswell III et al., 1996; Schuster et al., 2005; Tuovinen et al., 2009), such as the dependency on the population density or the improvement on technologies, among others. In particular, the latter has favored the increase of the number of records during the last years; the increase of social media platforms and the ease to share live videos and pictures has resulted in 50 % of the total events being recorded within the last 6 years. The information recorded in the database is the date and time (in UTC) of occurrence of the severe weather phenomena, the location (latitude and longitude) and the magnitude. The latter is referred to the size (in cm) for hail records, and velocity (in $\mathrm{m\,s^{-1}}$) for wind-related records. This information is obtained with the official weather station network (XEMA, explained above), and the collaboration of spotters and the recent citizen-science project "*Plega la Pedra*" (Farnell, 2018, Pick up the hail, in Catalan), implemented to obtain information of hail reports in areas with sparse meteorological stations.

Part III

RESULTS

5

Identification of anomalous propagation with accumulated rainfall fields

* The present chapter has been adapted from: del Moral, A., M.C. Llasat and T. Rigo, 2017: Identification of anomalous motion of thunderstorms using daily rainfall fields. *Atmos. Res.*, 185, 92-100, doi: https://doi.org/10.1016/j.atmosres.2016.11.001, ©Elsevier. Used with permision.

As explained in Chapter 1, severe weather phenomena are the print on the ground of some thunderstorms during their mature stage, when they are fully formed and may present anomalous propagation (e.g. stationarity, splitting or merging and sudden changes of direction). In this sense, the identification of these unexpected propagation patterns may be a useful tool for the prediction of this type of event.

For instance, the stationarity of Heavy Precipitation (HP) thunderstorms may result in flash floods. In this regard, the present chapter suggests a first approach to detect this type of propagation from the footprint of thunderstorms on the surface: the accumulated precipitation field (24h QPE fields explained in Chapter 4). The main goal is to develop a technique that can quickly and easily identify convective structures and the aforementioned anomalous movements. To that end, it is proposed the identification from the geometry of the rainfall print on the ground. This allows for the study of thunderstorm paths without requiring specific radar-based algorithms, which are not always available. A second objective is the implementation of the proposed methodology to obtain a climatic analysis of the precipitation days in Catalonia for the period 2008-2015, to have a broad view of the convection activity and the possible anomalous movements in the area. This latter objective strengthens the first goal since, for such a period of time, implies to analyze over 700,000 volumetric radar images, which would require long calculation times when applying the usual procedures.

5.1 Methodoloy

The daily rainfall fields lose some validity in the domain boundaries due to the distance to the radars, and a lack of observational data on the ground (Doviak and Zrnic, 2014). Therefore, before starting the preliminary classification, a mask covering only the area of Catalonia was applied to all the rainfall fields (raster maps). All the procedures of this chapter were developed using the programming environment for data and image processing R-Cran (R Core Team, 2019).

5.1.1 Selecting potentially convective days from daily precipitation fields

Once the mask was applied, a preliminary classification of each daily precipitation map was made following the criteria showed in Table 5.1. Taking into account that every daily rainfall field contains the total accumulated precipitation for Catalonia, a Daily Precipitation Structure (hereinafter, DPS) was defined as every set of at least 6 grouped pixels (area of $6\,\mathrm{km}^2$) within the daily precipitation field.

First, the days that did not show any DPS or with one or more structures not exceeding $1\,\mathrm{mm}$ and a continuous extension of $20\,\mathrm{km}^2$ (20 pixels) or more, were classified as No Rain (NR) days. This restriction was put in place in order to distinguish between the days with precipitation caused by fog or dew, or very small

Table 5.1: Precipitation (P) and extension (A) thresholds imposed to daily rainfall field maps. Days are classified into "No Rain" days (NR), "Non-Potentially Convective" days (NPC) and "Potentially Convective" days (PC).

	$0 = P$ [mm]	$0 \leq P < 1$ [mm]	$1 \leq P < 15$ [mm]	$P \geq 15$ [mm]
$A < 20\,\mathrm{km}^2$	NR	NR	NPC	PC
$A \geq 20\,\mathrm{km}^2$	NR	NPC	NPC	PC

precipitation structures. Second, days showing DPS with accumulated precipitation between 1 mm and 15 mm, were catalogued as Non-Potentially Convective (NPC) days. Finally, days that showed at least one DPS with maximum accumulated precipitation of over 15 mm were classified as Potentially Convective (PC) days.

In order to validate the previous classification, the results were compared with the convective cells maps from the SMC (Figure 5.1). These maps contain 2D or 3D cells identified by the radar-based nowcasting algorithm from the SMC (Rigo and Llasat, 2004), running over the XRAD CAPPI products (Chapter 4). In this sense, NPC days should have only 2D cells, PC days should present 2D and 3D cells, and finally, NR days should not have any cell.

5.1.2 Normal/anomalous movements in precipitation structures

After the initial classification was made for the entire period, the study centered on days classified as PC, because they are more prone to produce severe weather. In this sense, once selected the PC day, only those DPS really convective were selected for the study. Those DPS presenting an area over $6\,\mathrm{km}^2$ (6 contiguous pixels) and accumulated precipitation higher than 15 mm, were defined as Potentially Convective Structures (PCS), and were selected to extract the real convective area of the DPS. The rainfall threshold of 15 mm was chosen on the basis of different studies on convective precipitation, heavy rainfall and flash floods in the Mediterranean region (Llasat, 2001; Barnolas et al., 2010; Papagiannaki et al., 2015). The PCS structures were then characterized in shape as ellipses, in order to detect any possible anomalous movements based on the footprint. This was achieved by means of computing the 2D spanning ellipsoid (ellipsoid hull) of every set of points that define each PCS; this is the smallest area with, at least, the 90 % of the given points

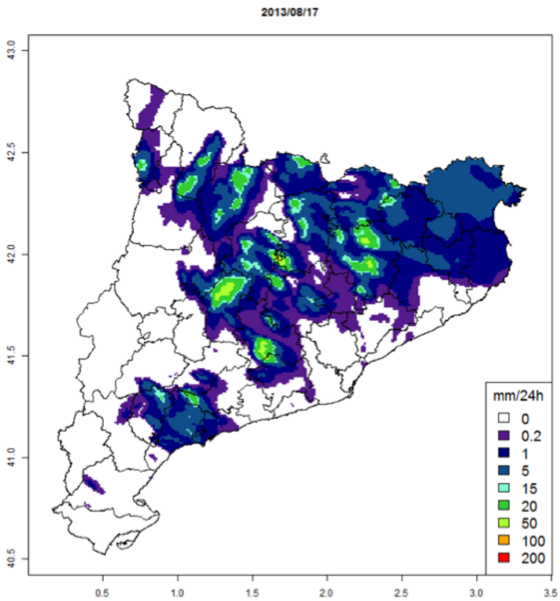

(a)

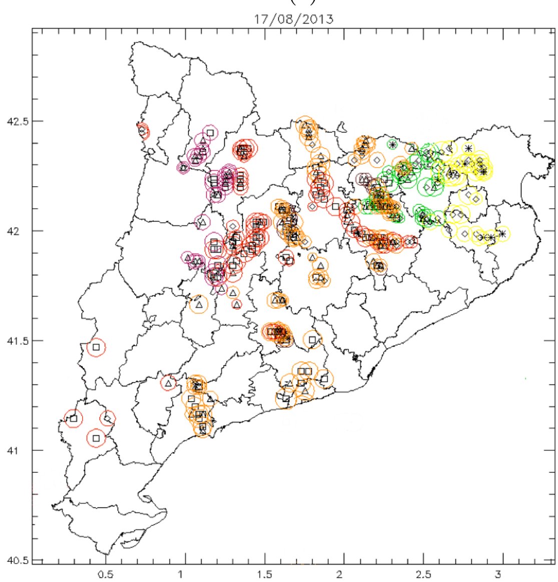

(b)

Figure 5.1: 17 August 2013. (a) 24 h accumulated rainfall field for the Catalan area (after the preliminary mask is applied); (b) Map of 3D cells detected via the radar-based nowcasting algorihtm at the SMC, for the same area.

lying inside the ellipsoid or on the boundary (Figure 5.2).

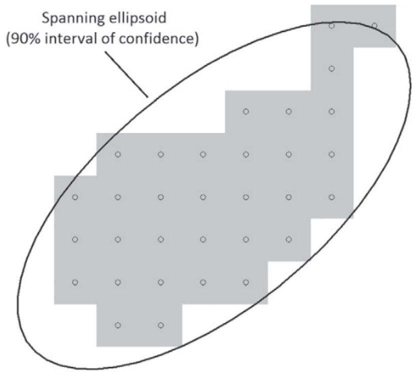

Figure 5.2: Example of the spanning ellipsoid of the points within the 90 % interval of confidence. Points are the centroid of the pixels that define the PCS.

Depending on the ellipsoid hull obtained, each structure was then cataloged as Elliptical (E) or Non-Elliptical (NE), considering radius criteria and shape similarity index based on the *Jaccard similarity coefficient*. The Jaccard similarity coefficient is measured as the result of dividing the intersection and the union of sample sets A and B, and it represents an index to compare similarity, dissimilarity, and distance of a data set of data (see, for instance, Seifoddini and Djassemi, 1991):

$$J(A, B) = \frac{A \cap B}{A \cup B}, \tag{5.1}$$

In our case, we considered the pixels that define the ellipsoid hull as sample A, and the pixels that define the actual structure as sample B. Finally, after a sensitivity test analyzing a large dataset of PCS and ellipsoid shapes, the following radius and Jaccard coefficient were defined to discern between E and NE structures. In the following criteria R_l and R_g are the semi-minor and semi-major axis of the ellipsoid hull, respectively:

$$\begin{cases} \text{if } R_l < \frac{3}{5}R_g \;\; and \;\; J \geq 0.65 \Rightarrow E \\ \text{if } R_l \geq \frac{3}{5}R_g \;\; and \;\; J < 0.65 \Rightarrow NE \end{cases} \tag{5.2}$$

The characterization of each PCS ellipsoid was maed following the features in Table 5.2; identifier number, number of pixels (area of the structure), position of the center of mass (in Universal Transverse Mercator, UTM, coordinates), R_g and R_l longitude, orientation of the ellipse (θ, in degrees) and final ellipse classification (E or NE). The orientation is defined as the angle between the x-axis and the major axis, R_g, of the ellipse, ranging from 0° to 180°, and increasing in a counter-clockwise direction (starting from the horizontal plane to the right). This shape-based classification allowed us to quickly see the propagation footprint on the ground, and therefore the thunderstorm behavior. A PCS cataloged as E can be identified as coming from thunderstorms that have probably had a regular path, guided by the mean wind. A thunderstorm with cumulus, mature and dissipating stages well defined (for instance, without interactions with neighbour cells), will present a growing and decaying rainfall footpring on the ground (ellipse well defined, see The COMET Program, https://www.meted.ucar.edu/, for more details). On the other hand, a PCS cataloged as NE can be identified as a structure with potentially anomalous movement. Within the NE category, structures with a

Table 5.2: An example of classification for structures identified on 17 August 2013. Semi-major axis, R_g and semi-minor axis, R_l, are shown in metres, the centre of mass (X_x, Y_c) is given in UTM coordinates, and the orientation (θ) is shown in degrees. Finally, the status indicates if the structure is elliptical (E) or non-elliptical (NE).

ID	**N pixels**	X_c [UTM]	Y_c [UTM]	θ [°]	R_l [m]	R_g [m]	**Status**
1	35	350038.98	4703284.14	41.29	2911.46	5557.01	NE
2	29	315060.79	4701133.91	94.69	3239.45	3678.31	NE
3	37	403361.92	4701120.46	154.15	3199.33	5360.08	E
4	137	369552.5	4689266.07	74.08	4989.08	14529.11	NE
5	77	340536.82	4689390.96	45.34	3748.14	8137.17	E

circular shape indicate that the thunderstorm remained stationary at the time, and structures in a V-shape indicate that the structure is associated with a convective system that presents merging or splitting cells. Finally, structures with rectangular shape indicate that the thunderstorm probably maintained its intensity throughout its path, self-maintained by specific factors (orography, other cells, etc.). Figure 5.3 shows an example of daily map with PCS indetified in orange, where E PCS are outlined with a thick line.

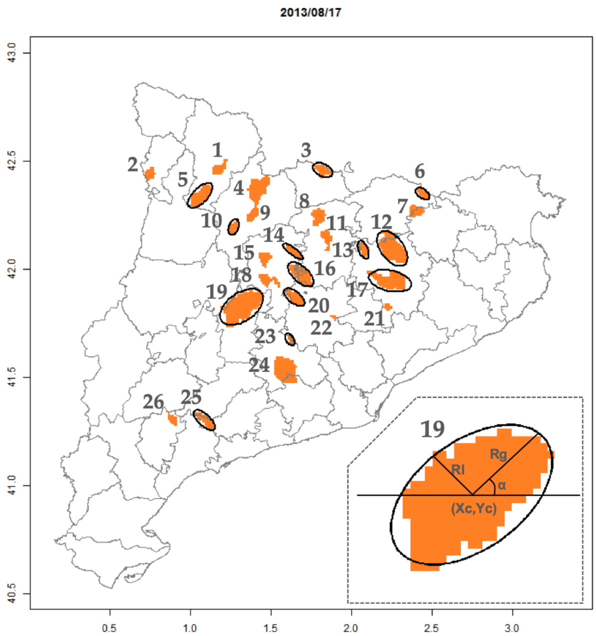

Figure 5.3: Convective structures detected on 17 August 2013 and a close-up of an elliptical PCS and its parameters.

5.2 Results

5.2.1 Classification of daily rainfall fields: validation

As stated in Section 5.1, the validation of the previous classification of the daily fields into No Rain (NR), Non-Potentially Convective (NPC), and Potentially Convective (PC) was based on a dichotomous characterization. These were compared to the 2D and 3D radar-based cells from the SMC. In this sense, s Success Ratio (SR) of 0.71 was obtained, indicating that for 71 % of the forecasted PC days, convection actually occurred. It was also shown a Probability of Detection (POD) of 0.61, indicating that almost 3/4 of the PC days observed were predicted correctly (these were real convective days). The results are promising, especially given that 2D and 3D maps, from a radar-based algorithm, were considered as observed events in the dichotomous validation. These maps are created using data from four SMC radars which, in some cases, it may be incorrect or missing due to operational issues. Moreover, sometimes false echoes appear on radar images due to anomalous echo propagation and orographic enhancement (Panziera and Germann, 2010;

Doviak and Zrnic, 2014). These may result in detecting false thunderstorms cores, and therefore false 2D or 3D cells. Finally, we should bear in mind that some thunderstorms (especially small and isolated cells) are sometimes not efficient enough to produce significant precipitation accumulation and are not detected within the daily rainfall field.

5.2.2 Precipitation patterns

Once the classification was done, the convective precipitation in Catalonia was analyzed on a monthly and seasonal scale, depending on the mean typology of the DPS (Figure 5.4). After that, for those Potentially Convective (PC) days, an analysis of the Potentially Convective Structures (PCS) and their morphology (Elliptical, E, and Non Elliptical, NE) was also analyzed in a monthly and seasonal scale (Figure 5.5). The results of the precipitation's typology (based on Daily Precipitation Structures, PCS) are consistent with other studies in the same area. As it was found for Barcelona for a longer period by Llasat (2001), and for the Internal Basins of Catalonia for a 10-year period by (Llasat et al., 2007; Barnolas et al., 2010), convective days (PC) are predominant during summer (Figure 5.4b). However, while these authors obtained autumn as the second convective season, results here point to spring as the second one. This difference could be due to the inclusion of the western and mountainous region of Catalonia in the present study, which usually triggers Convective Initiation (CI) in spring. A second reason could be related to the fact that the contribution of convective precipitation by day is major in autumn than in spring. For days considered as PC, between 50 % (summer) and 59 % (winter) of the cases showed a NE morphology (Figure 5.5b). It is observed that when a day has a high number of DPS or the rainfall field covers a broad area of the map, the accumulated precipitation threshold applied is low and more than one DSP can be considered as being part of the same structure, increasing the number of NE structures. On the other hand, the high number of NE structures found within a season is due to that all the elongated and circular shapes have been considered as structures with anomalous propagation. A deeper analysis has demonstrated that within the NE structures are included cases don't necessarily present anomalous propagation, usually because these are cell clusters.

Moreover, it is important to note that there are three months in late summer and autumn that, on average, have a noticeable amount of NE structures: August, September, and November (Figure 5.5a). This is a factor to bear in mind since, knowing which months have more NE structures along with the areas more affected,

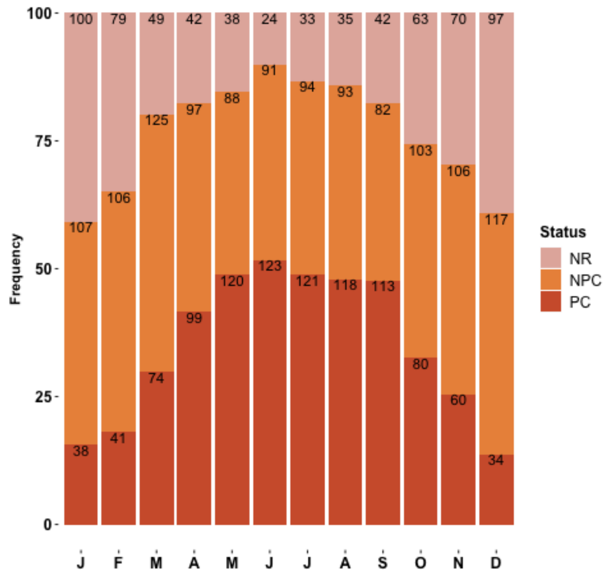

(a)

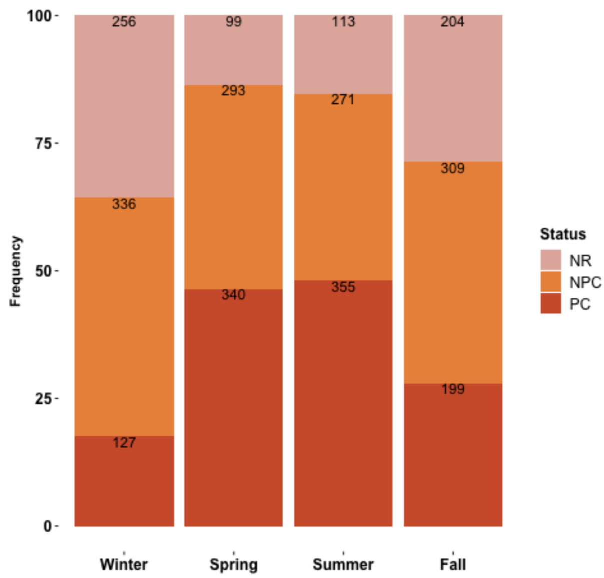

(b)

Figure 5.4: Classification of the typology for daily precipitation (2008 − 2015): absolute (y−axis) and relative frequency (inside bars); (a) by month; (b) by season.

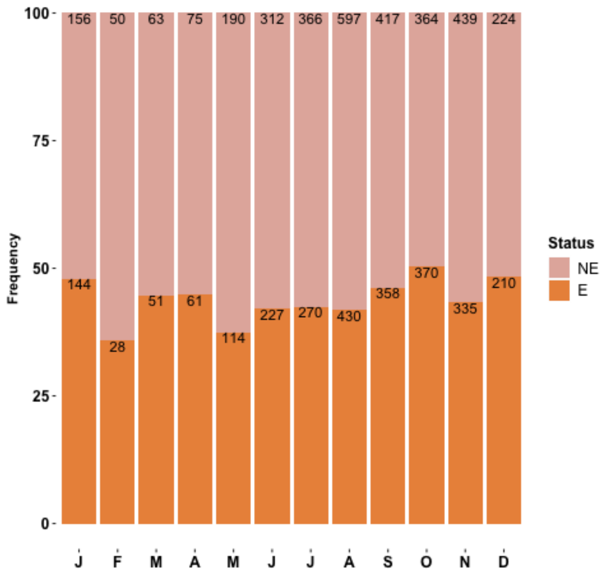

(a)

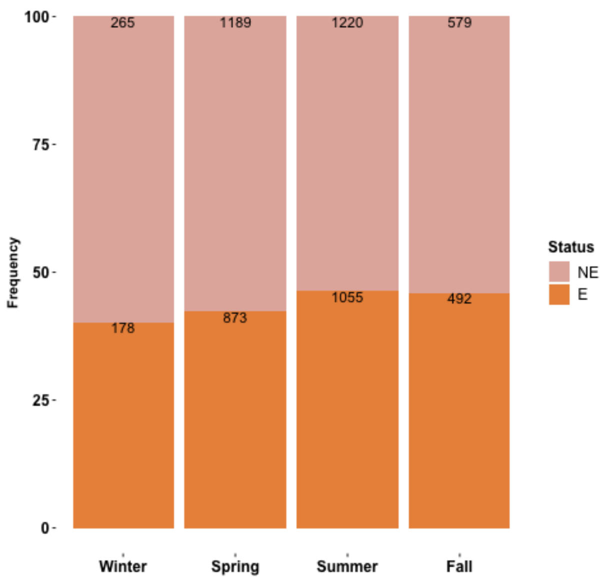

(b)

Figure 5.5: Classification of the shape of the convective structures $(2008 - 2015)$: absolute $(y-$axis) and relative frequency (inside bars); (a) by month; (b) by season.

can help to limit the severe weather studies in time and space, and also improve the surveillance purposes. As it has been previously commented, PCS structures are quite usual during spring (for instance, he hail campaign runs from May to September in the western plains), although the most convective period is between summer and early autumn (usually because of bigger systems with the easterly maritime flow). Furthermore, during the winter season, more E than NE structures are expected, due to the typology of the precipitation during this season, which is mainly stratiform. Despite this, the results show that the number of NE structures is comparable to the spring and autumn seasons. This is mainly because structures with an elongated shape are considered as NE, although these could be considered as structures with normal movements (despite not being an elliptical shape).

The spatial distribution of PCS is shown in Figure 5.6. It is demonstrated that most of the PCS structures are located in the northern region of Catalonia, over mainly mountainous areas. This was found by analyzing all the PCS for the entire period (2008-2015) aggregated in $5\,\mathrm{km}^2$ areas (raster maps), obtaining the density for the entire Catalonia region. This shows that around 120 PCS structures are located in the eastern Pre-Pyrenees, which coincides with the maximum spatial distribution of lightning activity, as shown by Pineda et al. (2011), who defined the region as an area of convergence. This also coincides with the area with maximum accumulated daily precipitation in Llasat et al. (2007). This may be associated with the triggering effect linked to the orography and proximity to the sea.

The visual analysis of a set of PCS shows that some shape patterns within the NE category are repeated many times, and that can be related to the different behaviors of a thunderstorm's life cycle, following Doswell III et al. (1996). Figure 5.7 shows the different types of mentioned shapes. For instance, V-shape structures may be associated with splitting and/or with a sudden change of directions. Some merging processes would be also described by this type of shape if the resulting cell stays stationary, or goes again through the same path as one of the previous cells. However, a variant of a V-shape structure appears if the resulting cell follows a perpendicular direction from the point where the merging process has occurred. This structure then results in a Y-shape. Circular structures may be thunderstorms that stay in the same place for an extended period, usually for more than half an hour. They can also be associated with geographical areas where thunderstorms tend to start or pass by more than once in the same day, such as convergence zones or ridges. Depending on the size of the structure found, they could be considered as individual cells or clusters. Elongated-shape structures may be associated with long-lasting thunderstorms that live for more than one hour. Finally, on the other

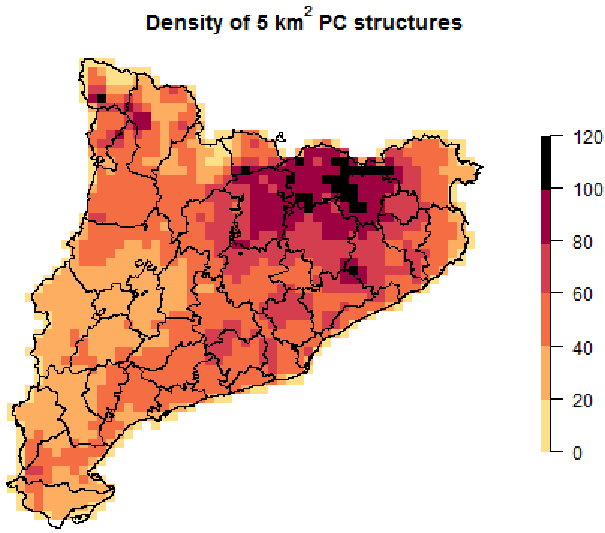

Figure 5.6: PC structures (PCS) at a density of 5 km^2 for the Catalonia region (2008-2015).

hand, cells considered as E structures are mainly single-cell or pulse thunderstorms, and therefore have a normal path. These types of thunderstorms have a typical life cycle and their radar signature at the surface is defined as an ellipsoid (wider at the center) caused by the higher precipitation intensity, as explained previously.

5.3 Conclusions

The study presented in this chapter shows a methodological approach to identify convective precipitation structures with anomalous movement from daily rainfall maps, and the possible anomalous pattern, from the geometric shape of the structures. This methodology has been divided into two phases: the first allows convective structures to be classified and identified only using the information provided by daily rainfall fields. Potentially Convective Structures (PCS) are defined by imposing, at least, an accumulated precipitation of 15 mm in 24 h and an area of 6 km^2 (6 pixels). This means that handling volumetric radar data is not required, and it becomes a useful tool to study behavioral trends for convection in a daily temporal scale. Applying this methodology to the 2008-2015 period in Catalonia, it shows that convective activity is mainly found between May and September, and convec-

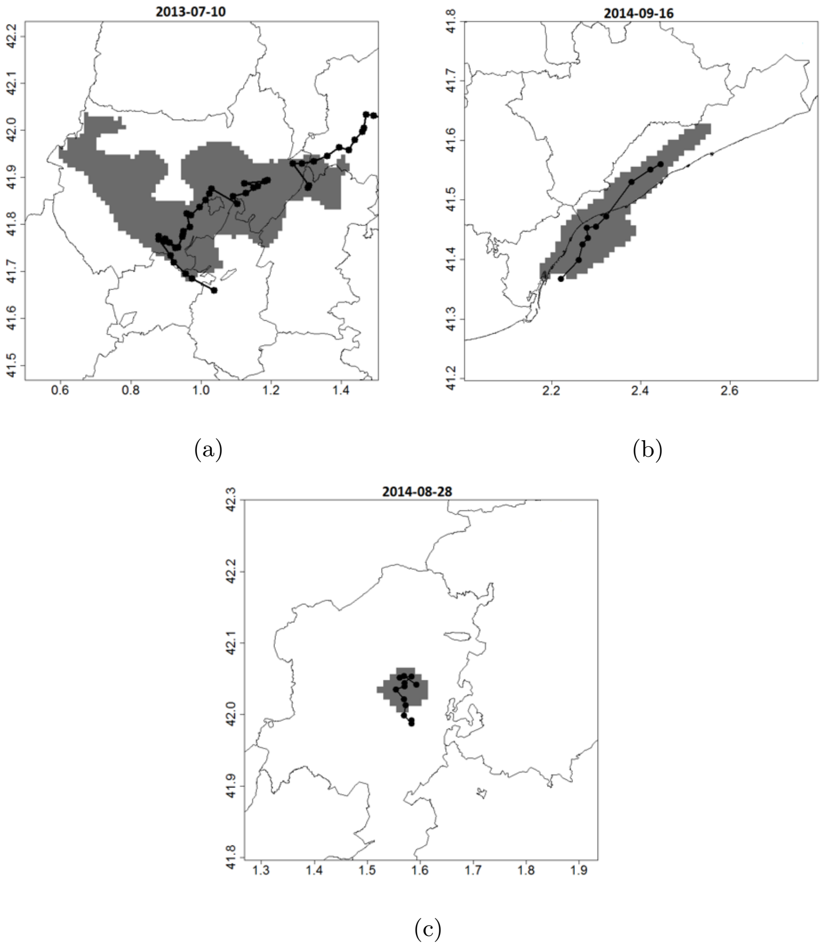

Figure 5.7: Examples of NE structures and their respective cell tracking; (a) V-shape; (b) elongated; (c) quasi-circular.

tive structures (PCS) are mainly located near mountainous areas, especially in the eastern Pre-Pyrenees. This is mostly due to the coupling of a wet advection from the Mediterranean Sea and orographic lifting processes.

The second phase of the methodology also involves identifying if the PCS structures are elliptical (E) or non-elliptical (NE), meaning that these present possible anomalous propagations. This has allowed identifying the seasons and areas of Catalonia that are more affected by structures with and without potentially anomalous movement, Non-Elliptical (NE) and Elliptical (E), respectively. Narrowing the dataset and visually analyzing the NE structures, the most repeated patterns suggest a shape classification into V-shape, circular, and elongated. As the number of Potentially Convective (PC) days increases, the amount of anomalous structures increases as well, especially in the summer, where the three types of structures that suggest an anomalous movement path are found. After analyzing different known cases with radar animations or imagery similar to that shown in Figure 5.7 we found that, on some occasions, not all NE structures were produced by real anomalous thunderstorm propagation, and some were the result of the sum of the path of different cells. For instance, in most of the cases, the circular shape was produced by a single convective stationary cell (which would be an anomalous movement), but sometimes the circular pattern was produced by a cluster of cells, or different individual cells affecting the same area. In order to better distinguish which NE structures were produced by single cells having anomalous movement or not, a gradient-based variable threshold for every single structure was tried (following the idea of Biggerstaff and Listemaa, 2000), taking into account the number of pixels and the maximum accumulated precipitation. Unfortunately, the results did not help to improve the methodology proposed, and after trying different thresholds, better results were found with the 15 mm proposed threshold. Usually, at the moment of a storm split, merge, or a change of direction, severe weather phenomena such as wind or hail are present. For this reason, the trace of precipitation at the surface doesn't present the highest values and, in some cases, shows a diffuse path. Because of this, the change of the precipitation threshold to higher values makes to lose very valuable information about the behavior of the thunderstorm, associated with the anomaly in the rainfall field. In fact, this anomaly is the main point of interest in the methodology.

To delve into the knowledge of this type of thunderstorm, it is necessary to apply other types of data sources and analysis to specific study cases, matching with the different types of PCS shapes that have been found. After getting the first picture of the most common anomalous propagation pattern that we can find in our area, we propose to go deeper in the analysis and to use volumetric radar data (better spatial and temporal resolution). This will allow us to better know some of the factors involved in the anomalous movement process in detail.

6

A radar-based centroid tracking algorithm for severe weather surveillance

* The present chapter has been adapted from: del Moral, A., T. Rigo and M.C. Llasat 2018: A radar-based centroid tracking algorithm for severe weather surveillance: identifying split/merge processes in convective systems *Atmos. Res.*, 213, 110-120, doi: https://doi.org/10.1016/j.atmosres.2018.05.030 ©Elsevier. Used with permission.

The identification and tracking algorithms presented in Chapter 3 can separate clusters of cells by applying different thresholds of reflectivity, although some of them don't have any special procedure to reproduce the real paths of the cells involved in a possible anomalous movement process, especially in multicell systems. Furthermore, in days with high convective activity, there is a lack of continuity in the cells' characteristics. Cells' shape and intensity may vary sharply and continuously, hindering the short-term forecasting. This is a big setback, especially when it comes to nowcast cells that may show anomalous movements during their life cycles, such as splitting into two different cells, or a merging process. This issue became more visible following the study of thunderstorms associated with severe weather presented in Chapter 5 and in del Moral et al. (2017). After analyzing a large dataset of 24-h precipitation patterns (referred to as PCS structures), the study concluded that an in-depth study is required for significant severe weather processes that have shown clear anomalous movements.

To overcome these challenges, the present study proposes a new methodology based on the radar-based SMC algorithm, focussing on the identification and tracking modules. In this sense, the main goal is to minimize the loss of continuity of the cells during their life cycle in days with high convective activity and to identify anomalous processes. With this purpose, the main differences between the proposed algorithm and those explained in Chapter 1 are two; first, when redefining the total area of the cell in each level within the volume, especially in those cells embedded in multicell thunderstorms, allowing to obtain a more realistic life cycle of the thunderstorms, and to get the most important features with greater continuity. Second, the use of the information from all levels of the thunderstorm, including the highest ones into the identification module, allowing to indicate if a splitting or merging process will occur.

6.1 Methodology

The new algorithm takes into consideration the previous SCIT and SMC methodologies (see Chapter 3). It proposes a new operational methodology to identify 3D structures, with the capacity to foresee if an anomalous movement will take place (before the tracking module), and to correctly reproduce the path of the thunderstorms involved in the phenomena. The data used has been the 10-level CAPPI products explained in Chapter 4 (spatial and temporal resolution of 2x2 km^2 and 6 min, respectively. Henceforward, thunderstorms and cells are considered in the same way.

6.1.1 Cell identification

Horizontal identification (2D convective structures)

First, the radar images are processed in advance to remove false echoes and to identify possible 2D convective structures (hereinafter 2D structures) to be considered later in the 3D algorithm. This part of the procedure includes three main steps, which are processed in each of the 10 CAPPI levels:

- A 5 km−radius mask is applied to the radar image, centered on the locations of all the XRAD radars, to remove extremely high echoes ($\geq$ 75 dBZ). These false echoes are mainly produced by anomalous propagation, radiofrequency interferences, or other external issues, and are not related to meteorological targets.

- 2D structures (before the 3D structures) are identified with reflectivity values $\geq$ 30 dBZ, since this is the lowest value of reflectivity in the 3D algorithm. Because of this, all the echoes below this reflectivity threshold are removed (Figure 6.1a).

- Groups of pixels with less than 10 pixels (40 km^2) are removed, since these are not considered to be potential 2D structures (Figure 6.1b). In this algorithm, pixels are connected by creating areas, using a technique known as Neighbouring Pixel Labelling (NPA). This technique gives the same entity label to all the pixels connected by the sides and the vertices (8 neighbors) (Queen's case adjacency, Lloyd, 2010). Subsequently, the only requirement to be considered as a neighbor pixel is to share a vertex or a side (at least one of the possible eight connections).

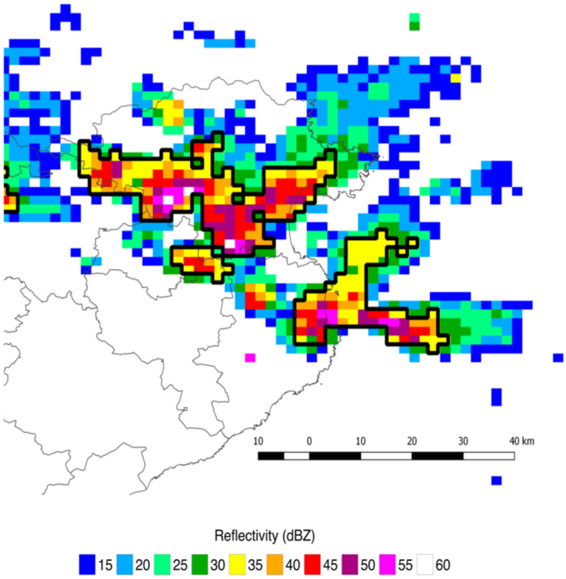

(a)

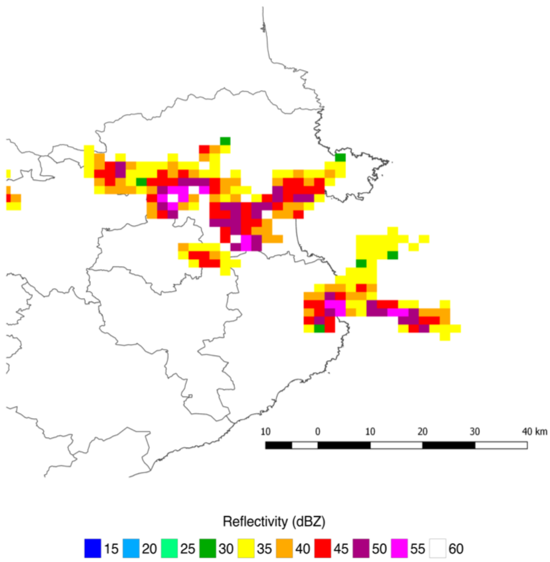

(b)

Figure 6.1: Reflectivity field for the 1 km CAPPI; (a) Original image with the 2D convective structures $\geq$ 30 dBZ enclosed with a thick black line that defines a group of pixels; (b) Final image with values $\leq$ 30 dBZ and areas smaller than 10 pixels filtered. Every group of pixels is a potential 2D convective structure or cluster.

After the pre-processing stage, the 2D convective structure identification is carried out for every group of pixels in the radar image. Following the SMC and SCIT algorithms, seven different thresholds (60, 55, 50, 45, 40, 35 and 30 dBZ) are applied at all CAPPI levels to every potential 2D structure, from the highest value to the lowest. After this, the same seven thresholds are applied again to each 2D structure as a second filter process, but this time in the opposite direction, starting from the lowest reflectivity value and increasing it through to the highest. This process makes it easier to define the dimensions of the 2D structure, rather than just delimiting the core, which, following the definition of the SMC algorithm, represents the 6 pixels with the highest value of reflectivity within each 2D structure. The new process also makes it easier to identify isolated or multicell systems (Figure 6.2). Each 2D structure is characterized by an identifier (ID), the time of occurrence (DATE and HOUR), the CAPPI level (CAPPI); the maximum reflectivity in dBZ (ZMAX), the number of pixels in the entire 2D structure (NPIX), the center of mass defined by its latitude and longitude coordinates (LON and LAT), the water content in $\mathrm{kg\,m^{-3}}$ (MA), and the number of pixels in the 2D structure core (NCORE).

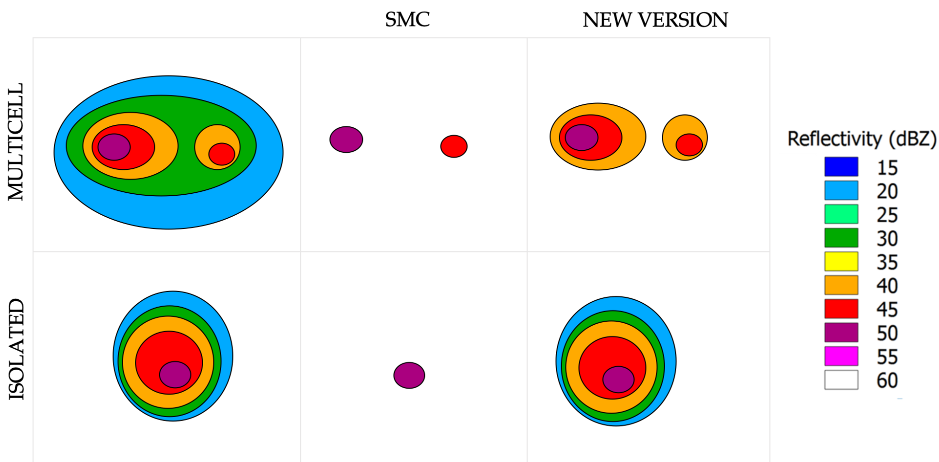

Figure 6.2: 2D structure identification using the SMC algorithm and the proposed new algorithm for a multicell system and for an isolated cell.

Vertical identification (3D cells)

The new algorithm adopts the overlapping technique of 2D structures as a new method to build the final 3D cells. This process is carried out as follows. For a better understanding, a diagram of the process is shown in Figure 6.3:

- Every identified 2D structure on a given level (i) is overlapped with all the 2D structures (one by one) on the level below ($i-1$). Hereinafter, 2D structures at level i will be referred to as $2D_i$, and 2D structures at level $i-1$ or level $i-2$, will be referred to as $2D_{i-1}$ and $2D_{i-2}$, respectively.
- If a $2D_i$ overlaps with at least one pixel of a $2D_{i-1}$, then the $2D_i$ would adopt the $2D_{i-1}$ identifier.
- In cases with multiple overlaps (with a different $2D_{i-1}$), the $2D_i$ would adopt their different identifiers (e.g. ID=ID1; ID2; ID3). Then, the algorithm will save extra information known as a Multiplicity of 2D structures (M2D) flag, that indicates at which CAPPI the algorithm found more than one associated 2D structure.
- On the contrary, if no $2D_{i-1}$ is found to be overlapping with the $2D_i$, then the algorithm would look at 2 levels below ($i-2$), applying the methodology listed above.
- Finally, if no $2D_{i-2}$ is found to be overlapping with the $2D_i$, then a new identifier is given to the $2D_i$. This would mean, for example, that a new cell has been found in the scanned volume.

The final 3D cell is built by grouping all the 2D structures with the same identifier, obtaining the following characteristics for each one: mean number of pixels over all the 2D structures that make up the 3D cell (NPIX), height of the 3D centroid in km (HCEN), height of the maximum reflectivity (HZMAX, in km), base of the 3D cell (HBASE, in km), top of the 3D cell (HTOP, in km), lowest and highest altitude at which there is a reflectivity of 40 dBZ (HBASE40 and HTOP40, respectively, in km), and 2D convective structures multiplicity flag (M2D). Since the splitting or merging of two cells is a gradual process, a valid M2D flag pattern will appear gradually at different elevations (once the cell is tracked and considered for its entire life cycle). This is seen in Section 6.2.

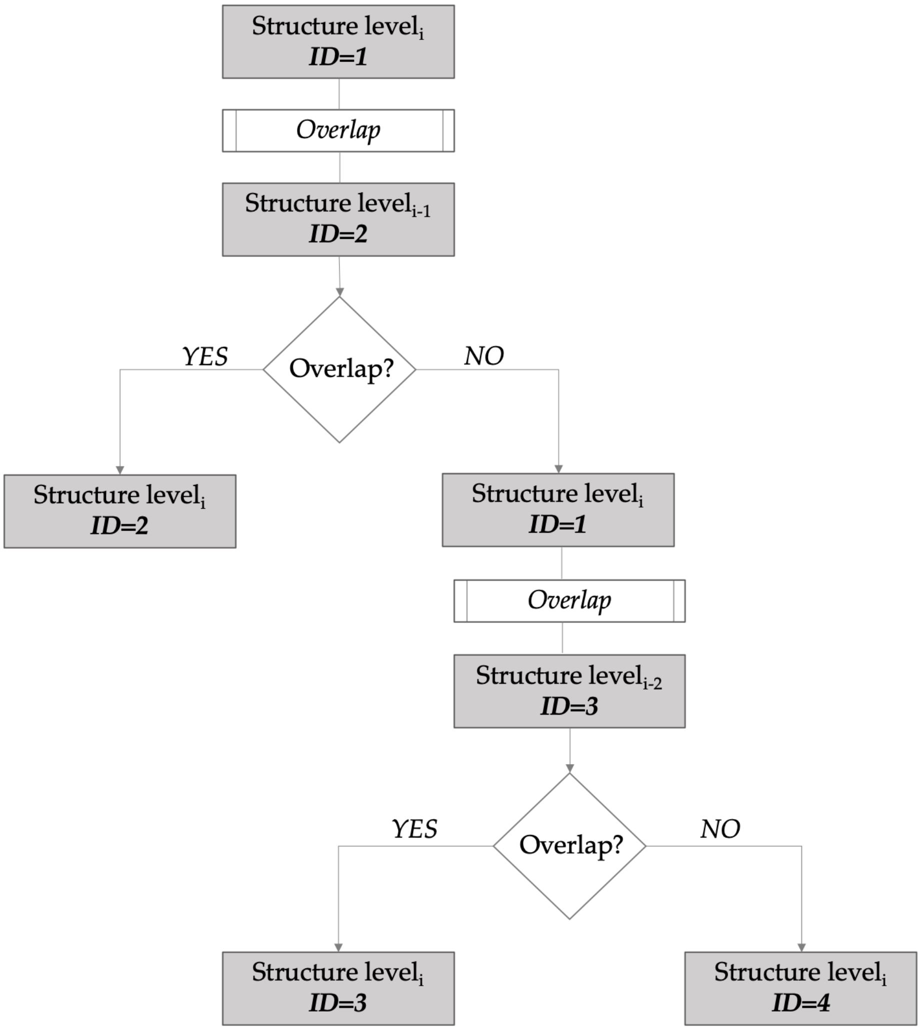

Figure 6.3: Diagram of the process followed to identify the 3D structures.

6.1.2 Cell tracking

3D cells are considered for tracking and an in-depth analysis of the life cycle when they are identified, at least, in two consecutive radar images. The new tracking scheme treats the process with two different approaches, depending on the time interval between the images to be processed. This time interval might be 6 min in case the two images (current and past) are consecutive, or 12 min in case the consecutive past image is missing. Therefore, 12 min sets the maximum time interval between possible associated centroids.

6.1.3 Cell association from consecutive images (6 min time interval)

For every 3D cell centroid identified at the current time, hereinafter known as $cell_t$, it is computed the distance to all the 3D cell centroids identified 6 min prior ($cell_{t6}$). A variable threshold, depending on the area (NPIX) of the $cell_t$, is then imposed to find the most likely association (Table 9.1). It is important to note that the dynamic threshold technique is more flexible and allows multiple associations to be identified, instead of only connecting the closest cells. If more than one $cell_{t6}$ match the distance threshold conditions, all of those cells will be associated with the actual $cell_t$. This is an uncommon occurrence that shows a Possible Merging process and will be indicated as PM (Figure 6.4). On the other hand, a splitting process will be shown through the multiplicity of the same identifier in the current tracking file, when a single $cell_{t6}$ is associated with multiple $cell_t$. This will be indicated as a Possible Splitting (PS) process. The potential occurrence of this anomalous movement is registered as a warning flag during the process, along with the identifier that the original cell (or cells) presented before the process.

Table 6.1: Variable distance thresholds depending on the area of the $cell_t$, to track the associations with $cells_{t6}$.

Area [number of pixels]	**Distance threshold [km]**
≥ 40	12
< 40 & ≥ 15	10
< 15	5

6.1.4 Cell association from the two past images (12 min time interval)

If a $cell_t$ remains non-associated after the first process, it follows an alternate pathway: connection with cells from two past images, hereinafter $cell_{t12}$. To select a distance threshold between two connected cells, the criterion followed by the SMC and SCIT algorithms has been taken into account. In these algorithms, the distance thresholds imposed during the entire tracking are dependent on the time between the images. In this sense, for consecutive images, it is assumed a cell's velocity between 5 and $21\,\mathrm{m\,s^{-1}}$. In our case, a fixed threshold of 8.5 km has been imposed which would imply a cell velocity of $12\,\mathrm{m\,s^{-1}}$, consistent with these other algorithms. Then, for cells in which the distance is $\leq$ 8.5 km, the following procedure is applied:

- The absolute variation of the HTOP40 and the ZMAX features is calculated during the 12 elapsed minutes. These two characteristics, along with the distance between $cell_t$ and $cell_{t12}$, are taken as the *change factor*, *f*.
- If there is more than one $cell_{t12}$ candidate, the $cell_t - cell_{t12}$ match (association of a cell from instant t and $t-12$) with the lowest change factor, *f*, is used as the correct association.

For example, in Figure 6.4, the procedure is applied because cell B has matched with two cells (D and E) that are < 8.5 km away. In this case, the change factors for *f1* (possible association of cell B with cell D), and *f2* (possible association of cell B with cell E) are as follows:

$$\begin{aligned} f1 &= |ZMAX_B - ZMAX_D| + |HTOP40_B - HTOP40_D| + |d_{B-D}| \\ &= 10 + 1 + 8 = 19 \end{aligned} \tag{6.1}$$

$$\begin{aligned} f2 &= |ZMAX_B - ZMAX_E| + |HTOP40_B - HTOP40_E| + |d_{B-E}| \\ &= 17 + 2 + 7.5 = 26.5 \end{aligned} \tag{6.2}$$

The smaller change factor, *f1*, which corresponds to the association of cell B with cell D. It can be seen that, in this case, the distance is not the determining factor in matching both cells; cell B and D will be connected although the distance between them is greater than the distance between cell B and cell E. In this case, cell B will take the identifier of its past cell (cell D), and the track will be traced between them. If there are no $cell_{t12}$ separated from $cell_t$ by a distance $\leq$ 8.5 km (the imposed threshold for cell association over the past 12 min), then the procedure described above cannot be applied. In this situation, the current $cell_t$ will adopt a new ID, since there is no $cell_{t6}$ or $cell_{t12}$ for the association, and it will be considered as a newborn cell (at the current time). Moreover, if this non-associated $cell_t$ presents an HTOP40 $\geq$ 7 km, it will be stored with a new warning flag called WTOP7 (Warning of HTOP greater than 7 km). This would indicate a newborn cell with a high development, which is considered an anomaly according to the results presented by Rigo and Llasat (2016). These cells must be treated as singular cases during the nowcasting process since explosive convective bubbles tend to be associated with severe weather phenomena (Senf et al., 2015).

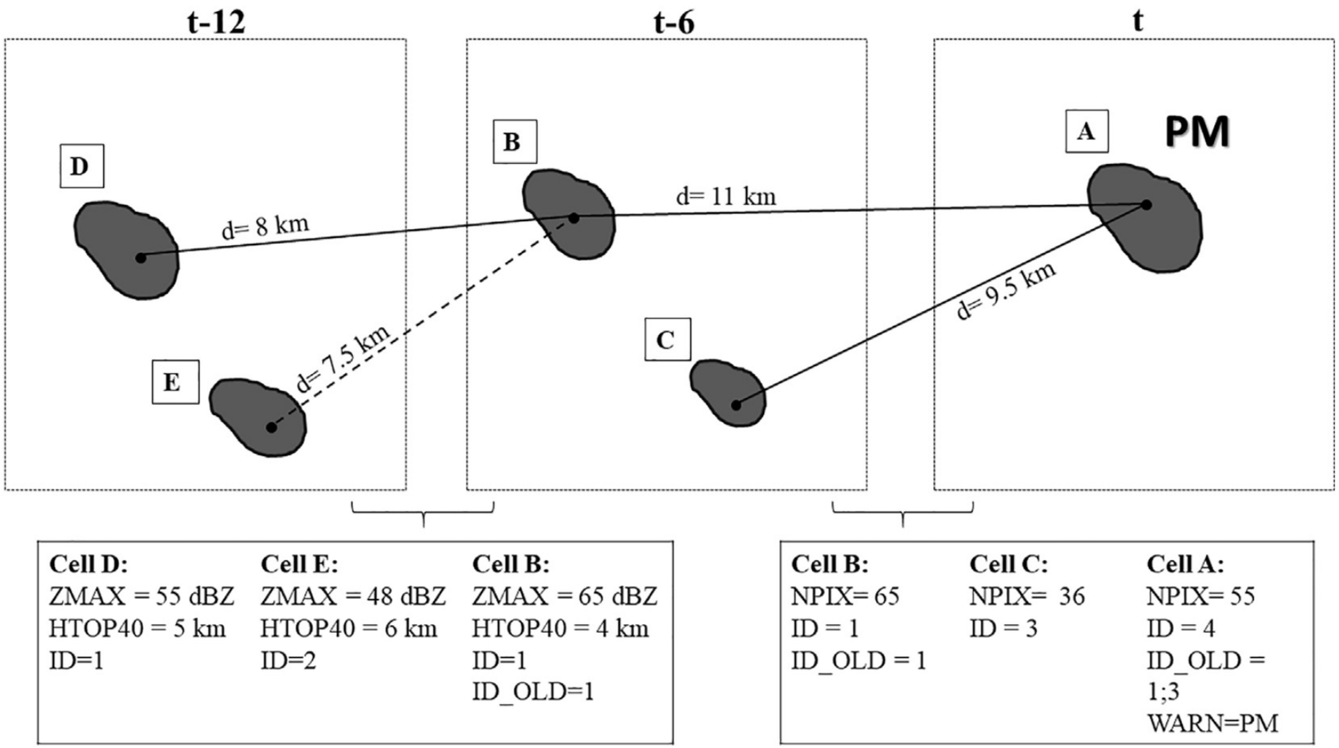

Figure 6.4: Example of cell association from one and two past images. ID indicates the current identifier and ID_OLD indicates the identifier of the past cell used for the connection. The final connections are plotted in black line and a Possible Merging, PM, process is also indicated at Cell A at current time *t*.

6.2 Application to case studies

The severe weather event of 10 July 2013 was used as an example to highlight the differences in the identification and tracking process between each version of the algorithm (Figure 6.5). However, to illustrate better the improvements in the different phases of the algorithm, two other cases of severe weather have been used: 10 July 2017, and 31 August 2017. Note that the dates of the July cases differ just from the year of the event. For this reason, to not create confusion, hereinafter the two events will be referred also as E2013 and E2017, respectively. Since the event in August 2017 is only used in Subsection 6.2.1, the entire date of the event will be written.

During the episode of 2013 (E2013, Figure 6.5), a severe thunderstorm remained quasi-stationary at least half an hour and ended in a splitting process with two main cells moving in opposite directions, producing large hailstones and severe wind gusts. The cell traveling SW became part of a multicell system when it encountered several cells developing across the western front, merging and forming a quasi-stationary linear system. More than 67 km^2 were affected by severe weather, especially by large hailstones (3 to 4 cm), which caused more than 80 % of losses in corn crops and fruit tree fields. Figure 6.5 shows the changes every half-hour in the composite radar images of the splitting and merging multicell system. Notice the white color in the core of the two splitting cells, indicating that the reflectivity is $>$ 60 dBZ, and therefore the possibility of hail.

6.2.1 Horizontal storm identification (2D structures)

Figure 6.6 shows a composite of two different CAPPI elevations for the storm of the episode E2013, 18 min before the splitting at 16:48 UTC. The composite shows the 2D structures identified with the SMC algorithm (upper panel) and the new algorithm (lower panel), represented by the area enclosed with a black line. The cell at 1 km elevation is shown to be bigger with the new algorithm, adjusting better to the thunderstorm shape. By applying two times the seven reflectivity thresholds, the structure is defined up to the lowest value possible, since there is just one single cell (instead of only identifying the core of the structure, which is the most intense area). The new algorithm maintains shape continuity and does not separate the main 2D structure into different smaller entities until strictly necessary when more than one core is found. It also identifies structures that would not be identified with the SMC algorithm (compare the fourth column in Figure 6.6). This same behavior

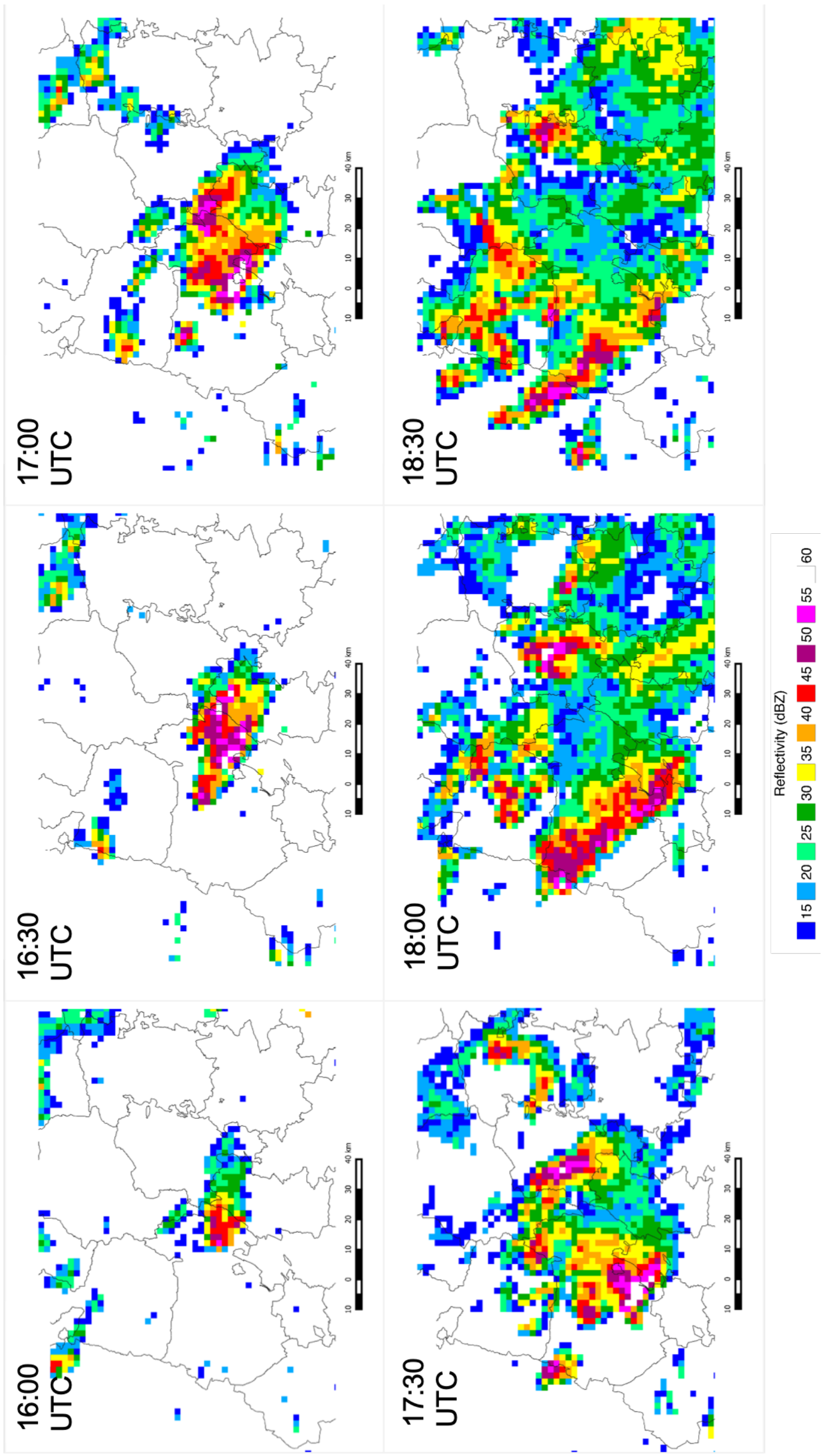

Figure 6.5: 1 km CAPPI composite image of the 10 July 2013 (E2013) episode, from 16:00 UTC to 18:30 UTC.

can be seen in Figure 6.7, which shows the case on 31 August 2017 (E2017) at 09:12 UTC.

6.2.2 Vertical storm identification (3D cells)

One of the biggest improvements to the SMC algorithm is the way 3D cells are identified through the overlapping process. Figure 6.8 shows a 3D view of the overlapped 2D structures of the splitting thunderstorm from 10 July 2013 (E2013) at 16:24 UTC. The structures of the new algorithm version are plotted in black, and the structures of the SMC algorithm are plotted in color. Due to the overlapping process, the new algorithm identifies all the structures in black as being the same. It can be seen the multiplicity of the 2D structures from 4 km to 9 km levels, indicating that the cell is splitting in two, starting from upper levels. Notice that the 2D structures at CAPPIs 6 km and 7 km coincide exactly with the 2D structures from the SMC in yellow. Nevertheless, the SMC algorithm identifies two different cells with no relation; the main cell, from level 1 km to 10 km, in red, and a secondary cell from level 5 km to 7 km, in yellow, which overlaps with the new algorithm structure in black, as stated before. The 2D structure at level 10 km, in green, is discarded because it is only found in a single CAPPI level and also because there is a gap of two CAPPIs between the closest 2D structures below, found at 7 km CAPPI. In this case, there is no overlapping of the SMC green structure and the new algorithm structure. The new algorithm can forecast the split in advance because the main cell is starting to split from the upper CAPPI levels, spreading to the lower levels until it becomes two completely different cells. Table 9.2 shows the result of identifying the 3D cell with the new algorithm. The last column shows the multiplicity flag for the 2D structures (M2D). This indicator is visible several minutes before the split (16:48 UTC), starting from the highest levels and spreading to the levels below. An M2D flag is also shown at 16:06 UTC at CAPPI 3 km, which is also an indicator that the two cells resulting from the splitting process at 16:48 UTC were being formed. The algorithm was able to distinguish two different 2D structures, matching the minimum area condition at CAPPI 3 km, unless they were not big enough to show the same pattern in other CAPPI levels. For this reason, in the proposed algorithm, the valid indicator that the split is going to take place is a gradual increase in M2D flags, from higher to lower levels.

Furthermore, the new 3D identification process allows a major continuity of the shape of the final 3D cell. To illustrate this fact, the process has been applied to an isolated severe thunderstorm on the 10 July 2017 event (E2017, Figure 6.9),

Table 6.2: Characteristics of the 3D splitting cell on 10 July 2013 (E2013) at different times. M2D values indicate the CAPPI where it is found a multiplicity. NULL values indicate that there is no flag available for that cell.

HOUR [UTC]	**LAT** [°]	**LON** [°]	**AREA** [km2]	**HCEN** [km]	**ZMAX** [dBZ]	**HBASE** [km]	**HTOP** [km]	**HBASE40** [km]	**HTOP40** [km]	**M2D** [flag]
1530	1.31	41.93	14.2	6	51.5	1	6	1	4	NULL
1536	1.28	41.93	15.8	5	49.0	1	8	1	7	NULL
1542	1.25	41.92	14.7	6	53.0	1	7	1	6	NULL
1548	1.23	41.90	25.6	6	50.5	1	9	1	7	NULL
1554	1.22	41.89	33.4	4	50.0	1	9	1	8	NULL
1600	1.20	41.89	43.9	2	51.5	1	10	1	10	NULL
1606	1.19	41.89	57.0	3	55.5	1	10	1	10	3
1612	1.20	41.89	77.6	6	56.5	1	10	1	10	NULL
1618	1.21	41.89	66.1	5	60.5	1	10	1	10	9;10
1624	1.21	41.88	33.4	5	61.0	1	10	1	10	4;5;6;7;8;9
1630	1.20	41.88	17.9	4	60.5	1	10	1	10	1;2;3;4;5;7;8;9
1636	1.13	41.90	24.1	5	63.0	1	10	1	10	1;2;3;4;5;6;7;8;9
1642	1.16	41.90	50.9	5	62.5	1	10	1	10	2;3;4;5;6;7;8;9

a convective episode that produced several severe thunderstorms throughout the day. This was carried out to better visualize the entire overlap of the cell, which is difficult to discern for a multicell system. Due to the uninhabited area affected by the thunderstorm, there is no record of surface hail impact, unless the probability of hail was greater than 90 % during almost the entire life cycle (see Rigo and Llasat, 2016; Farnell et al., 2017, , for more details). The figure shows the evolution of the contours of the aforementioned 3D isolated cell (color lines) and its overlapping area (thick black line), for the proposed new algorithm (Figure 6.9a) and the SMC algorithm (Figure 6.9b). In the new algorithm overlap, a broader central area can be seen, coinciding with the mature stage of the thunderstorm, with the head and tail of the shape slightly narrowed, corresponding to the development and dissipation stages. On the other hand, the SMC overlap is continuous in shape, making it impossible to distinguish between different thunderstorm phases.

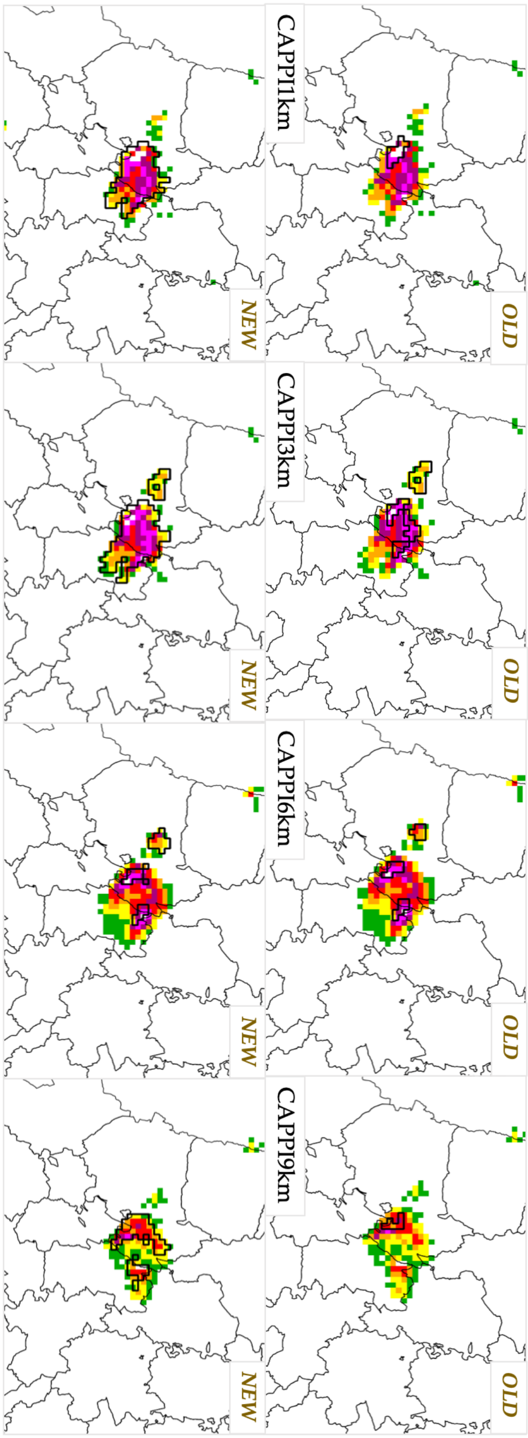

Figure 6.6: 2D structures (enclosed with a black line) from the 10 July 2013 (E2013) case at 16:24 UTC, identified with the new algorithm (lower panel) and the SMC algorithm (upper panel).

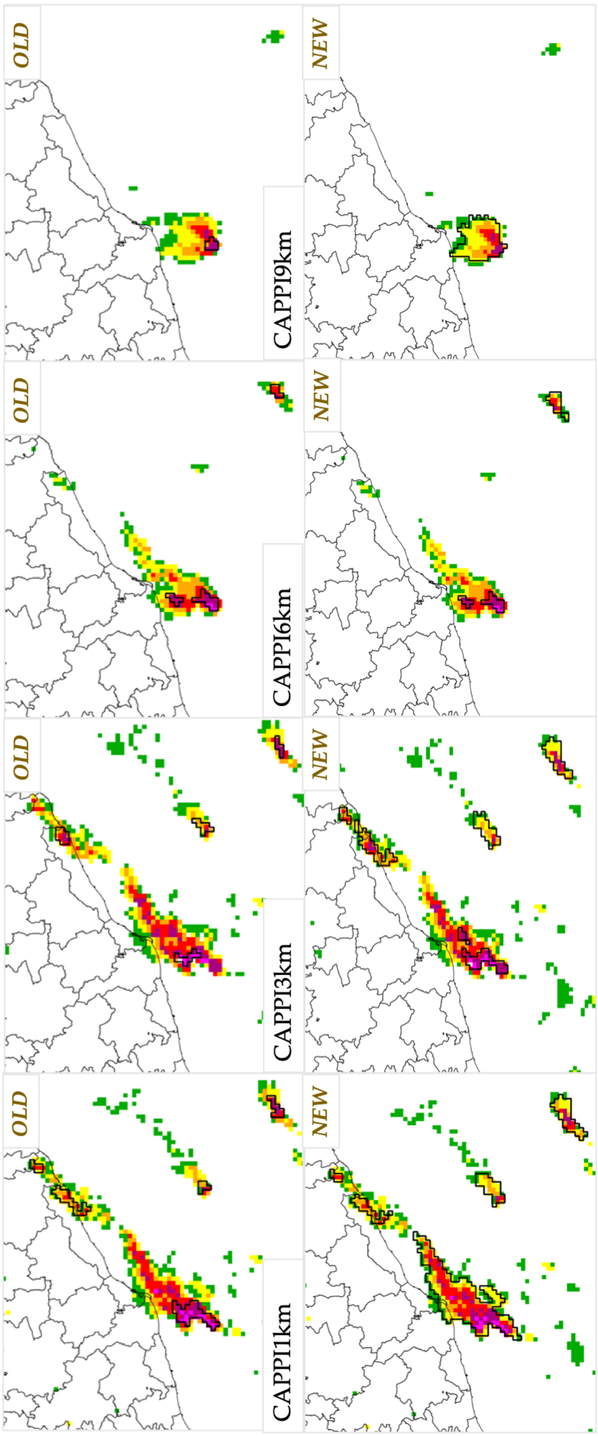

Figure 6.7: 2D structures (enclosed with a black line) from the 31 August 2017 case at 09:12 UTC, identified with the new algorithm (lower panel) and the SMC algorithm (upper panel).

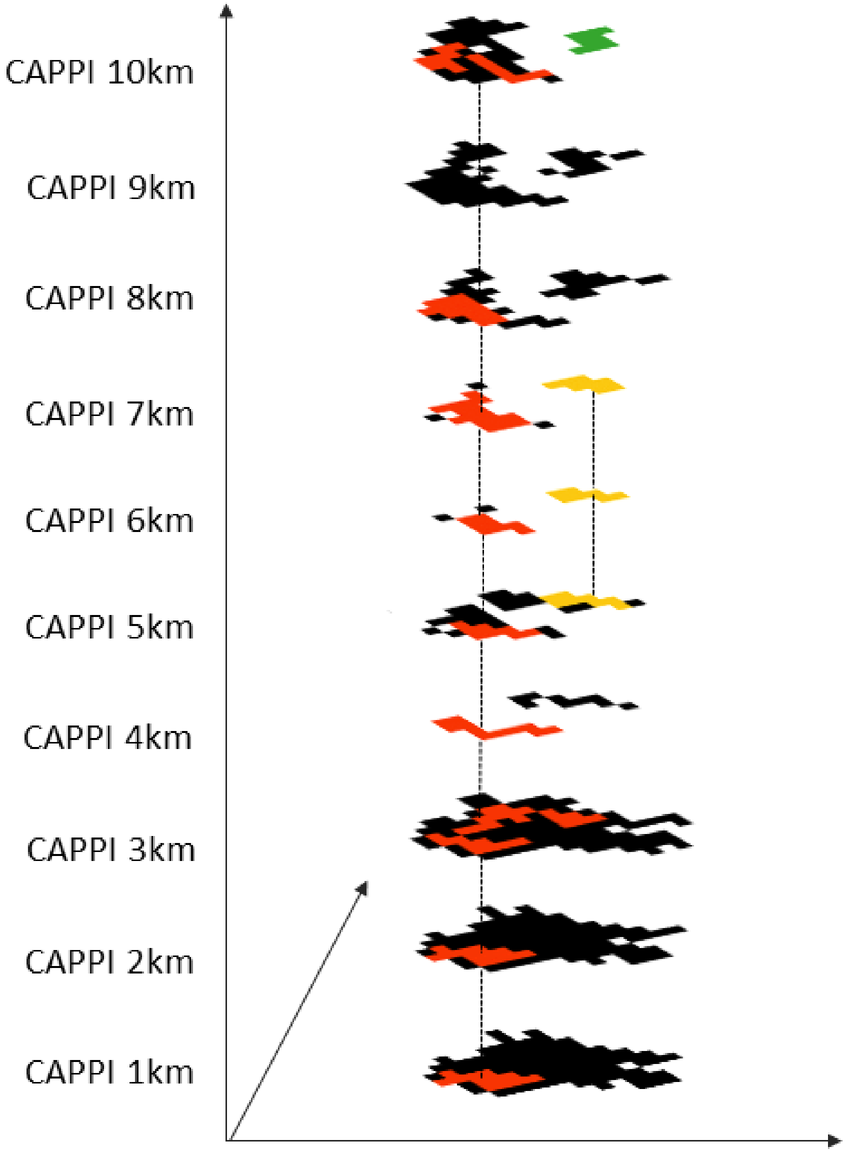

Figure 6.8: 3D view of the 2D structures of 10 July 2013 (E2013) at 16:24 UTC. Structures from the new algorithm are plotted in black and structures from the SMC algorithm are plotted in colour.

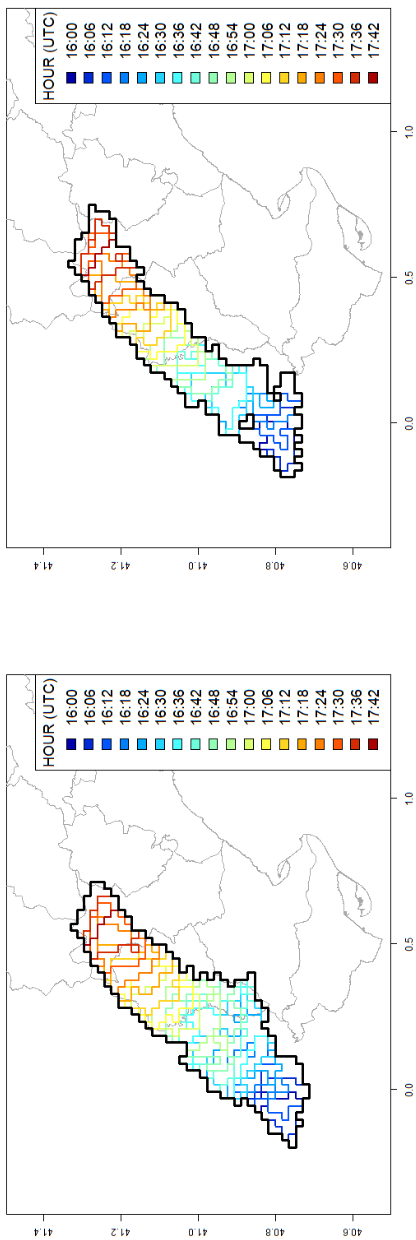

(a)

(b)

Figure 6.9: (a) Shapes for the isolated cell of 10 July 2017 (E2017) during its lifespan for the new algorithm and (b) for the SMC algorithm. An overlap of the entire life cyclecycle shape is displayed in thick black line.

6.2.3 Tracking

Figure 6.10 shows the identified and tracked cells from the multicell system on 10 July 2013 (E2013), which showed splitting and merging processes, with the SMC and the new algorithm. The new algorithm (Figure 6.10b) retrieves five different tracked cells which took part in the system, with the start location of each cell indicated with a circle. It is easy to discern the quasi-stationarity of the initial "mother" cell (cell 1), as well as the corresponding resulting cells after the splitting process, which moved in opposite directions. In this sense, two PS (possible splitting process) flags are shown when the "daughter" cells (2 and 3) are identified for the first time. Also, once cell 4, moving from NW to SE, encounters cell 3, which results from the splitting process and moves towards SW, a Possible Merging (PM) flag is issued. This means that a merging process has taken place. The resulting cell from the merging process, cell 5, moves towards SE unless in the first minutes it seems to have a little backward propagation. On the other hand, the SMC tracking (Figure 6.10a) only detects three cells, and cannot identify the splitting and the merging processes. It also fails to show warning flags for anomalous movement. In this sense, the new algorithm is capable of separating different entities within the same linear system, and therefore to see the weaker cell appearing to the east (cell 4 in Figure 6.10b), which is part of the entire linear system. This is a direct result of no longer tracking just the core of the cell, but tracking the linear system as a group of different interacting entities. In the case of the SMC, the potential occurrence of small cells growing in the vicinity can't be identified, and the movement of the system seems to present a backward propagation to the west (see the time indicator in cell 3 in Figure 6.10a).

The evolution of some characteristics of the tracked cells resulting from both algorithms is presented in Figure 6.11. The characteristics shown for the new version of the algorithm are ZMAX, in dBZ, and the HTOP40, in km, and the HTOP12, also in km, for the SMC algorithm. This is shown because the same HTOP was not stored for both algorithms (different top reflectivity thresholds). However, in this case, the cells are highly developed and intense, so the top heights (for 12 and 40 dBZ) are comparable. Figure 6.11c and Figure 6.11d show how the thresholds applied in the new algorithm, as well as the constrains on HTOP40 and ZMAX parameters allow, once again, to get better continuity of the cells' characteristics, which are maintained also when anomalous processes are identified. This allows getting a more realistic path and life cycle of the thunderstorms in question. It is easy to see how there is a growing phase for the initial cell that is maintained

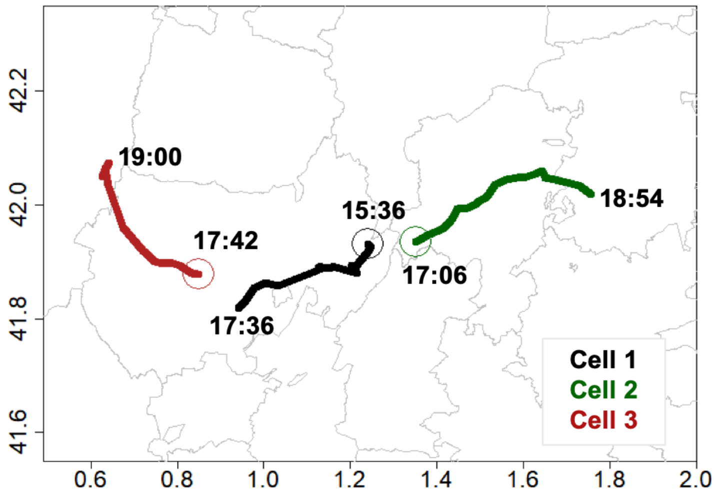

(a)

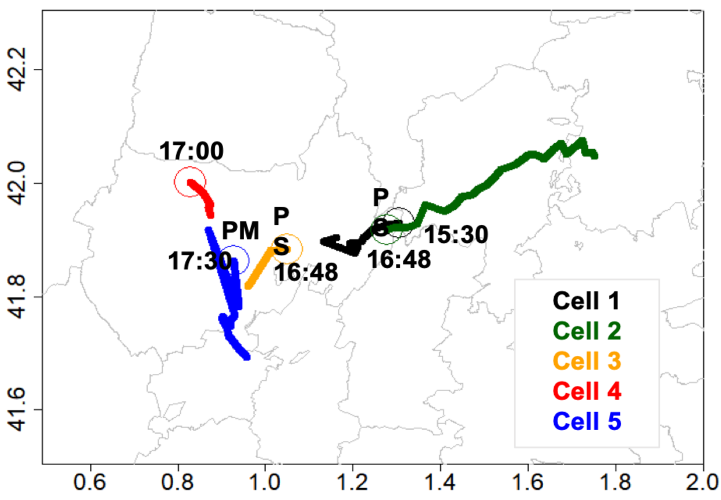

(b)

Figure 6.10: Result of tracking the cells involved in the splitting and merging multicell system of 10 July 2013 (E2013). (a) SMC algorithm with start and end times of the cells; (b) new algorithm with start time of the cells and anomalous movement flag. For both pictures, the starting time is also indicated with a circle around the centroid.

during the mature phase when the split occurs. After the split, it can be seen how the "daughter" cells are identified in a growing phase, with less intensity than the preceding "mother" cell, reaching their peak when the merging process occurs.

Finally, the decaying phase of the remaining cells after the splitting process is shown, corresponding to the dissipating stage. On the other hand, Figure 6.11a and Figure 6.11b show how two of the cells identified and tracked by the SMC (green and red in the figure) algorithm start with high reflectivity values (above 55 dBZ) and with an HTOP12 greater than 10 km. The decaying phase can be seen shortly afterward, suggesting that both cells were identified late and that their growing phase is masked in the growing phase for cell 1 (in black), constituting an incorrect path.

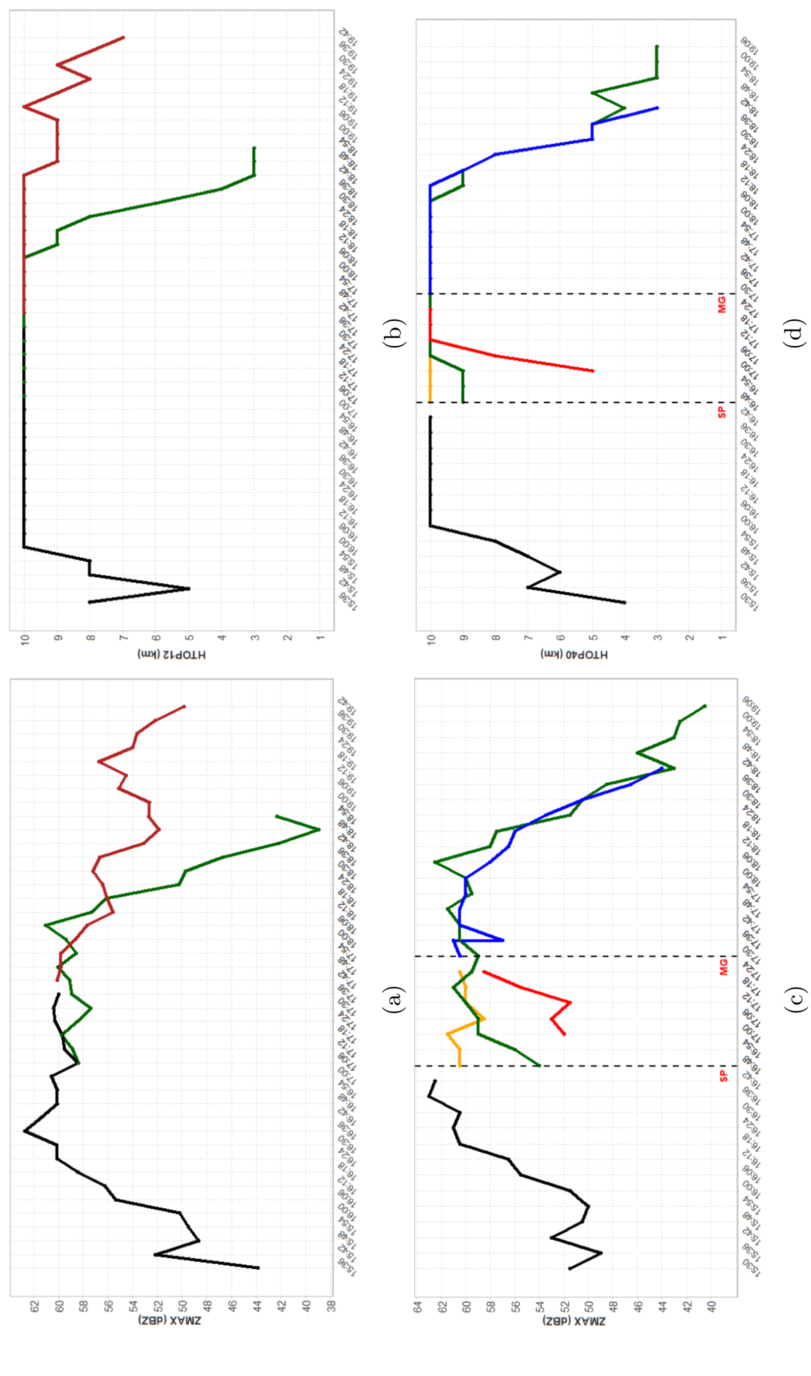

Figure 6.11: Evolution of the cell characteristics on 10 July 2013 (E2013) resulting from the SMC algorithm (upper panel) and the new algorithm (lower panel). (a) ZMAX in dBZ and (b) HTOP12 in km for the SMC algorithm; (c) ZMAX in dBZ and (d) HTOP40 in km for the new algorithm. Vertical dotted lines show the splitting and merging time in the new algorithm, as well as SP and PM flags over the tracks.

6.3 Conclusions

This chapter proposes a new methodology for the radar-based 3D identification and tracking of convective cells, which makes it possible to identify anomalous movements of thunderstorms. It enhances the current operative algorithm used by the Meteorological Service of Catalonia. First, for the identification process in each 2D level, the new algorithm adds an image pre-processing stage, involving filtering the extremely intense echoes around the radar position, and filtering possible 2D convective structures close to 30 dBZ that are smaller than 10 pixels ($40\,\mathrm{km}^2$). This gets rid of false echoes that could result in a *pseudo* cell identification. The previous horizontal identification of the structures is modified, adding a different rule for pixel grouping (Queen's case), which has proved to be a less restrictive method when retrieving 2D structures. A second seven-reflectivity bottom-up thresholding technique allows for a better distinction of the cells embedded in multicell systems or highly-dense convective day. This allows to not discard small cells growing near those that are more developed.

Second, in the 3D identification module, an overlapping technique has been introduced. This has been shown to facilitate the knowledge of possible internal processes, by analyzing the multiplicity of 2D structures (M2D) in different CAPPIs throughout the entire 3D volume. Due to the complexity of thunderstorm formation and the several factors that can vary their behavior throughout their life cycle, a good knowledge of their volumetric structure is essential to describe the organization of convective cells and the possible interactions between them. It is also important to know whether a potential growth of new cells on the storm flank is going to happen, because it helps to foresee if other factors might have a significant impact on the motion of the storm (in terms of direction and speed), besides wind advection. This, as well as obtaining in advance information on possible anomalous movements (splitting or merging, in this case), is crucial for forecasters during a human-based tracking of severe storms in an operative environment.

Finally, in the new tracking module, the connection of 3D cells is done by varying the distance thresholds depending on the area of the cell being tracked. Furthermore, cells not connected with the past image (6 min) are analyzed through a completely new process, where the minimum variation of some characteristics is imposed. It is important to remark that this process is not contradictory to the results from Tsonis and Austin (1981), since a fixed trend is not imposed, and parabolic curves are not used to extrapolate future echo sizes. The new method is applied for cells that are not connected with the past image, and that would result in incorrect connections if static distance thresholds were imposed. Also, although the aim is not to see such a large variation in the absolute value of the cell's area and reflectivity in a time interval of 12 min, a pattern of growing, developing and decaying life cycle is not followed. This tracking method has worked very well in tracking thunderstorms that were born very close to others in a different phase of development, and for tracking anomalous movements. Sometimes, a cell may appear in the path of another cell in a different life stage (mature or dissipating, for instance). By imposing a centroid distance threshold technique to connect the cells, both the mature and developing cells will appear to be the same cell and a false path might be built. Applying different thresholds based on the area of the cell, and with a minimum variation of the HTOP40 and ZMAX characteristics in the case of those not connected with the image 6 min before, it is possible to create a more realistic track.

The most remarkable improvement of this new algorithm is that it can identify, in advance, if possible anomalous movements are going to happen, and to provide early warnings during the identification and tracking process, which will improve the decision-making process in an operative environment. In future research, it is important to apply the new algorithm to a wide database, to discern between valid warning flags, as well as test the M2D, PS, and PM occurrence in anomalous and normal propagation cases. Furthermore, we cannot ignore that, since some years ago, the combined data from radar networks and lightning have been used to nowcast severity in thunderstorms (e.g. Bonelli and Marcacci, 2008; Schultz et al., 2009; Yang and King, 2010), because lightning gives additional information about onset and evolution of thunderstorms, severe weather and heavy rainfalls (e.g. Rigo et al., 2010; Yair et al., 2010; Price et al., 2011; Rigo and Pineda, 2016). In this sense, the new tracking algorithm should be a tool running in parallel with lightning information to search for signatures that could help to identify the occurrence of phenomena associated with anomalous trajectories and severity.

7

Validation of the radar-based algorithm with severe weather cases

* The present chapter has been adapted from: del Moral, T. Rigo and A., M.C. Llasat 2018: Performance of a new algorithm for nowcasting anomalous trajectories. In *Proceedings fo the 10th European Conference on Radar in Meteorology and Hydrology (ERAD 2018): 1-6 July 2018, Ede-Wageningen, The Netherlands*, Wageningen University and Research - 983

To demonstrate the performance of the new radar-based algorithm from Chapter 6 and its capabilities, this short chapter presents a validation over 30 severe weather thunderstorms affecting Catalonia between 2007-2016. These cases were obtained from the severe weather database explained in Chapter 4 . It is mainly focused on splitting and merging processes, since these occur in isolated and severe thunderstorms, and constitute the base for a good validation of the algorithm. To see how the algorithm performs in convection embedded in bigger systems, and how it deals with highly-dense convective days, the reader is referred to Chapter 8 (coastal convection).

7.1 Dataset

As stated before, for the present validation it has been selected 30 different severe weather cases from the SMC internal database (Rigo et al., 2015; Farnell et al., 2017, presented in Chapter 4). All the episodes reported damages due to severe weather phenomena and, in most of the cases, there were proofs of anomalous propagation in, at least, one of the cells involved in the phenomena (visible in radar images). In total, the dataset for the validation was formed by 20 hail cases, 8 cases presenting severe-wind gusts (downburst or gust front), and 2 tornado cases (Table 9.1). The cell tracks and weather phenomena associated with the thunderstorms are shown in Figure 7.1. Notice that most of the events occurred inland, in plain areas or near steeped mountain ranges. Figure 7.2 presents example cases with radar images, where the severe thunderstorms that presented anomalous propagation are framed in purple polygons.

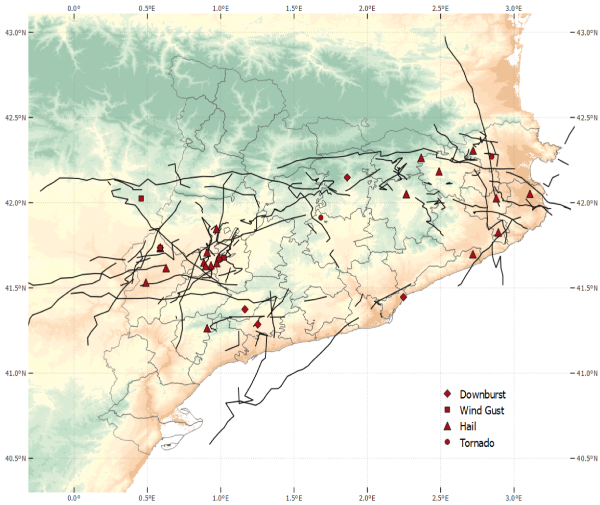

Figure 7.1: Map showing the region of study (Catalonia) with the tracked cells involved in the analyzed cases.

Table 7.1: List of the analyzed cases of severe weather, with date and time of occurrence (in UTC) and type of phenomenon at surface. Hail cases with asterisk also recorded strong wind gusts.

Date	**Time [UTC]**	**Type of phenomeon**	**Date**	**Time [UTC]**	**Type of phenomeon**
17/09/2007	1500	Hail	23/06/2015	1630	Hail
31/08/2011	1300	Hail	22/05/2016	1330	Downburst
05/07/2012	1630	Hail	16/08/2016	1930	Hail
27/07/2012 (a)	1700	Hail	09/09/2016	2200	Downburst
27/07/2012 (b)	1730	Hail	13/09/2016	2330	Downburst
18/06/2013	1400	Hail*	14/10/2016	1330	Hail
10/07/2013 (a)	1600	Gust Front	14/10/2016 (b)	1430	Hail
10/07/2013 (b)	1730	Hail	11/05/2017 (a)	1230	Gust Front
19/07/2013	1430	Hail	11/05/2017 (b)	1900	Gust Front
02/07/2014	1630	Hail	06/07/2017	1600	Hail
04/09/2014	2330	Downburst	10/07/2017	1700	Hail
06/09/2014 (a)	1600	Hail*	18/10/2017	1900	Hail
06/09/2014 (b)	1630	Hail	18/10/2017	2000	Downburst
14/09/2014	1430	Hail	07/01/2018	0100	Tornado
15/09/2014	1530	Hail	07/01/2018	0730	Tornado

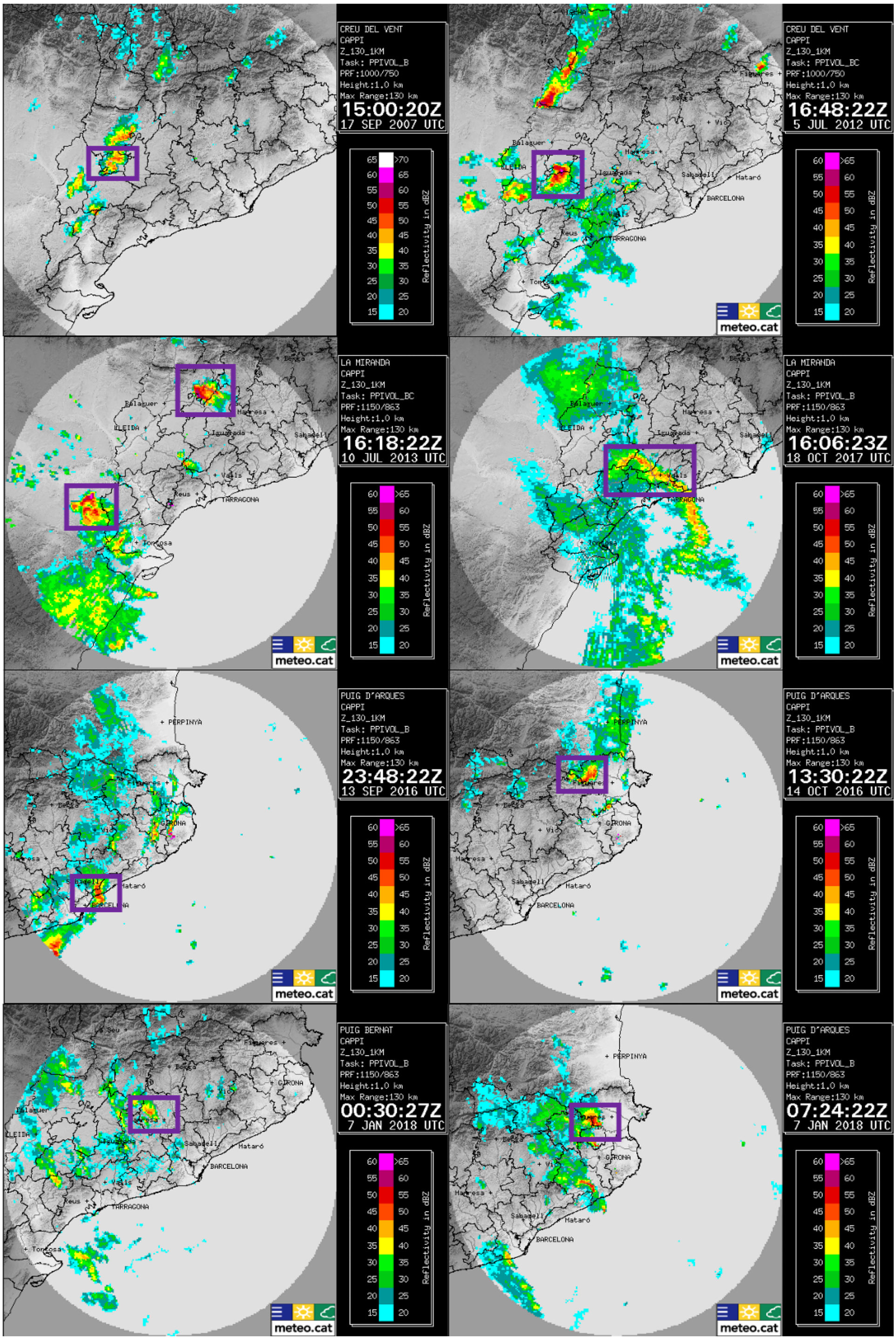

Figure 7.2: Some examples of the radar structures (inside the purple rectangle) that produced severe weather phenomena in different episodes.

7.2 Methodology

To analyze the thunderstorms for each one of the cases, it has been used the algorithm presented in Chapter 6, that, as stated before, runs over the volumetric SMC CAPPI product. In this sense, the algorithm has been performed over a total of 7,200 volumetric CAPPIs, as it has been used to analyzed and distinguish all the thunderstorms happening in the episode and not just the severe ones.

The analysis of the cases has been done mainly in three steps; visual recognition of the thunderstorms' propagation; automatic detection and tracking of the radar convective cells with the new algorithm, and the final verification. During the first stage, it has been necessary to rigorously visually identify the propagation of all the cells involved in each case of study. This has meant to analyze each radar animation, discerning whether a thunderstorm was suffering a split/merge process or not, identifying the time, the type of movement, and the number of cells involved. For those days where there was a dense convective activity, it has been more difficult to identify each severe phenomenon with its causing thunderstorms. In these cases, it has been imposed the rule of selecting the closest cell to the observation spot, the maximum of the reflectivity field (i.e. $\geq$ 60 dBZ in cases of hail), and the shape of the cell (i.e. the bow echo in cases of severe wind). It is important to remark the issues of a human-based visual recognition and tracking of shapes which, according to Rasmussen and Hager (2001), can be divided into three problems; *agile motion*, when the object movement exceeds the dynamic prediction abilities of the tracker person; *distraction*, when another object has a similar shape to the object being tracked; and *occlusion*, when another scene element is interposed between the tracker and the object tracked. Furthermore, orographic blocking, electronic interferences, or precipitation attenuation, among other factors, may occasionally lead to visually recognize false split or merge processes. In the present study, we have tried to minimize these handicaps.

7.2.1 Warning identification

The possible algorithm-derived warnings that may conclude in the identification of a split/merge process, which are used in the present work, are resumed in Table 9.2. It is important to remark that these appear at different stages of the algorithm. For instance, several M2D warnings in the 3D identification module, with an increasing frequency pattern before a split or merge process, will be considered as the *in-advance indicator* that some anomalous movement may take place with the cell. Besides, the M2D pattern may finally be accompanied with a PS and/or PM warning in the tracking module if it results in this kind of pattern. Finally, if all of the above fails, the emergence of a cell with high development during the tracking (for instance, with HTOP greater than 7 km, WTOP7), will be considered as an indicator that the cell could be resulting from a splitting process, since a gradual growth pattern is expected. This can be seen in Figure 7.3, which presents a correctly identified splitting process during the tracking module, where both "daughter" cells show an SP flag (Figure 7.3a). On the other hand, a different splitting process that has not been identified with the previous SP warning can be guessed in Figure 7.3b, where a final WTOP7 warn has appeared over one of the resulting cells.

Table 7.2: Different possible indicators, and time of occurrence in the algorithm, of splitting and merging. M2D is the "Multiplicity of 2D structures" of a CAPPI appearing in the 3D identification; PS and PM are "Possible Splitting" and "Possible Merging" flags, respectively, appearing in the tracking module; WTOP7 ("Warning of HTOP greater than 7 km"), also shown in the trakcing module, represents a warning indicating that the 'newborn' cell top is, at least, 7 km high.

Indicator/flag	**Time to split or merge**	**Module**	**Evaluation**
M2D	Before occurrence	3D identification	Prognosis
PS/PM flag	On time	Tracking	Diagnosis
WTOP7	After occurrence	Tracking	Diganosis

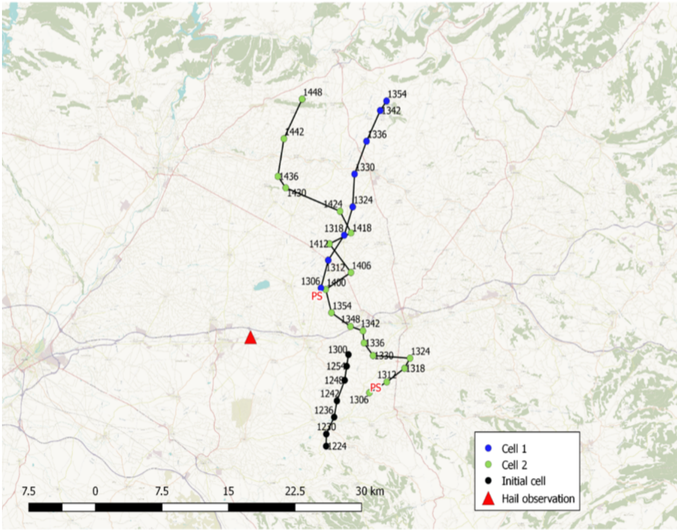

(a)

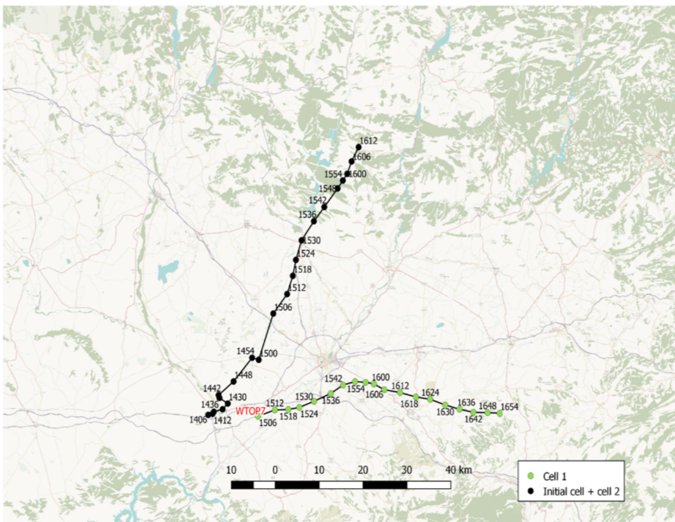

(b)

Figure 7.3: (a) Correct PS/PM warning displayed in the tracking module (first chance); (b) WTOP7 warning displayed when incorrect identification of a PS process is done (second chance).

7.2.2 Analysis

The entire analysis has been divided into two sections; evaluation of the M2D warnings (prognosis), and evaluation of the PS/PM and WTOP7 warnings during the tracking module (diagnosis). All cells identified with no anomalous movements are, hereinafter, defined as NAM. It must be explained that he WTOP7 warnings don't necessarily represent exclusively cells resulting from merging and splitting processes but, for instance, these can also represent cells that have been identified as new ones because the tracking has failed, or for missing radar data during consecutive images.

The verification has been done through a two-step dichotomous forecasting verification (Yes/No) (Table 7.3). This has allowed us to study the capability of the algorithm to show the PS/PM warnings as a first step and, in case of failure, to identify the possible anomalous movement with a second chance (showing the WTOP7 warning). The first dichotomous verification has considered the visual recognition of split/merge processes in the radar animation to be the *observed* sample, and the PS/PM warning flags during the tracking module, to be the *forecasted* sample. The second one (Table 7.4), has only considered the resulting "forecasted NO" from the first verification, to be the total sampling (no PS/PM flag in the tracking module), and has taken the WTOP7 flags as the new *forecasted* sample, comparing it against the visual recognition of split/merges (*observed* sample). This second verification has been done to prove the capability of having some type of information when an anomalous process takes place, even if the first indicator has failed.

Table 7.3: Contingency table followed to evaluate PS/PM warnings (first verification).

PS/PM Warning in Tracking module	**PS/PM Observed in Radar Animation**	
	YES	*NO*
YES	Hits (12)	False Alarms (1)
NO	Misses (6)	Correct Negatives (11)

Table 7.4: Contingency table followed to evaluate WTOP7 warnings (second verification).

WTOP7 Warning in Tracking module	**PS/PM Observed in Radar Animation**	
	YES	*NO*
YES	Hits (5)	False Alarms (1)
NO	Misses (1)	Correct Negatives (10)

The accuracy and the skills of the method have been tested with the Probability of Detection (POD), Probability of False Detection (POFD) and Peirce's Skill Score (PSS) indexes described below (Wilks, 2011). The first two, indicate how well our algorithm can forecast a split or merge that has happened in real life, and what is the probability to fail such identification when it has not happened, respectively. The latter, the PSS, indicates the skills of the algorithm in distinguish when a split or merge process happens or not:

$$POD = \frac{hits}{hits + misses} \tag{7.1}$$

$$POFD = \frac{false\ \ alarms}{correct\ \ negatives + false\ \ alarms} \tag{7.2}$$

$$PSS = POD - POFD \tag{7.3}$$

7.3 Results

More than 75 % of the cases were recorded during the JASO period (July, August, September and October), and almost 90 % was related to the diurnal cycle (took place Post Meridian, from 12 to 00 UTC). Table 7.5 summarizes the 30 cases characteristics depending on the propagation and phenomena presented:

Table 7.5: Studied cases according to type of movements and severe weather event; Possible Splitting (PS), Possible Merging (PM) and Non-Anomalous Movement (NAM).

Type	**PS**	**PM**	**NAM**
Hail	7	6	7
Downburst/Gust Front	2	3	3
Tornado	1	0	1

7.3.1 M2D evaluation and patterns (identification module)

As stated in Subsection 7.2.1, M2D flags are displayed during the 3D identification process, representing a prognosis indicator that a possible split/merge will happen. This is always emitted when a 3D cell in a given time of its life cycle, has more than one 2D structures in the same CAPPI level. Figure 7.4a shows the frequency of occurrence of M2D flags emitted for the observed 19 cells that presented either a PS/PM process. The 63.2 % of the cases (12) contained M2D flags before the split or merge process, representing a good indicator that something could occur with the cell; 10.5 % of cases (2) presented M2D flags in a moment of the entire life cycle of the cell, and another 2 cases presented M2D at the moment of the split or merge. Finally, 15.8 % cases (3) did not present any M2D flag.

Furthermore, in all the cases except those with no flag, M2D warnings were visible not only in one moment of the entire life cycle but also in consecutive images, with a 30 min-lead time (mean value). For instance, Figure 7.4b shows the consecutive M2D flags of the splitting cell on the 10th July 2013 case (previously analyzed in Chapter 6, visible 30 min before the split process, where it also can be distinguished a top-down pattern of occurrence. The first M2D flags are registered at CAPPIs 9 and 10 km, and then it starts to descend to lower CAPPIs until almost all the CAPPIs register M2D flags. It is also found an M2D flag at CAPPI 3 km, 42 min before the split, which has not been considered valid. This type of pattern was common in some cases, but not all the cases presented a clear top-down or bottom-up pattern.

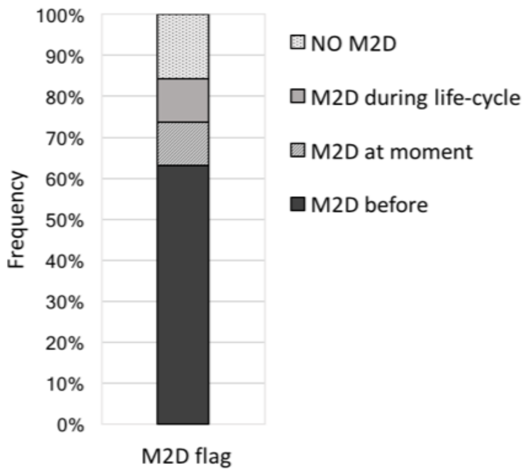

(a)

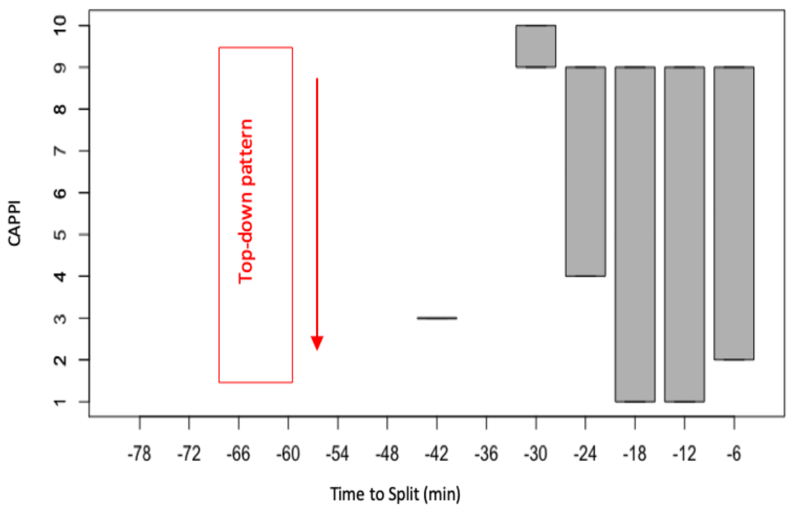

(b)

Figure 7.4: (a) Frequency of the moment of occurrence of M2D flags in PS/PM cells;(b) M2D flags pattern for the splitting cell on 10 July 2013. Grey bars represent the extension of the M2D flag in the entire volume (CAPPIs with multiplicity).

7.3.2 Performance of the PS/PM and WTOP7 warnings (tracking module)

Table 7.6 shows the skill scores for the evaluation of the different possible warnings displayed in the tracking module. It can be seen how the new tracking scheme detected correctly the PS/PM process of 63 % of the cases observed (POD = 0.67), and only the 8 % (POFD = 0.08) of the cases where incorrectly warned. This results in a good ability (PSS=0.58) of the algorithm to separate PS/PM and NAM events (notice that the PSS score is comprised between -1 and 1, and a 0 indicates no skill). Moreover, if the first chance of warning does not appear, a second chance is available if a WTOP7 warning is issued. In this case, the results show that 83 % of the cases that were not detected at first, presented a WTOP7 warning in the "daughters" cells.

Table 7.6: Skill scores for the evaluation of PS/PM warnings (first chance) and WTOP7 warnings (second chance) in the tracking module.

Skill	**PS/PM**	**WTOP7**
POD	0.67	0.83
POFD	0.08	0.10
PSS	0.58	0.73

7.4 Conclusions

This chapter shows the results obtained from the validation of the new version of the 3D identification and tracking algorithm (del Moral et al., 2018b) over 30 severe weather cases in Catalonia. The new algorithm identifies and tracks the convective cells in a better way that the current operative in the SMC, to anticipate an anomalous movement (split or merge), and to perform more realistic tracks of all types of cells. In this way, the algorithm has been validated from two perspectives; the capability to foresee split or merge movements in the 3D identification module (M2D warnings), and the capability to identify split or merge movements in the tracking module (PS/PM and WTOP7 warnings). The forecast verification shows that almost 85 % of the cases with anomalous movements presented M2D warnings, in some stage of their life cycle, and that more than 65 % where displayed in advance (30 min lead-time in average), constituting a good tool to foresee this type of processes.

As seen from the splitting case on 10 July 2013, it is expected that a split or merge of a cell will appear gradually in time. In the present study, most of the splitting cases presented a top-down pattern with M2D warnings, spreading from upper to lower CAPPI levels. However, it is necessary to conduct more studies on merging thunderstorms, since it wasn't able to distinguish a valid pattern of M2D (expected bottom-up anomaly propagation against the top-down propagation that sometimes is found).

Finally, the results also demonstrate that the tracking is the module that works better since it has two chances of anomalous movement identification. As a first stage, the POD score resulted in 0.63, which was increased to 0.83 when the second stage (WTOP7 warnings) was performed. This allowed us to correctly identify the split or merge process seen previously in the identification module (M2D), with great accuracy.

The results are promising, but the validation needs to include a wider dataset with cells also involved in heavy precipitation events. That is the reason why in Chapter 8 it is presented an application of the algorithm in a touristic area, with another convective type regime and with flash flood-producing thunderstorms. Future research should include some work to discern whether it is possible or not to find an M2D flag pattern for merging storms, as well as to know the differences on the cells' characteristics when identified with the new algorithm or the SMC version, to find strong and weak points to improve.

8

Connecting coastal flash flood events with radar-derived convective storm characteristics

* The present chapter has been adapted from: del Moral, A., M.C. Llasat and T. Rigo, 2020: Connecting flash flood events with radar-derived convective storm characteristics on the northwestern Mediterranean coast: knowing the present for better future scenarios adaptation *Atmos. Res.*, 238, 104863, doi: https://doi.org/10.1016/j.atmosres.2020.104863, ©Elsevier. Used with permision.

The work presented here aims to start investigating some of these outstanding questions in a region of the Catalan coast which has been identified as a risk area associated with an elevated number of flash flood events and high vulnerability

(Cortès et al., 2018). For instance, what are the characteristics of the convective cells affecting the region (e.g. vertical development, duration, and propagation)? Are cells related to deep or shallow and more efficient convection? Do cells remain relatively shallow with efficient microphysical precipitation processes, or do they instead grow into deep convective towers? What is the role of the sea and the topography in cell initiation and motion? Are flash floods strictly related to in situ high rainfall rates?

As part of the Spanish project M-CostAdapt (CTM2017-83655-C2-2-R), and therefore a part of the Mediterranean community, our main goal is to utilize a radar-based perspective to better understand the region's convective activity. The work additionally acts as a starting point for future and broader meteorological studies in other potential areas susceptible to adverse weather events. In this sense, for instance, the results obtained in this paper could be applied to other regions with similar features of heavy rainfalls that produce flash floods, as it has been commented before. This is the case, for example, of Liguria (Italy), where convective activity plays a major role (see, Fiori et al., 2014; Braud et al., 2014; Gaume et al., 2016). Besides, this chapter pretends to serve as an extended validation for the identification and tracking algorithm developed in Chapter 6, in an area with different convective regime.

8.1 Characteristics of the regions of interest

Figure 8.2 shows the regions of study, hereafter denoted Regions of Interest (ROIs). The analysis is focused on the southern coast of Catalonia, referred to as ROI1, and a more focused smaller region centered over the Salou municipality (ROI2) for more detailed study (Figure 8.1). ROI1 is typically affected by surface freshwater floods and flash floods (Llasat et al., 2014), which is a consequence of a high frequency of local and short convective events producing heavy rainfall (Llasat et al., 2007) as well as height variations of the local mountain ranges (from 0 to 600 m in less than 10 km or from 0 to 1200 m in less than 30 km) acting as a triggering mechanism for convection (Figure 8.2a). The steep orography also influences in the hydrologic part, because of the short time response of the basins. Specifically, 29 flood events have occurred between 1981 and 2015 in Salou, impacting the town itself and several campings and vacation resorts surrounding the region that are crossed by streams flowing into the Mediterranean Sea (Figure 8.2b). Although autumn floods are usually associated with synoptic situations characterized by cyclonic structures and southeast advection, local flash floods that occurred primarily in summer and early autumn are not reflected at synoptic scale, being mainly associated with mesoscale factors (Gilabert and Llasat, 2018).

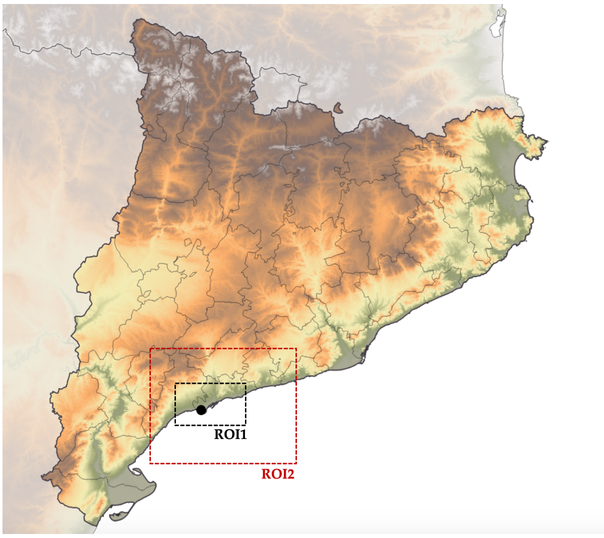

Figure 8.1: Catalonia (NE of the Iberian Peninsula) and the two regions studied (ROI1 and ROI2)

Interest in Salou is motivated by its status as one of the most important touristic towns in Catalonia because of its beaches. Although the municipality only has 26,775 inhabitants (2018) in an area of 15.13 km^2 (density of population of (1,769.7 inhab./km^2), overnight visits approach nearly 8 million annually (i.e. 7,994,205 in 2017). Shown in Figure 8.2a, the major urbanistic and touristic settlements are surrounding the stream "Torrent de Barenys" and thus lie within a potential high-risk flood area. The different return periods shown in Figure 8.2b (10, 100 and 500 years) correspond to a precipitation amount of of 110.4 mm, 187.4 mm and 249.1 mm and a discharge (volumetric flow rate from streams to the sea) of 57.3 $\mathrm{m}^3\,\mathrm{s}^{-1}$, 178.1 $\mathrm{m}^3\,\mathrm{s}^{-1}$ and 307 $\mathrm{m}^3\,\mathrm{s}^{-1}$, respectively. It is observed that an important part of Salou is constructed over a flood-prone area which considers not only flooding as a result of *in situ* rain but also upstream rain, affecting the headwaters of the "Torrent de Barenys". The cases presented in the final part of this paper show these different possibilities, highlighting the flood of the stream when it barely rains over Salou. This is one of the most dangerous situations since the population is off guard and with a low temporary response.

More revealing information is found through a lightning analysis, which, ac-

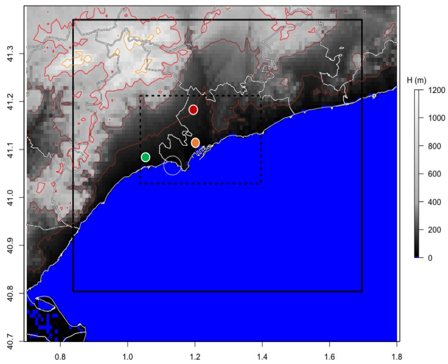

(a)

(b)

Figure 8.2: (a) Topography of ROI1 (solid black line rectangle) and ROI2 (dotted black line rectangle). The town of Salou is marked with a white circle. The light brown, brown, red and orange lines indicate the 100, 300, 600 and 1000 m contours, respectively. The color circles represent the three Automatic Weather Stations (AWS) of the Meteorological Service of Catalonia (SMC); U6 in green, XE in orange and VQ in Red. (b) Flood hazard map of the Salou stream “Torrent de Barenys” for different return periods; T=10 years (pink contour), and T=100 years (orange contour), T= 500 years (blue area). Red stars represent camping and vacation resorts (source: ACA, 2019)

cording to the database from 2000 to 2018 of the Spanish Agency of Meteorology, AEMET, shows that the coast of ROI1 (Salou and surroundings) is the most affected by lightning compared to the rest of the Catalan coast (Figure 8.3). This supports the understanding that frequent events affecting the area are also of convective behavior, which implies additional risks to the area, such as possible severe weather (e.g. strong winds, hail, and even tornadoes). Frequent CG lightning also impacts electrical networks and increases the potential for forest fires, but also poses a serious risk to human safety. The coupling of these convective meteorological phenomena and the increasing population and vacation resort settlements during the summer and autumn seasons makes this area extremely vulnerable to adverse and severe weather, and thus motivates the study of these events along the western Mediterranean.

8.2 Methodology

The core of this study is performed by analyzing results after applying the object-oriented convective cell identification and tracking algorithm presented in Chapter 6 (del Moral et al., 2018b) to the 6-minute composite volumetric reflectivity data set for the period 2014-2018. However, to optimize computational time, a preliminary

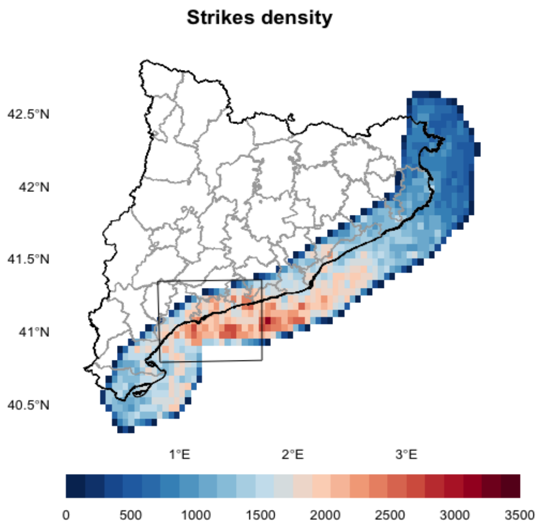

Figure 8.3: Cloud-to-ground (CG) strike density over the Catalan coast from the period 2000-2018. The main region of study (ROI1) is marked with a black rectangle. The map has been constructed with the AEMET CG lightning database data (the only one that the agency provides.)

filter based on the daily and hourly accumulated rainfall fields has been applied to reduce the initially more than 438,000 volumetric fields (explained in detail in Subsection 8.2.1).

8.2.1 Daily and hourly preliminary filter

This procedure consists of the application of the daily filter shown in Chapter 4 and del Moral et al. (2017) in order of identifying "potentially convective" days over a total of 1826 daily maps covering ROI1 for the entire period. We identify a potentially convective day having, at least, one structure with maximum accumulated precipitation of over 15 mm 24 h, where a structure is defined by a precipitating area of, at least, 6 km^2. This reduces the daily starting dataset to 250 files, and consequently 6,000 hourly files. Then, the hourly filter is used within the same area (ROI1), with a threshold for identifying the precipitation structures of 1 mm/1 h and with no area restriction. This lessens the dataset to 1,290 final files. In terms of 6-min volumetric fields, it results in 12,900 10-level CAPPI volumes for processing with the identification and tracking algorithm.

8.2.2 Identification and tracking of convective cells

The identification and tracking of the convective cells is performed by applying the algorithm described in Chapter 6 and del Moral et al. (2018b). As explained previously, this new object-oriented 3D identification and centroid-tracking algorithm is a 4-step version updated for severe weather surveillance purposes to identify severe storms that present anomalous movements (split and/or merge) that tend to affect the Catalan area during the convective season. After identifying the convective cell, these are tracked throughout the entire life cycle to obtain time- and direction-dependent features. These meteorological structures are called henceforward "storms", which are defined as the connection of different convective cells through radar frames (and thus through time). We thus describe direction- and time-dependent features over ROI1 by accounting for the velocity and duration. Importantly, this framework allows the identification of convective initiation (CI). Finally, we compare the convective features of the ROIs with features identified in notable flash-flood events that have impacted Salou, which allows us to establish key characteristics of these flood-producing storms.

8.3 Results

This section contains three subsections: (1) the analysis of the convective cells, which includes a study of the outlier values of some features, (2) the entire storm life cycle climatology, and (3) the comparison with important flash-flood events in the area. Subsection 8.3.1 includes a study of the outlier values of some features, to determine if they correspond to real cells or not. Although those values might not skew a lot the distribution, it is necessary to know if those outlier values correspond to real storms that might pose a much higher safety risk.

8.3.1 Convective cells

Seasonal distribution

The spatial distribution of convective cells, by season, within ROI1 for the period 2014-2018 is shown in Figure 8.4, where the distribution is the number of cell centroids inside a pixel of a $4\,\mathrm{km}^2$ area. The number of convective cells varies strongly depending on the season of the year. Autumn (October to December) presents the highest number of cells (Figure 8.4d), with areas affected by more than a total of 4,000 cells, which coincides with the convective season in the coastal area of Catalonia (Aran et al., 2015). Spring and summer (April to June and July to September, respectively) record maximum values above 1000 cells (Figure 8.4b and Figure 8.4c). Note that the color bars in each sub-plot of Figure 8.4 are scaled according to the maximum value and thus differ from one sub-plot to another. Winter (January to March) is the season with the smallest amount of convective activity, with a maximum value of only 150 cells during the studied period and large areas without a single cell.

Having in mind the topography presented as contour lines, Figure 8.2b shows clear differences in the pattern distribution regarding the first and second half of the year. During spring (Figure 8.4b), the convective activity is mostly concentrated inland, mainly over the mountainous area (top left corner of Figure 8.4b). This indicates that the sea surface is colder compared to land temperature. In this context, the orography plays a key factor in the convective process, likely as a triggering mechanism or an aid in creating convergence lines for organizing thunderstorms. Contrarily, both summer and autumn (Figure 8.4c and Figure 8.4d, respectively) show a greater concentration over the sea. This is due to the high surface temperature of the Mediterranean Sea, which feeds the lower atmosphere with a large amount of moisture and enables the cells to grow and develop more rapidly (Pastor et al., 2015).

Convective cells characterisation

The main features of the cells, including maximum reflectivity (ZMAX), convective cell top height (HTOP, in km) and the highest height of the 40 dBZ echo (HTOP40, in km), are shown in Figure 8.5. First, it can be seen the high variation of cell identification along the year: September and October are the only months on which it has been identified convective cells for all the years. Also, these months present the highest variation in all the characteristics. The median value for the core height is 3 km for all years (Figure 8.5a), except for 2014 during which it is even lower (2 km). In addition, the interquartile range is 2 to 4 km for all years, indicating that the top of the cell is typically located at low levels. This is representative of shallow convection, frequent in the Catalan coast where usually thunderstorms' cell tops don't exceed 6 km (Ballart et al., 2009). This is the opposite of most of the thunderstorms producing severe weather phenomena in other regions of Catalonia, such in the plains, where these present higher tops, even exceeding 10 km (see, for instance, Rigo and Llasat, 2004; Rigo et al., 2010; del Moral et al., 2017).

The median ZMAX for all years is between 40 and 45 dBZ, which represent

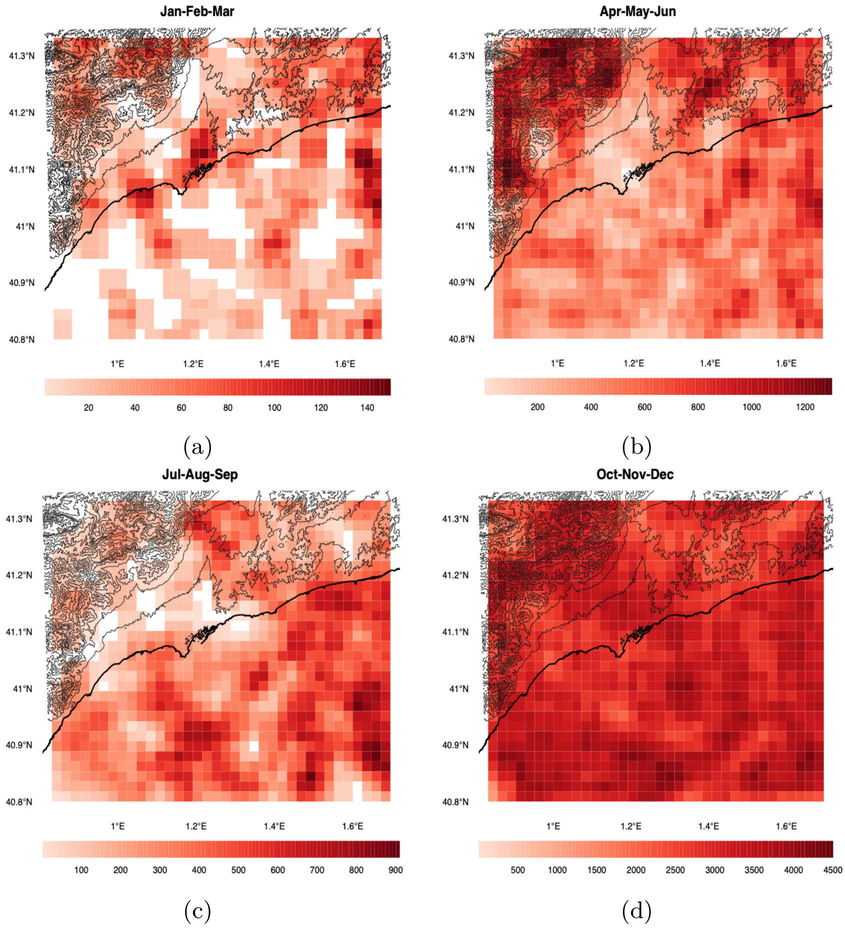

Figure 8.4: Spatial and seasonal distribution (number of cells in a 2x2 km^2 pixel) of convective cells between the period 2014 to 2018 in ROI2; (a) winter (January through March); (b) spring (April through June); (c) summer (July through September) and (d) autumn (October through December). Pixel maps have been smoothed by applying a 3x3 Gaussian filter around every pixel. Each pixel corresponds to an area of 4 km^2, and the contour lines indicate the topography every 100 m.

values likely resulting from high precipitation efficiency (rimed ice particles like hail or graupel generally produce higher reflectivity values of up to 60 dBZ). It is also found that the echo tops of 30 dBZ do not exceed 8 km of altitude (most of the cases under 5 km) and that high reflectivity values (over 40 dBZ) are located at low levels. According to Doswell III et al. (1996), the high precipitation concept is referred to as a high relationship between the output and input water fluxes in a thunderstorm. Therefore, values over 40 dBZ indicate that most of the input water flux is converted into rainfall which, from a spotter point of view, would result in really intense and with large drop size. The yearly distribution of ZMAX shows that during 2017, cells generally produced lower values of reflectivity. The highest ZMAX values occurred during 2018, which was also the year in which Catalonia, and especially the Salou area, recorded extreme precipitation values and several floods during the autumn season. Also, that year was the most convective one o on average, since a high amount of cells, with slightly higher values of ZMAX, HTOP and HTOP40 occurred (Figure 8.5). Table 8.1 shows the remarkably high maximum values of 24-h precipitation for 2018. The three AWS within ROI2 recorded more than 100 mm in 24 h in October, with two records occurring during the same event – the storm on October 14, 2018.

Table 8.1: Maximum values of precipitation in 24h [mm] and mean annual precipitation [mm] for the period of study (2014-2018) for the three Automatic Weather Stations from the XEMA network of the SMC within ROI2

Year	**Station**	**Annual Mean [mm]**	**Annual Max/24h [mm]**	**Date Max/24h [DD/MM]**
	V6	638.5	62.9	16/09
2014	U6	418.9	30.5	30/11
	XE	544.8	46.5	30/03
	V6	549.5	95.9	02/09
2015	U6	382.8	45.9	02/09
	XE	471.5	43.6	29/09
	V6	500.3	57.6	27/11
2016	U6	481.8	97.7	16/12
	XE	425.1	59.4	27/11
	V6	339.9	45.4	24/03
2017	U6	273.1	50.6	18/10
	XE	276.9	39.3	24/03
	V6	848.4	100.2	14/10
2018	U6	682.5	112.6	09/10
	XE	762.8	101.2	14/10

The 40 dBZ echo tops (Figure 8.5c) are generally located at almost the same

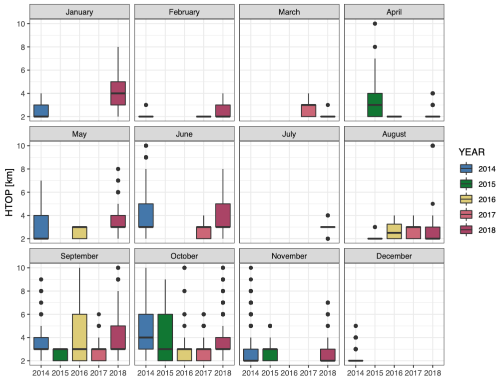

(a)

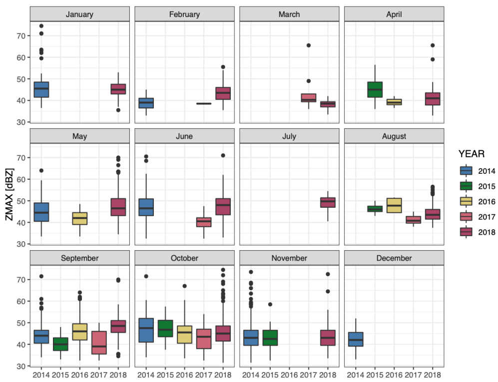

(b)

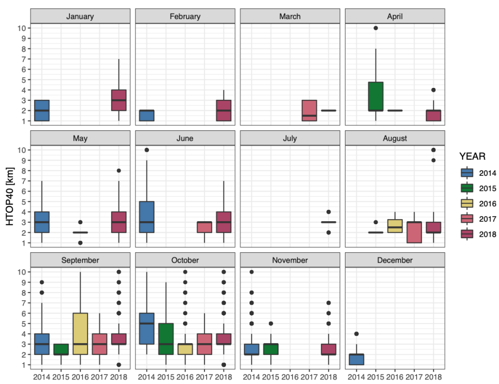

(c)

Figure 8.5: Boxplots of convective cells characteristics separated by year and month; (a) convective cell top height, HTOP [km]; (b) maximum reflectivity, ZMAX [dBZ] and (c) maximum height of 40 dBZ echoes, HTOP40 [km].

height as the cell tops (Figure 8.5a), with the interquartile range generally between 2 and 3 km. Both results demonstrate that the region is usually affected by convective cells with low vertical development (shallow convection) and a high precipitation efficiency, where the intense cores occupy low- and mid-levels of the troposphere. According to the single-cell conceptual model (Chisholm, 1972; Wilk et al., 1979), this behavior agrees with cells in later mature stages. During that period (late mature) the updraft starts to dissipate, and the core is displaced to low levels. this behavior agrees with cells in later mature stages. During that period (late mature) the updraft starts to dissipate, and the core is displaced to low levels. This stage starts where a dominant downdraft forms and the precipitation reaches the surface shortly after. It is important to note that this conceptual model is also used to describe other types of convective organization (multicell or supercell; Doswell, 2001; Kumjian and Ryzhkov, 2008).

Outliers analysis: extreme values

The distributions in Figure 8.5 show that some outlier cells have a ZMAX $\geq$ 59 dBZ and an HTOP $\geq$ 8 km. Using these values as a threshold for identification, a total of 19 outlier cells were found that formed on 6 different days, as shown in Figure 8.6. These outliers coincide with large convective cells, mostly concentrated along the coast or offshore, that have extremely high reflectivity values and deep vertical development (Figure 8.5). These features suggest the occurrence of deep convection in some concrete events, in which the updrafts tend to reach above the freezing level where the coexistence of liquid and ice phase particles results in higher reflectivity. Another outlier pattern was found when analyzing the reflectivity values in Figure 8.5; these include 19 cells with very high reflectivity values but also relatively low echo top heights of 2 km, which are part of 11 different days. A representative sample of those outlier cells is shown in Figure 8.7. These outlier values with ZMAX $\geq$ 59 dBZ, most reaching values $\geq$ 60 dBZ, do not represent real meteorological pixels and therefore are not part of a cell core. The reflectivity gradient is much stronger than the case of the outliers in Figure 8.6; those extremely high values of reflectivity are surrounded by neighbor values which in all the cases differ by, at the very least, 20 dBZ. Furthermore, it is important to note that the position of the maximum values is located over the same area (framed in black in Figure 8.7). Comparing Figure 8.7 with Figure 8.1, this area is shown to be within the mountainous region. This suggests possible anomalous propagation of radar echoes or electromagnetic interferences with, for instance, electric towers

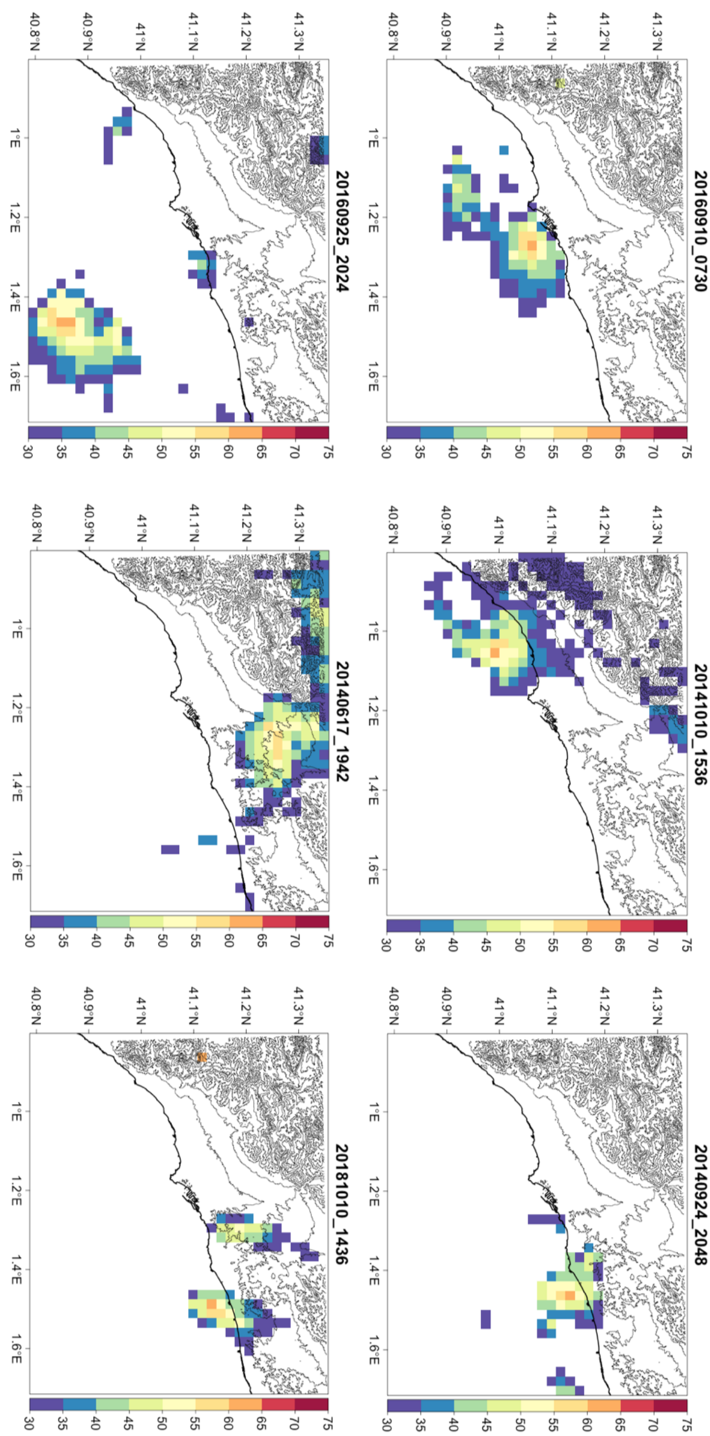

Figure 8.6: Maximum reflectivity (ZMAX) for the six different convective cells with outlier values (high ZMAX, HTOP, and HTOP40). The color bar represents reflectivity in dBZ.

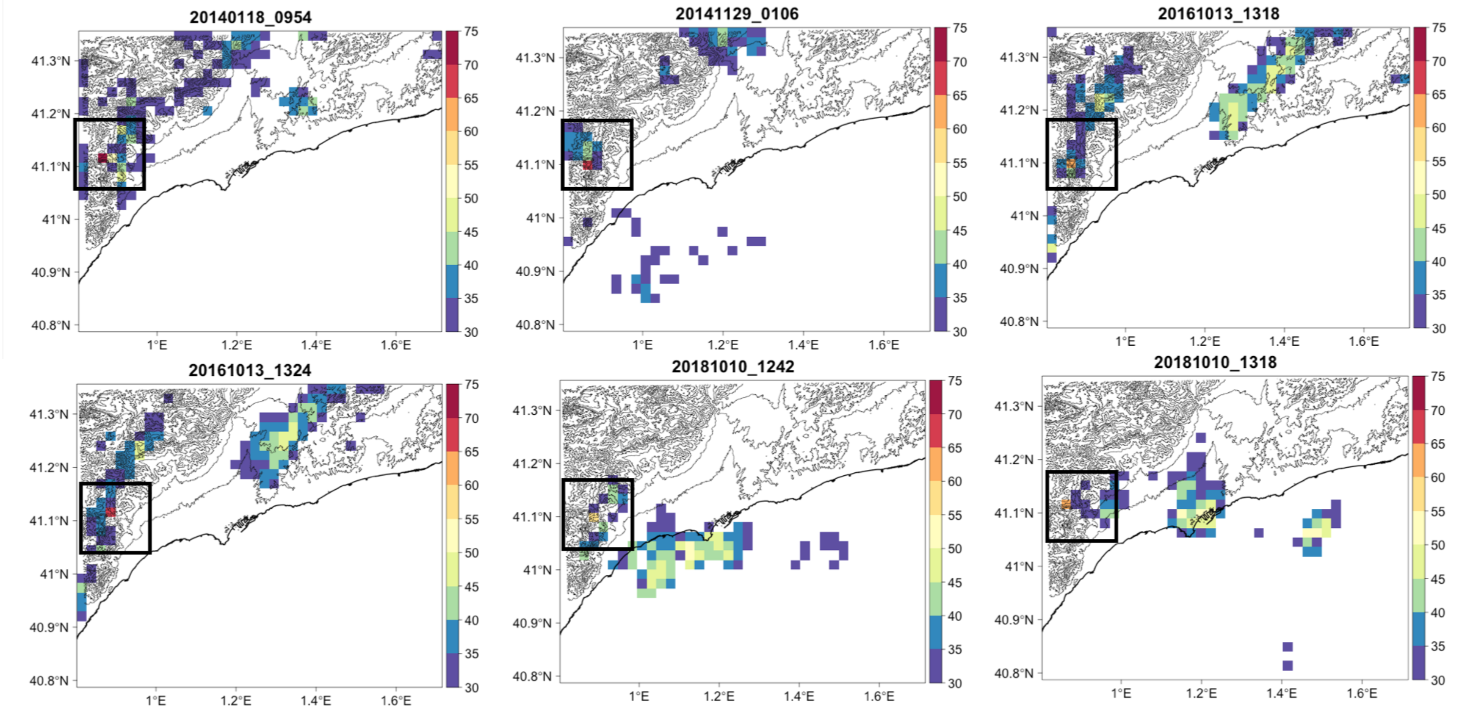

Figure 8.7: Maximum reflectivity of 6 radar frames with the second group of outliers (high ZMAX and low HTOP and HTOP40 values). Pixels with the highest reflectivity value are framed with a black box. Color bar represents reflectivity [dBZ]

or wind farms. For that reason, these outlier values have been considered to be unreal convective cells, and therefore are discarded as a real representation of the convective activity in the area.

8.3.2 Storm life cycle

Storm initiation

Understanding the nature of the storms that affect ROI1 requires determining the location of initiation. Figure 8.8 thus shows the spatial distribution, separated by season, of the storm initiation (henceforward, SI) expressed in the number of cells in a pixel of $4\,\mathrm{km}^2$. This is the location of the first identified 3D cell that encompasses the entire storm after tracking. The spatial distribution, as well as the SI density, follow a similar pattern that the total number of cells by pixel shown in Figure 8.4, although in the SI case the region analyzed is extended to surrounding areas (ROI1 instead of ROI2, in order to identify the role of topography in the initiation). Note that the maximum SI concentration is located inland during winter and especially during spring (Figure 8.8a and Figure 8.8b, respectively), which would coincide with the triggering effect from orography. On the other hand, for the warm seasons when the sea surface temperature is high, SI moves offshore, where convergence lines can be seen in the area (Figure 8.8c and Figure 8.8d). This would coincide with the usual patterns (Pineda et al., 2007; Rigo et al., 2010) during the convective season in the Catalan area, where several easterly flows affect the coast and convergence lines can be formed perpendicular to the coast (east to west).

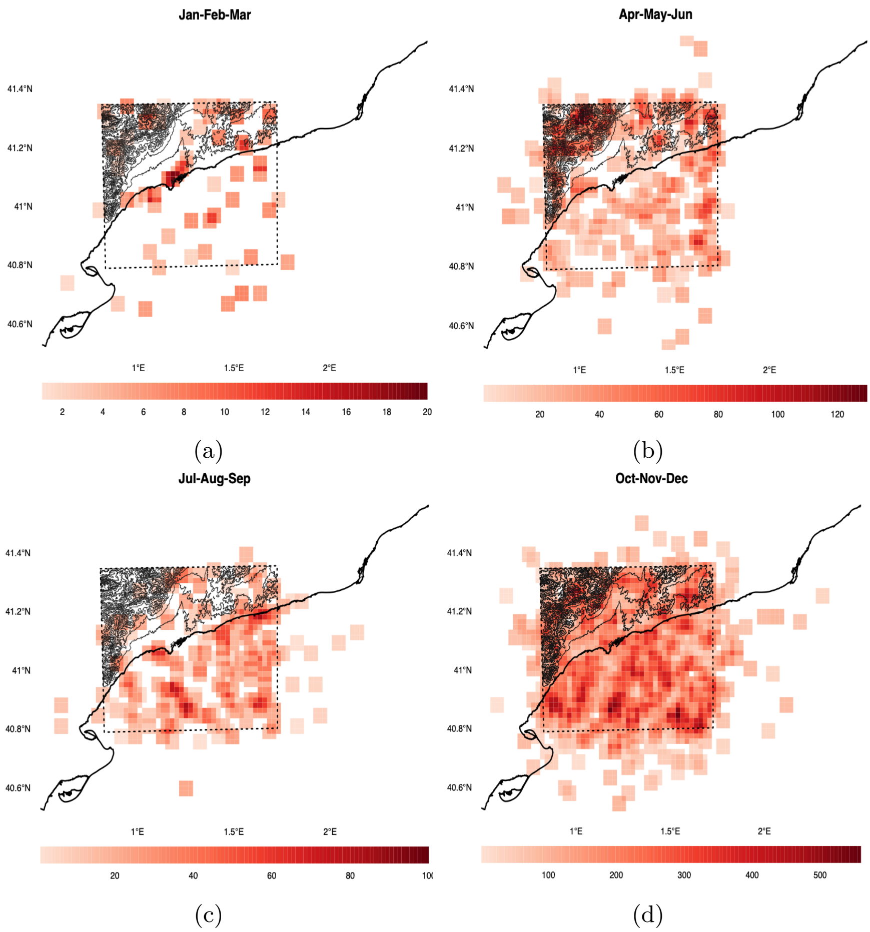

Figure 8.8: Spatial distribution (number of 3D cells) of storm initiation affecting ROI1, separated by season; (a) winter (January through March); (b) spring (April through June); (c) summer (July through September) and (d) Autumn (October through December). The color bar represents the number of 3D convective cells by a pixel of 2x2 km^2, and contour lines indicate the topography (every 100 m). The original pixel has been resized by applying a 3x3 Gaussian filter around it, which is why the area represented is bigger than the ROI1 area (dotted line).

Storm characteristics

The storm characteristics in terms of lifetime duration, direction and mean speed is shown in Figure 8.9. The wind rose shows the proportion of time (in percent, %) that the wind is from a given angle and the wind speed range. In other words, it indicates where the storm comes from (e.g., a west direction in the wind rose implies that the storm is moving towards the east). The median value of the entire dataset for the duration of the storms is 24 min, with the longest values found in the storms of 2016 in April, where the third quartile is up to 50 min (Figure 8.9a). Then, most of the storms are singular, short-lived cells but very effective in terms of precipitation or, on the other hand, they are embedded in multicell systems. This latter case is usually associated with the convective train effect in the area (several cells are constantly growing in the rear flank and are being fed by the mature cells in the forward flank, Doswell III et al., 1996). Although no satellite or broader radar image is provided in the present study, these characteristics match with other previous studies of flash flood and mesoscale systems in the Catalan coast, where the train effect is clearly depicted (see, for instance, Rigo and Llasat, 2007; del Moral et al., 2017; Rigo et al., 2019).

It is important to remark the high monthly variability of speed and direction of the storms. Although most of the cells come from SSE or SW directions during the convective season (Figure 8.9b), implying that they travel from the sea to inland or parallel to the coastline, it is shown how another main direction is taken during June and August; NNE. This implies that during those months, cells could be more forced by northeastern flow which could correspond northern relatively cold advection crossing Catalonia. Besides, a large proportion of the total set ($>$ 10 %) travels from SSW towards NNE, which is exactly the coastline orientation. With respect to the velocities, most of them range from 2.5 to $17\,\mathrm{m\,s^{-1}}$, with the biggest segments, in all paddles, between 7.5 and $12\,\mathrm{m\,s^{-1}}$, especially in October and November. This indicates that most of the storms move with the same average velocity than the flow at low levels (usually taken at 850 hPa) which would lead the storm core motion (in these cases almost surface, see for instance, del Moral et al., 2018b). This agrees with some previous case studies analyzed in the southern Catalan coast during autumn, that is, linearly organized mesoscale systems with convective cells that regenerate continuously, traveling mostly parallel to the coast. These systems can cross the entire Catalan region in less than 3 h (Rigo et al., 2019), and are usually the result of Mediterranean lows. However, in other cases, they can remain stationary in located areas (Rigo and Llasat, 2005), as it is seen

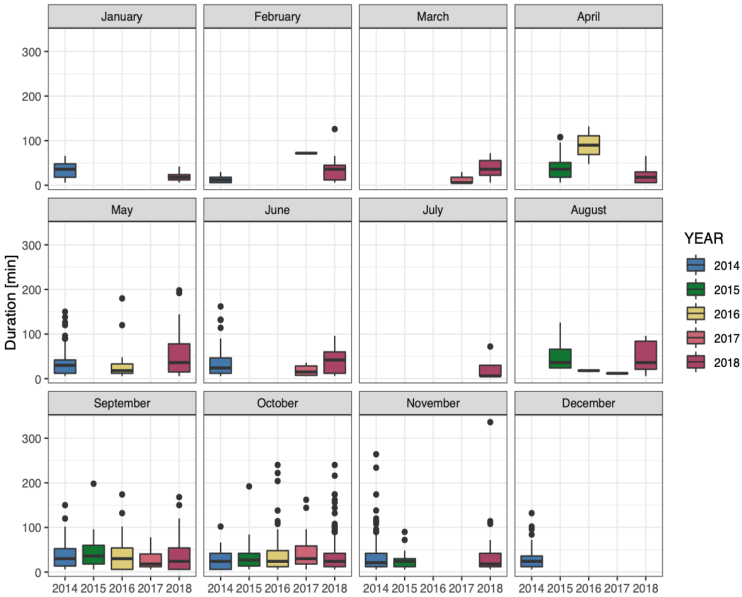

(a)

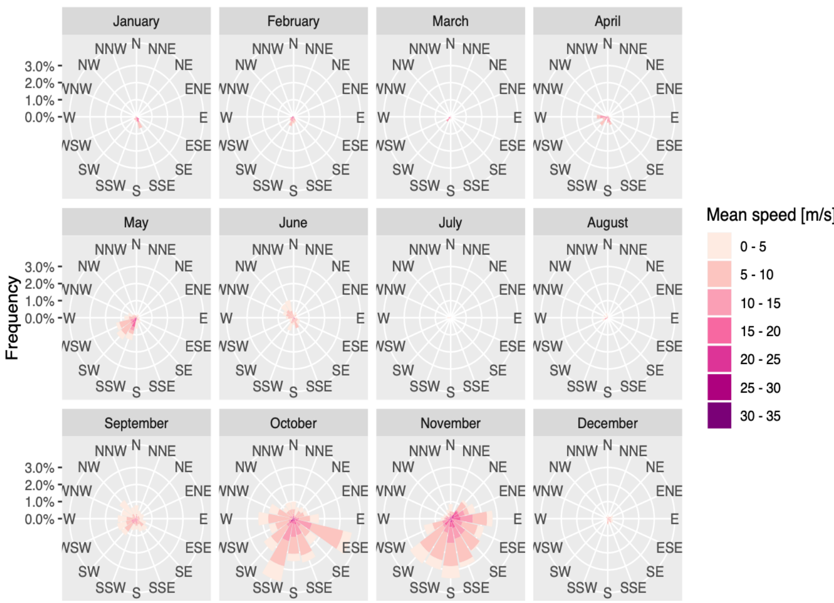

(b)

Figure 8.9: Storm life cycle characteristics; (a) lifetime duration [min] by months and year; (b) wind rose diagram for the total period 2014 to 2018, showing the frequency of storm speed [$\mathrm{m\,s^{-1}}$], and direction by month.

in other months that present low velocities ($< 2.4\,\mathrm{m\,s^{-1}}$).

8.3.3 Convective characteristics in three flash floods events

Event overview

This section focuses on the analysis of three flash flood events that affected the town of Salou and its surrounding area during the period from 2014 to 2018. The aim is the presentation of the main hydrologic and meteorological features, which will be compared with the thunderstorm's properties in the following section. The three cases compared and evaluated are 29 November 2014, 29 September 2015 and 10 October 2018. The first event affected the entire Catalan coast over three days, in which during the first day the system moved over the region of interest and recorded the maximum precipitation among all the cases: 336.1 mm in 24 h in Els Ports, which is approximately 100 km south of Salou. The entire system produced several flash floods in the Catalan region, especially along the coastline. The effects of the episode were also aggravated by the strong sea surf. In total, 179 municipalities were severely impacted, one death was recorded and the "Consorcio de Compensación de Seguros" (CCS, 2018), which is the National Insurance Company, paid more than 12.4 million € (adjusted to 2015).

Although the flash flood event of 29 September 2015 only reached 145.1 mm in 24 h in Sant Pere Pescador, North of Catalonia, it was coincident with a strong storm surge and the CCS paid more than 12.1 million €. In this case, the AWS VQ, in Constantí, approximately 20 km north of the city center of Salou, recorded a maximum of precipitation of 83 mm. The Torrent de Barenys in Salou overflooded and the sea surf destroyed part of the town's seafront.

Finally, during the 10 October 2018 event, additional surrounding Autonomous Communities were impacted, and the flash floods and storm surge resulted in three deaths. In this case, the maximum precipitation recorded for the region of study was 98.4 in the AWS XE, at the Education Center in Tarragona, approximately 10 km north of the city center of Salou. The major affectations involved several other cities, especially Barcelona, were main roads and metro stations were flooded due to localized and intense storms. In this case, the CCS had to pay more than 2.1 million € just for the claims from the 10 October 2018 case.

The daily estimation of precipitation for ROI1, using a statistical combination of the radar field and AWS data of the SMC (del Moral et al., 2017; Rigo et al., 2019), is shown in Figure 8.10. The rainfall field presents large differences between episodes, both in the distribution and in the maximum values over Salou and the surrounding area. In the case of 29 November 2014, the rainfall over the city was relatively scarce, with the maximum values concentrated in the mountainous areas of the Pre-Littoral range (maximum height close to 1,200 m). In the 29 September 2015 case, the maximum values were mainly concentrated along the oriental slope of the mountain (heights lower than 500 m) closer to Salou, but again the precipitation recorded over the city was low. Finally, in the 10 October 2018 case, the precipitation was situated over the town and surrounding areas. In the two first cases, flash floods started in the upper part of the streams, causing damage outside and inside the cities, while the third case was a typical example of surface water floods by precipitation *in situ*.

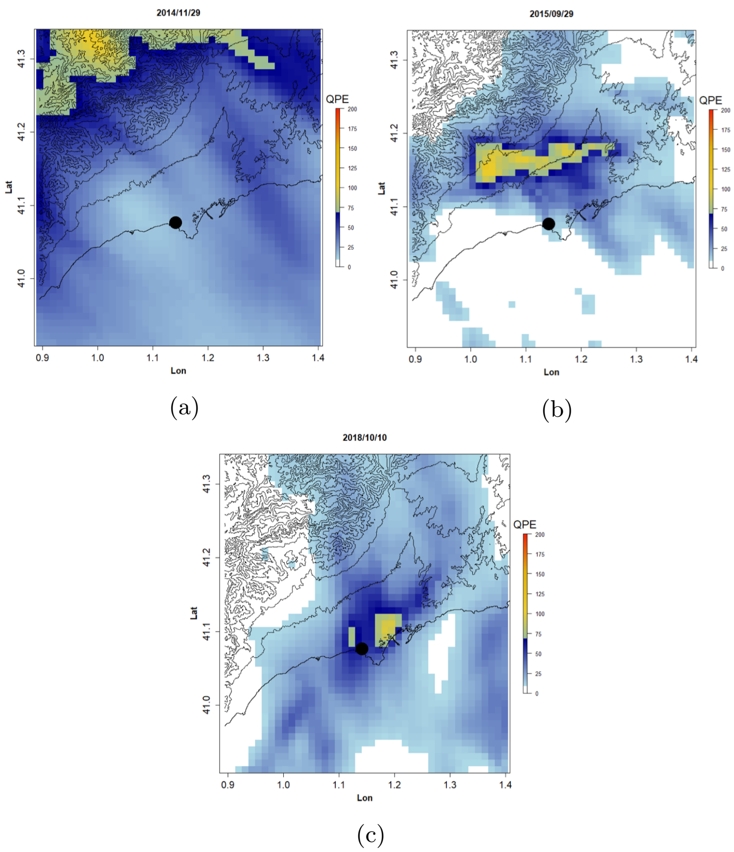

Figure 8.10: Estimated daily rainfall field [mm/24 h], resulting from a combination of radar and rain gauges from the SMC; (a) 29 November 2014; (b) 29 September 2015; and (c) 10 October 2018. The black dot shows the location of Salou.

Cells characteristics

The convective cells characteristics for the three cases are shown in Figure 8.11. The 2018 event shows higher values for all three characteristics (ZMAX, HTOP, and HTOP40) compared to the climatology (Figure 8.5). The HTOP values span between 3 and 6 km (Figure 8.11a), with an outlier of 7 km, the HTOP40 values range from 4 to 5 km (Figure 8.11b), and the ZMAX interquartile and median values are between 48 and 58 dBZ (Figure 8.11c). These three features lie outside of the median values found for that year, (Figure 8.5c) even if we consider that 2018 is an outlier among the period. This indicates that the cells affecting the area had very high rainfall intensity due to the deep vertical developments. For the two other cases (2014 and 2015), the characteristics of the cells lie within the climatic patterns found previously from the entire period (red and orange box in Figure 8.5). Specifically, the vertical development (HTOP and HTOP40) range from 3 to 4 km (Figure 8.11a and Figure 8.11b) and therefore suggests shallow development. However, Figure 8.11c also shows that 2014 could be also considered slightly deviated from the median patterns in terms of cell intensity (ZMAX). In this case, the ZMAX values are higher than 45 dBZ, with a median value almost reaching 48 dBZ, indicating that the cells had shallow vertical developments but were very efficient in precipitation and with high intense rainfall (high amount of water in a short period of time).

The spatial distribution of the totality of convective cells in 24 h for the three cases, in terms of the centroid height (in blue and green pixels) and location (in red dots), is shown in Figure 8.12. In this case, we show another feature resulting from the 3D identification to see if the center of mass of the entire volumetric structure coincides with the HTOP40. The centroid is computed by weighting the reflectivity values in every level by its water content (Martín et al., 2007). Convective cells of the same storm are connected with lines and arrows in Figure 8.12, with the latter pointing towards the storm propagation (an arrow connects cell from starting to ending point, indicating the bearing direction). The distribution is coincident with the rainfall estimation in Figure 8.10 and the main vertical developments shown in Figure 8.11, but it also allows an understanding of some of the behaviors in terms of motion and probable topography interaction. In 2014 and 2015, the centroid heights (big pixels in Figure 8.12) were between 1 and 2.5 km (see color bar). This matches with Figure 8.11 and indicates that the precipitation was coming from that height. On the other hand, the cells had centroids over 3 km in 2018, with the HTOP40 and HTOP values even higher. This indicates that the maximum reflectivity occurred in a mixed-phased region with reduced liquid water content (Sui et al., 2007).

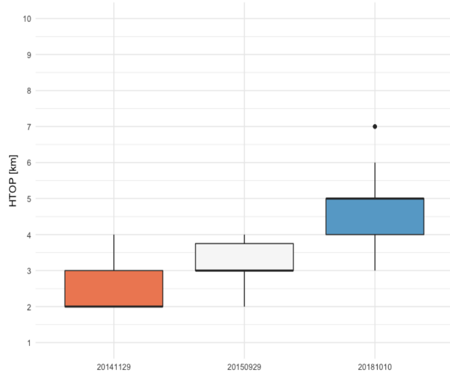

(a)

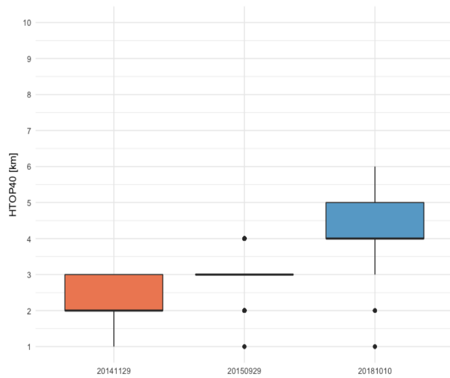

(b)

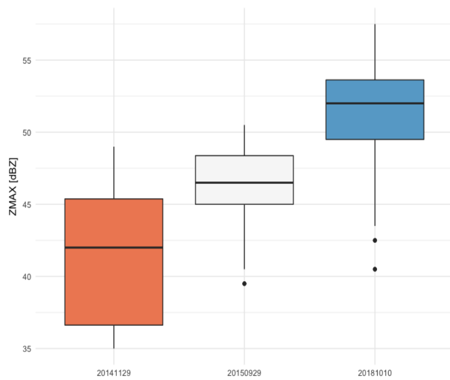

(c)

Figure 8.11: Characteristics of the convective cells for the three flash flood events; (a) HTOP [km], (b) HTOP40 [km] and (c) ZMAX [dBZ].

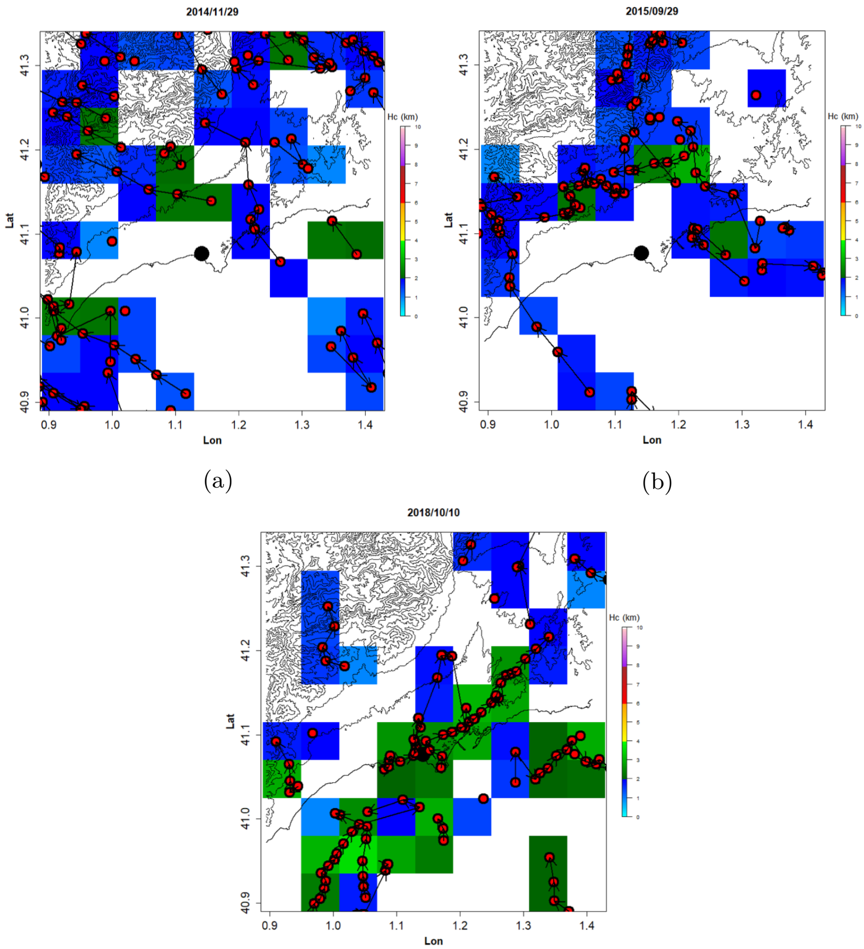

(a) (b)

(c)

Figure 8.12: Spatial distribution of the totality of convective cells in 24 h for the three events; (a) 29 November 2014; (b) 29 September 2015; and (c) 10 October 2018. Large pixels (5x5 km^2) and red dots represent the height and location of the centroid, respectively; lines and arrows represent the storm trajectory, indicating bearing direction. The black dot shows the location of Salou.

We also compare the motion and speed of the storms in these cases. In the 2014 case, it is clear from Figure 8.12a that storms moved from the sea to inland (SSE to NNW), which matches with Figure 8.13a. Figure 8.12b then shows that the 2015 storms moved more erratically, which also can be seen in Figure 8.13b. Although some of the short-lived storms over the sea show a SSE-NNW direction, it is noticeable that the storms inland, especially those interacting with the oriental slope of the mountain, present quasi-stationary propagations (all dots are close in the same area and with weak velocities between 0 and $2.5\,\mathrm{m\,s^{-1}}$ from NNE to SSW in Figure 8.13b).

Finally, Figure 8.12c and Figure 8.13c show that most of the storms during the 2018 case were parallel to the coastline and had higher, although expected, speeds (5 to $10\,\mathrm{m\,s^{-1}}$) with SSW-NNE propagation. Also, the duration of the life cycle of the storms was slightly longer compared to the climatology from Figure 8.9a (not shown), with an interquartile value ranging from 30 to 90 min, which is higher than the climatic value where the interquartile ranges from 10 to 50 min (Figure 8.9a). This can be associated with a higher organization of the convection, with respect to the rest.

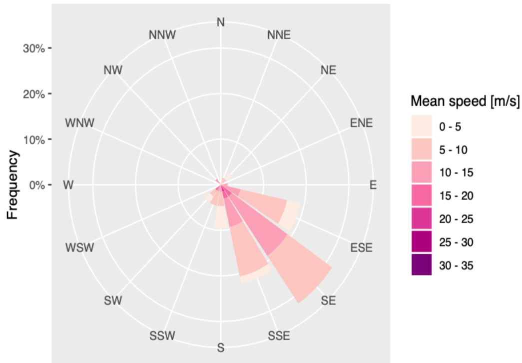

(a)

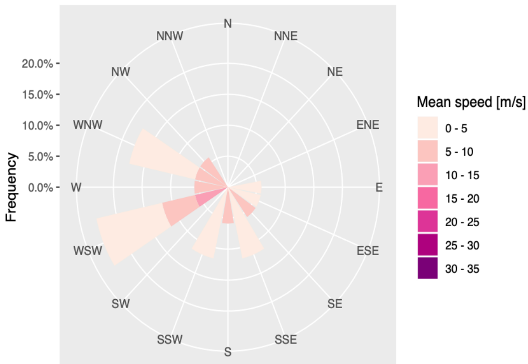

(b)

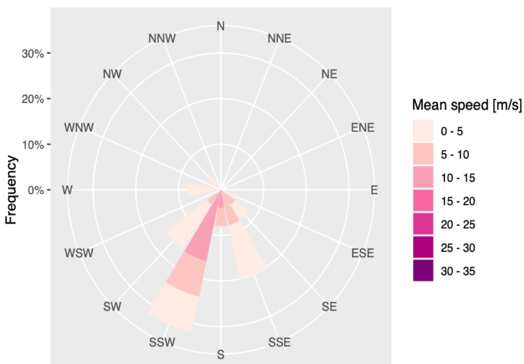

(c)

Figure 8.13: Wind rose diagram for the cases of study, showing the frequency of storm speed [$\mathrm{m\,s^{-1}}$], and direction; (a) case of 2014; (b) case of 2015; (c) case of 2018.

8.4 Discussion and conclusions

The coastal town of Salou in the northwestern Mediterranean region has been used as a test area for analyzing three flash floods. It meets all the conditions of a very densely populated area, surrounded by complex topography and a short response hydrologic basin, which is affected by different types of rainfall events. The analysis has been made using the algorithm for identifying, characterizing and tracking convective cells with volumetric radar data presented in Chapter 6. The technique has been applied to the entire period 2014-2018, obtaining the main convective features of the storms, resulting in a climatic and statistical analysis of the entire dataset. Finally, three main events have been selected within the period studied. This has been done in order to determine the properties (intensity, duration, direction, and triggering factors) of the convection involved in those events, and to discern whether they are the result of rare storms or a common pattern in the area to be aware of.

The results found in the present work can be extrapolated to other Mediterranean areas with similar characteristics. The analysis of the convective cells and subsequent storms affecting the area shows the highest activity between September and November, with moderated reflectivity values ($\approx$ 40 dBZ) and low vertical developments (median of 4 km). Also, these are mainly initiated over the sea or the coastline, traveling or either to inland or parallel to the coastline. This likely corresponds to a convective train effect in multicell or mesoscale systems; new developing cells are being fed by the stationary cold pool of the mature and dissipating ones (preceding). This, along with the configuration of the mean wind and cells' motion inside the system, makes the region to be constantly affected by convective intense precipitation. This is a completely different regime, for instance, like the one affecting the plains or mountain areas in Catalonia, where isolated deep convection produces mostly severe weather (hail or strong wind). Furthermore, the sea is demonstrated to play a major role in the efficiency of the precipitation. The configuration demonstrates the particularity of this coastal area, with shallower convection and a different general flow compared to other areas of Catalonia (Rigo et al., 2010; Rigo and Llasat, 2016; del Moral et al., 2018b).

In general, and for the analyzed three flash flood events, cells show the main pattern observed for the total sample of covective events studied in the ROI; shallow and efficient convection due to the proximity to the sea, playing an important role in the total accumulated values. However, the topography also favors three main key aspects that can be seen from the analysis of the 2018 case, the one that differs from the general pattern. First, it allows the triggering of the convection in those cases where the instability is not high; second, it helps in the formation of an instability line over which the thunderstorms grow, and third, it becomes a capping feature for the cells that get to pass the coastline. This last factor points out that not just a better weather warning system is needed for the area, but also a good adaptation infrastructure plan. Even if the area is not affected by continuous efficient rainfall, flash floods may happen if storms are blocked upstream, producing a rapid increase in the flow in the small streams flooding the settlements (catchments results saturated by a large amount of water).

The results match with other studies done previously in other parts of the world. Shallow and efficient convection has been broadly analyzed in many regions, prevailing in the Tropic and Sub-Tropic areas (see, for instance, Short and Nakamura, 2000; Schumacher and Houze Jr, 2003; Pereira and Rutledge, 2006). The shallow convective cells in these regions are characterized by echo tops usually near 2 km, notably lower than the observed in our region, which could be explained by the presence of a freezing level higher than 3 km (clearly over the one found in the Catalan area). Besides, another important point is the notable contribution of this type of precipitation (shallow but efficient) in the total amount of rainfall; between 10 % and 30 %, depending on the region. Having in mind that some of the cases that produce the maximum accumulation values in our area of study are produced by this type of precipitation, it could be possible that, in some coastal areas of the Mediterranean, these percentages are even larger. It is also important to highlight that the results here presented are similar to those observed in the analysis of the rainfall regimes in Australia (May and Ballinger, 2007), where a high number of short-lifetime shallow cells are found. They also match with the cells observed in Israel (Eastern Mediterranean) by Peleg and Morin (2012), where it is found a large contribution of the sea in the development of shallow convection,and with Godart et al. (2011) that observed the importance of the topography in the south of France in the evolution of shallow convection, which also represents the highest contribution in the total rainfall amount for that area.

The work here presented demonstrates the need for an early warning system in conjunction with adaptation plans. The results so far show that from the meteorological aspects, the system should consider fast recognition of convective cells, accounting for the intensity, that can be translated to precipitable water, but also the motion coupled with the topography. It should be able to set different risk levels depending on two main areas; upstream and downstream of the catchment, since they need a differenced precipitation threshold. Furthermore, the system should be able to release weather warnings if the cells are stationary in the same area for a long time. In this sense, the new 3D identification and tracking tool developed in this thesis (del Moral et al., 2018b), and that is now being put into the operative system in the Meteorological Service of Catalonia, would be a base tool for the warning system. Although there's still a need to address the issue found with the non-weather clutter echoes, which may give false alarms if the threshold is set to values too high, the radar-based nowcasting is the good approach to this type of convection and the related phenomena. This also matches with a similar analyses that has been made in Central Europe by Trentmann et al. (2009), which showed that numerical models are only able to reproduce the nature of the environment, but not to identify the position and time of occurrence of the shallow and efficient convective cells nor either the total accumulation that these produce.

9

C-band dual-Doppler retrievals in Catalonia: Improving the knowledge of thunderstorm dynamics

* The present chapter has been adapted from: del Moral, A., T.M. Weckwerth, T. Rigo, M.M. Bell and M.C. Llasat 2020: C-band dual-Doppler retrievals in complex terrain: Improving the knowledge of severe storm dynamics in Catalonia *Remote Sens.* In preparation after invited to be submitted in special issue: Estimating Meteorological Variables by Remote Sensing Data

As explained in Chapter 3, multi-Doppler retrievals is another technique to study thunderstorms, in concrete, when we want to obtain a dynamical point of view. This tool is coveted in the research and operational meteorological fields, since not always the set up of the radars is optimal for its application. This is the reason why most of the dynamical thunderstorm studies are conducted with idealized high-resolution models. The advances in the last years in the use and development of near-real-time multiple-Doppler techniques with operational radar networks, as well as the improvements achieved in complex terrain seen in Section 3.2, has provided the motivation and foundation for the study presented here. The main purpose of this chapter is to demonstrate how the operational radar network from the SMC, the XRAD, is suitable to retrieve dual-Doppler winds by using a free variational Doppler software within The Lidar Radar Open Software Environment (LROSE) project: the Spline Analysis at Mesoscale Utilizing Radar and Aircraft Instrumentation (SAMURAI, LROSE Development Team, 2019). This project is a collaboration between the Atmospheric Science Department at Colorado State University (CSU) and the Earth Observing Laboratory (EOL) at the National Center for Atmospheric Research (NCAR). It is funded by the US National Science Foundation and is an open-source program that aims to unify different tools for Lidar and Radar data processing and analysis. This project was introduced to the author of this thesis during the stay at NCAR as an awardee of the Advanced Study Program grant. We will demonstrate the powerful capability of this tool to retrieve the winds in a complex terrain area. It is the first time at the Iberian Peninsula that dual-Doppler retrievals are used to obtain dynamical features within particular severe storms, that present unexpected propagation patterns, and that have affected the Catalan area. The concept of the Multiple-Doppler retrievals and the SAMURAI software are explained in the following sections.

9.1 Methodology

Seen in Section 3.2, the mean radial velocity from every single radar is related to the rectangular components of the mean velocity of the hydrometeors (u,v,w) through the azimuth, ϕ, and elevation, ϵ, angles (Equation 9.1, where wt is the terminal velocity of the particles). In this sense, by combining the radial velocities in a closed equation system or, in the case of the dual-Doppler technique (with observation from two Doppler radars), applying boundary conditions on the vertical velocity and the terminal velocity of the particles, and by integrating the mass continuity equation (Equation 9.2, where ρ is the air density), we can obtain a unique solution for the three wind components in a given point.

$$V_r = u \sin\phi \cos\epsilon + v \cos\phi \cos\epsilon + (w + w_t) \sin\epsilon \tag{9.1}$$

$$-\frac{\partial \rho w}{\partial z} = \frac{\partial \rho u}{\partial x} + \frac{\partial \rho v}{\partial y} \tag{9.2}$$

This is actually what all the multiple-Doppler systems solve when retrieving the 3D wind within a thunderstorms, either by geometrical solutions applied directly in Cartesian coordinates or by using a variational method. The latter is the case of the system used in this study, and which is explained in the following section.

9.1.1 Dual-Doppler coverage

The accuracy of the multiple-Doppler solution, this is, the retrieval of u, v and especially w, depends on the geometrical configuration of the radars relative to the target thunderstorm. The variance on the horizontal wind field, which is represented by the standard deviation of the u and v components of the wind (σ_u^2 and σ_v^2), impacts directly in the vertical motion. This, along with the variance of the radial velocity from each radar (the spectral width, represented with σ_1^2 and σ_2^2), define the beam-crossing angle between both radars, β (Equation 9.3, see Figure 3.2 in Section 3.2), and consequently, the *dual-Doppler lobes*. These lobes are depicted in black solid lines (half the lobe) in Figure 9.1.

$$\frac{\sigma_u^2 + \sigma_v^2}{\sigma_1^2 + \sigma_2^2} = sin^{-2}\left(\beta\right) \tag{9.3}$$

In this lobes, equal values of the geometric error of the horizontal wind field fall inside circles passing through the radars location, with centers located perpendicular to the bisection of the baseline, b, the distance separating both radars (Rauber and Nesbitt, 2018). In cartesian coordinates, with two radars located at $(\pm\frac{b}{2}, 0)$, the area covered by the dual-lobes is defined by Equation 9.4. Bibliography demonstrates that one of the most suitable dual-lobes configuration is the one with $\beta = 30°$ (Davies-Jones, 1979), considering $\sigma_u^2 = \sigma_v^2 \leq 3\,\mathrm{m\,s^{-1}}$ (Lhermitt and Miller, 1970; Friedrich and Hagen, 2004). This sets the $\sigma_i^2 = 1.5\,\mathrm{m\,s^{-1}}$ for each radar (cosidered equal), which falls in the radar maximum range used in Altube (2016) (0.1 to $3\,\mathrm{m\,s^{-1}}$).

$$A\left(\beta\right) = 2\left(\frac{b}{2}\csc\beta\right)^2\left(\pi - 2\beta + \sin 2\beta\right) \tag{9.4}$$

Furthermore, according to Carbone et al. (1985), in order to resolve storm-related winds and updrafts, the paired radars must be able to resolve horizontal scales below 3-6 km. This compromises not only the beam-crossing angle, β, but also the baseline, b: if it is too big, the data will degrade at the edges of the dual lobes because of the beam spread and elevation. The spatial resolution, s, is here considered proportianal to the range, R, and approximately to the beam height, defined as $s = \frac{R\pi\Delta}{180}$, being Δ half of the beam width and 180 expressed in degrees (Davies-Jones, 1979). Then, the area representing the region where points are at a distance R to the radars, with a spatial resolution, s, for 0° beam height is described in the following equation (Davies-Jones, 1979). These areas are depicted in red solid lines in Figure 9.1.

$$A\left(R\right) = 2R^2 \left\{ cos^{-1}\left(\frac{b}{2R}\right) - \frac{b}{2R}\left[1 - \left(\frac{b}{2R}\right)^2\right]^{1/2} \right\} \tag{9.5}$$

In this sense, in order to retrieve the best wind stimates, it has to exist a compromise between the area that we can cover with the optimum dual-lobe (Equation 9.4) and the area in where we can correctly solve the thunderstorms because of the pixel resolution (Equation 9.5). This constitutes the intersection of both areas, and depends on the radar beam width and the maximum resolution desired (seen as a result in Subsection 9.2.1).

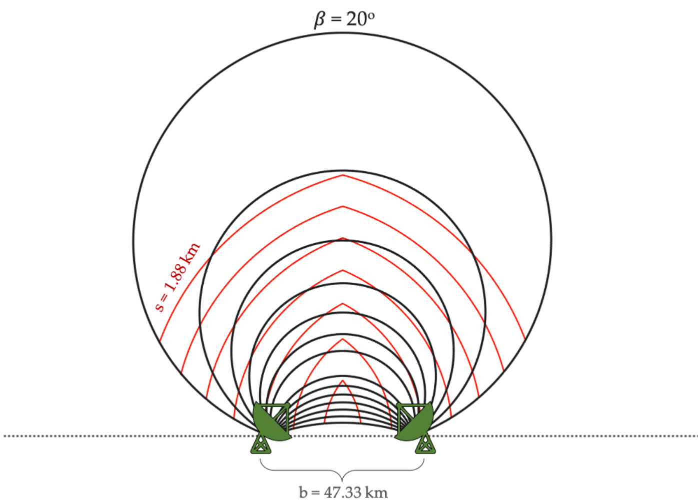

Figure 9.1: Map showing lines of constant β, in black, from 20° to 80° in increments of 10°, and constant s for a beamwidht of 1.2° and a baseline $b = 47.33km$. Constant lines of s are 0.42, 0.63, 0.84, 1.05, 1.26, 1.47, and 1.68 km. *Adapted from (Davies-Jones, 1979)*

9.1.2 SAMURAI: a variational multiple-Doppler method

The SAMURAI software (Bell et al., 2012) is a three-dimensional variational analysis method which can retrieve, apart from the 3D wind in a thunderstorm, the kinematic and thermodynamic features, when ingesting different meteorological data sources. The algorithm, which is based on the work of Ooyama (1987, 2002) and Gao et al. (2004), determines the most probable state of the atmosphere based on observations by minimizing a cost function in incremental form, and using cubic B-spline finite elements. This method can incorporate complex and multiple sources of observations that allow to have a better analysis and background estimates to use in the cost function, which facilitates its minimization (e.g., ground-based and aircraft radar data, atmospheric vertical profiles from soundings, NWP model fields and AWS data). An important feature of SAMURAI, which is relevant to the present study is that, in the minimization process, it is also included an operator that, besides the cubic B-spline transform (Ooyama, 2002), it also includes a Gaussian low-pass filter (Purser et al., 2003). This is crucial when using the XRAD data since it allows an interpolation by filling gaps and avoiding an explicit integration of the mass continuity equation. Also, the spline technique minimizes problems related to missing boundary conditions below terrain and ensures with high accuracy that the mass continuity is conserved all the time.

SAMURAI set-up

As recommended in Bell et al. (2012); Foerster et al. (2014) and Foerster and Bell (2017), it is important to set the filter parameters correctly, since high values may result in an over-smoothed analysis, losing information of fine scale features. The set-up values for the analysis of the study cases are presented in Table 9.1. In this case, and after a sensitivity test, the parameters where set equally for all the cases, since the location of the thunderstorms was similar (in terms of topography or distance to the radars). The Gaussian recursive filter length scale (Δ) was set to 4 and 2 grid points in the horizontal (X and Y), and vertical (Z) directions, respectively, while the spline cutoff length scale, also in grid points, was left to 2 in all directions, as recommended by Bell et al. (2012). The analysis grid spacing was set to 500 m, in order to resolve updrafts smaller than 1 km wide. The radius of influence for gridding the reflectivity field was set to 1 km, and no reflectivity values were masked due to the existence of gaps in some of the raw data.

Since our analysis has been purely based on observed radar data to test the capabilities of the configuration of SAMURAI with the XRAD, the only data used

Table 9.1: SAMURAI main configuration for the study: Radius of influence R_Z [km], Gaussian filter and Spline cutoff Δ, in grid points, and analysis grid increment [km].

R_Z **Influence [km]**	**Gaussian Filter [Δ]**	**Spline Cutoff [Δ]**	**Analysis Grid Increment [km]**
1	4; 4; 2	2; 2; 2	0.5; 0.5; 0.5

has been the reflectivity and radial velocity from the radars selected (no NWP or other data sources). However, to improve the numerical precision of the analysis it is necessary to ingest a vertical profile from a sounding, which helps to subtract off the large vertical gradients in the atmosphere. Sensitivity tests demonstrate that the source of the sounding does not have a real impact in the analysis field, although, to be consistent, we have used the closest (spatially and temporally) vertical profiles to the thunderstorm to analyze. The only sounding station in Catalonia is located in Barcelona, which is very close to the sea, and therefore with a strong moist maritime influence in low levels. For this reason, we used a sounding resulting from the combination of WRF outputs and real observed sounding data. This was made following the criteria applied in Rigo and Pineda (2016), taking the WRF output closest to the thunderstorm location from surface to 850 hPa, and the Barcelona sounding for upper levels. The Zaragoza sounding was not taken into consideration because is $\approx$ 200 km west of all the analyzed cases, even further than the Barelona one. Furthermore, since there was no spectral width field available, all background and error fields were set to a high value, so that the impact on the cost function is minimal and therefore, the only values of significance are the observed ones. Finally, a constant advection field (u,v) was introduced by using the propagation velocity resulting from the new identification and tracking system explained in Chapter 6 (del Moral et al., 2018b). This is done to take into account the propagation velocity and direction of the thunderstorm in the analysis process.

As explained in Chapter 4, despite of the processor filters applied to the XRAD raw data, there are still some corrections that must be done before ingesting it into the dual-Doppler algorithm. To overcome the aliasing issue, that is, when the scatterers move faster than the Nyquist velocity and the estimated velocity is folded back to fit in the Nyquist velocity range (Doviak et al., 1976), the commercial radar processor applies the dual-PRF technique (Holleman and Beekhuis, 2003). This technique, in cases of high azimuthal shear, quite common in severe weather events, results in velocity outliers and errors (May, 2001). For this reason, the radial velocity data is processed with a new algorithm to correct such errors when the dual-PRF technique is applied (Altube et al., 2017; Altube, 2016). Finally, before starting the dual-Doppler analysis, data is cleaned-up using the NCAR SOLO3 software (Oye et al., 1995). This is done to manually correct remaining errors such as ground clutter, second trip echoes or electromagnetic interferences (Doviak and Zrnic, 2014), especially around the area of the target storm being analyzed.

9.2 Results

The results section is divided into three subsections to illustrate the advantages and capabilities of dual-Doppler retrievals in the Catalan area. First, the dual-Doppler coverage and configuration for the XRAD are described. Second, the performance of the SAMURAI technique is described, paying attention to the retrievals of a tornado case on January 7, 2018, over complex terrain and with an over-filtered radial velocity original radar data. Finally, a splitting storm on July 10, 2013, is analyzed to show the possible role of topography associated with an anomalously-propagating system.

9.2.1 XRAD dual-Doppler configuration

Considering that the XRAD radars' beam width is 1.2° and that we cannot change the operational scanning strategies, Table 9.2 summarizes the dual-Doppler coverage, baseline, resolution of the farthest point and blockage for each pair of radars, for the chosen 30° beam-crossing angle. The total area indicates the maximum coverage of the dual lobes taking into account the farthest point and the gate resolution at that point. We've set the maximum horizontal resolution desirable to 3 km (Maximum Resolution in Table 9.2), which allows us to work with two main paired radars: CDV-PBE and CDV-LMI (Figure 9.2). Unfortunately, this leaves the northeastern area uncovered due to the large baseline from the PDA radar to the closest ones (109.01 km to PBE and 136.10 km to PDA, as seen in Table 9.2). The pair PBE-LMI is not chosen due to the overlap of coverage with the chosen pairs with a configuration resulting also in a lower resolution of the data. Finally, the topography blockage for the lowest beam is also low in both chosen pairs (Table 9.2), since most of the blocked area falls within the blind area between the dual lobes, where the wind cannot be resolved correctly due to the collinearity of the wind components of each radar (Figure 9.2). This is less than 2 % of the total area in both cases, and less than 1 % in the CDV-PBE pair.

To test the SAMURAI performance, we've been even more restrict and chosen cases within an area of pixel horizontal ressolution of 2 km (in order to be comparable to some of the products used at the SMC). This allows us to work in optimal area plotted in red dashed-lines area in Figure 9.3. Notice that for the CDV-PBE pair that area is the same as the 30° dual-lobe, since the maximum resolution of the farthest point of the 30° dual-lobe is less than 2 km. This red dashed-lines areas are our dual-Doppler coverages for the present study.

Table 9.2: Dual-Doppler network coverage characteristics for the XRAD, considering a crossing-beam angle of 30°. The topography blocking percentage is only depicted for the two optimal dual-lobe pairs chosen (CDV-PBE and CDV-LMI).

Radar Pair	**Baseline [km]**	**Farthest Point [km]**	**Max. Resolution [km]**	**Total Area** [10^3 km^2]	**Topo. Blockage** [%]
CDV-PBE	47.33	94.66	1.98	13.30	0.61
CDV-LMI	72.60	145.20	3.04	31.04	1.68
PBE-LMI	90.83	181.66	3.80	49.02	-
PBE-PDA	109.01	218.02	4.57	70.78	-
CDV-PDA	136.10	272.20	5.70	110.30	-

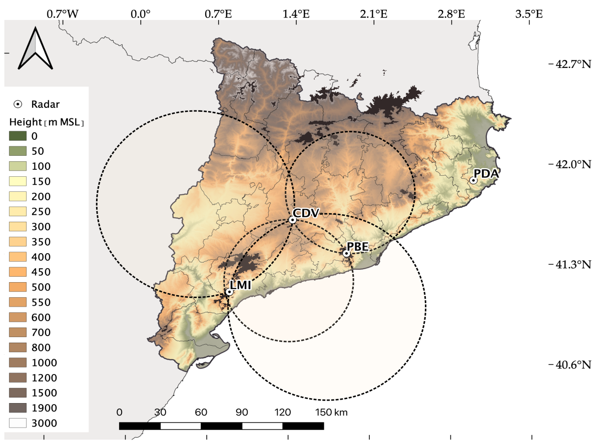

Figure 9.2: Dual-Doppler pairs for the XRAD: CDV-PBE and CDV-LMI. Dotted circles show the dual lobes for a 30° dual-Doppler beam-crossing angle. Topography is shaded in terrain colors and is indicated in meters.

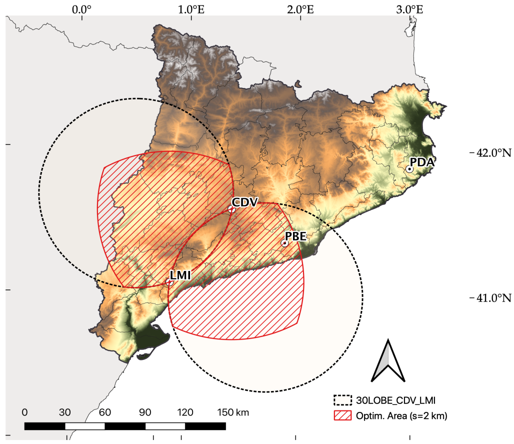

(a)

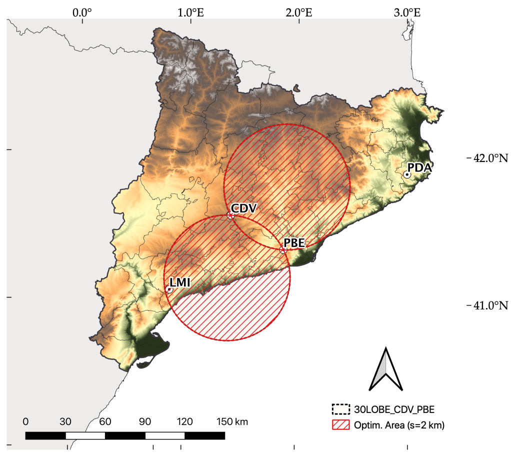

(b)

Figure 9.3: Dual-Doppler coverage for the CDV-PBE and CDV-LMI pairs of radars (in red). The 30° dual-lobe is shown in dotted black circles.

The two pairs selected, allow us to solve with good confidence the regions more affected by severe and adverse weather in Catalonia as we see in Figure 9.4; the western Plains, the central area and the central and southern coast. These maps have been retrieved useing the data from the internal Severe Weather Database from the SMC, explained in Chapter 4. The regions with the highest number of phenomena are the internal western region (the Plains), the central coast and the northeastern counties. and a large and wide region covering almost all of the coast, especially the central and northern counties. These areas have counties with more than 0.015 events per km^2 in the period 2001-2019 (in maroon in Figure 9.4a) and the highest density of Lightning Jumps (LJ) warnings (Figure 9.4b). This is mainly due to hail reports in the western plains and the north-central counties. On the contrary, wind-related phenomena have been observed mainly along the coastline and in the northeastern part, which also coincides with the area with the highest density of population by county (Figure 9.4c).

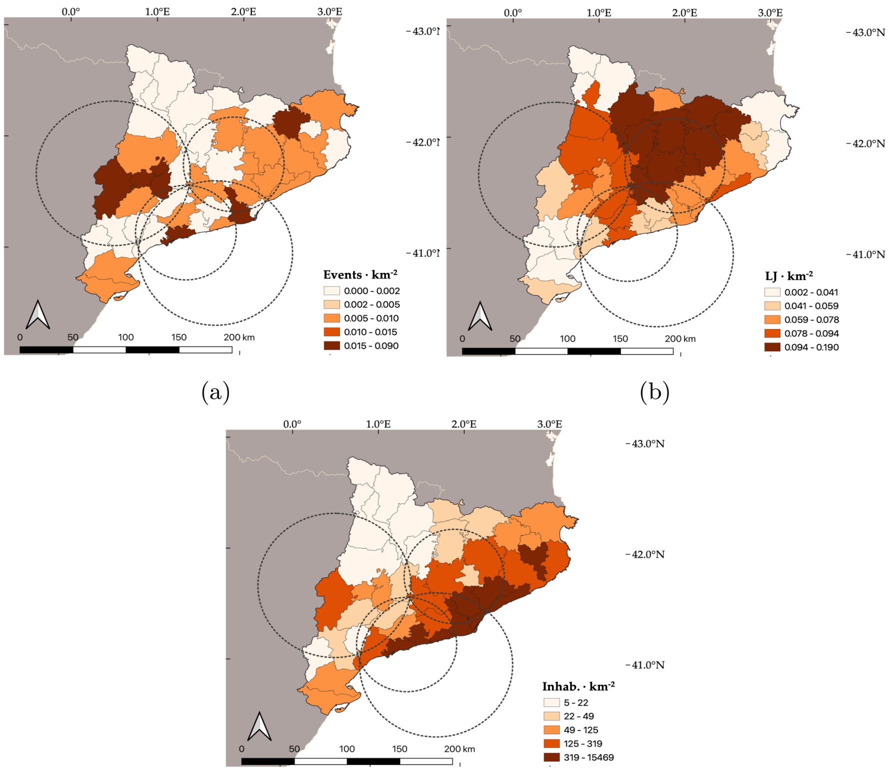

(a) (b)

(c)

Figure 9.4: Geographical distribution of severe convection in Catalonia. (a) Density of severe weather events per county [Events/km^2]; (b) Density of Lightning Jumps warnings per county [LJ/km^2]; (c) Density of population per county [Inhabitants/km^2]. The category division is based on equal count (quantile). Counties are indicated in grey lines and the optimal 30° dual-lobes for the XRAD are presented in dotted-line circles.

9.2.2 SAMURAI performance

SAMURAI has been originally tested over a total of five severe cases, although this chapter is focused on two main cases to analyze the dynamics. Except for the tornado case here analyzed, the other cases where isolated cells affecting inland areas, and that produced large hail or strong severe gusts. For all the five cases, it was previously done a fast verification test to see how close were the retrieved SAMURAI radial velocities from the observed ones. In this sense, the Root Mean Square Error (RMSE) between the Retrieved-Observed data was obtained for all the cases. It is worth to mention that for four of the five cases, the mean RMSE was below $1.8\,\mathrm{m\,s^{-1}}$ except for one case that the mean value was $2.3\,\mathrm{m\,s^{-1}}$. This was the case of an unusual weather overnight system that occurred in Catalonia on 6-7 January 2018, producing two tornados, one of them analyzed with SAMURAI in the present chapter. The high RMSE value was produced because, although being the case closest to the radar pair, the tornado-producing supercell was rain-wrapped, and there were a lot of weak returned echoes masking the real structure. This made the clean-up process difficult, and clutter targets were not completely removed, therefore, introduced in the analysis. Also, there were missing pixels that were removed because of the aggressive pre-processing filters, as explained in the Chapter 4. However, after a deep analysis of the resulting structure and its dynamics, the SAMURAI results were surprisingly good and worth discussing. This case is described as follows. The other case analyzed in this chapter is the case of 2013, which has been used previously in this thesis. This was chosen because of its complexity, is the more difficult to forecast of all the five other cases, and because of the clear and strong topographic influence in the event.

The severe weathernevent on 6-7 January 2018 occurred outside the convective season, which in the northwestern Mediterranean is between May and September inland (Chapter 5), and extended to late autumn for the coastal area (Chapter 8), and it occurred overnight, while the usual thunderstorm period in Catalonia is between 12 and 19 UTC. Several rain bands with a predominant southeasterly flow affected the area. Within those bands, embedded convective cells produced severe weather, causing two significant tornadoes, both rated EF2 (Enhanced Fujita scale, McDonald et al., 2010). One of those tornadoes affected the central region of Catalonia, damaging farms and the surrounding pine woods, and was particularly interesting concerning the supercell propagation because it was channeled completely through a narrow valley. This can be seen in Figure 9.5, which shows the track of the convective cell that produced the tornado, overlaid on the topography. Due to the resolution and the scanning strategies, the radar could not observe the tornado itself (smaller than 1km wide and with high shear that would result in aliasing). Also, the tornado was channeling in the valley (ground valley floor ≈ 250 m MSL), and the closest radar, CDV, was located 42 km away at 825 m MSL. This implies that the lowest radar beam was at ≈ 440 m AGL with respect to the radar, which is ≈ 1,000 m MSL. Although the radar was not able to see the tornado itself (asterisks in Figure 9.5), the mesocyclone was visible in several consecutive volumes.

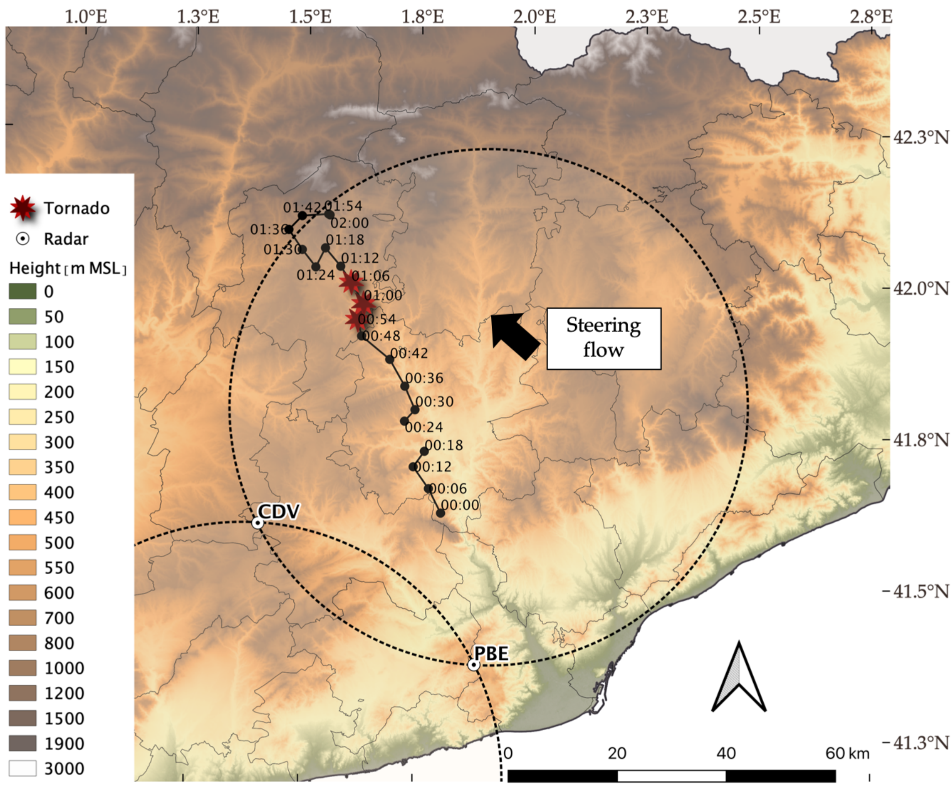

Figure 9.5: Track of the nocturnal winter tornadic supercell on January 7, 2018 over topography. Part of the 30° CDV-PBE pair dual-lobes is depicted in dotted lines; red stars indicate the location of the confirmed tornado after field damage survey and the times [UTC] indicate the centroid of the tornadic supercell identified with the radar-based algorithm from (del Moral et al., 2018b). The black big arrow indicates the steering flow.

Figure 9.6a shows the raw reflectivity field, suggesting the typical hook echo associated to supercell thunderstorms. The mesocyclone is demonstrated with the radial velocity data (Figure 9.6b), where the couplet of velocity is depicted at ≈ 26 km east from CDV radar. In this case, the raw velocity data is dramatically thresholded (see again the processing of the data explained in Chapter 4; the aggressive filtering of the data during the operational processing results in a loss of practically half of the mesocyclone in all the volumes (white pixels in dashed circle in Figure 9.6b). As explained previously, the SAMURAI technique allows us to minimize this problem if choosing the correct Gaussian and spline filters to extrapolate the data available and fill the holes during the analysis. This is shown in Figure 9.7, where it can be seen how all the fields over the missing points are retrieved with consistency. The reflectivity and the horizontal wind field at 1 km height is depicted in Figure 9.7a, where it can be seen the southeasterly steering flow that was leading the entire system (arrows indicate $10\,\mathrm{m\,s^{-1}}$). It also can be seen the large area of weaker reflectivity values surrounding the main supercell, indicating the rain wrapping the thunderstorm, and a region, at the southeast corner where the wind is slightly more intense and converging to the rear part of the supercell. This is consistent with a weak rear inflow jet, which feeds the main updraft region (red area in Figure 9.7c).

SAMURAI also resolves the closed circulation in the storm-relative horizontal winds (black arrows in Figure 9.7b) which corresponds to the mesocyclone at mid-levels (2.5 km AGL), and the area with a couplet of positive and negative vertical velocity (blue and red in Figure 9.7c, for negative and positive values, respectively). This depicts the main updraft (red shaded) and the corresponding forward-flank downdraft (blue shaded) of this rain-wrapped supercell, consistent with the conceptual supercell model proposed by Lemon and Doswell III (1979), and adapted by Markowski and Richardson (2011). Furthermore, although depicting a complicated vertical vorticity retrieval, in 10^{-5} s^{-1}, (other smaller scales are probably contaminating the main cell itself, being this a Heavy Precipitation (HP) supercell), it can be seen the main couplet coinciding witht the updraft-downdraft area, with the highest values perpendicular to the steering flow. This depicts a crosswise vorticity, where the original horizontal vortex lines are perpendicular to the storm-relative motion. This could have been helped by the orientation of the valley itself, enhancing the final tilting of the vortex lines. All of these common supercell features retrieved with SAMURAI demonstrate that the technique successfully overcame the heavily-filtered data, and that it is an effective tool to use with an operational C-band radar network.

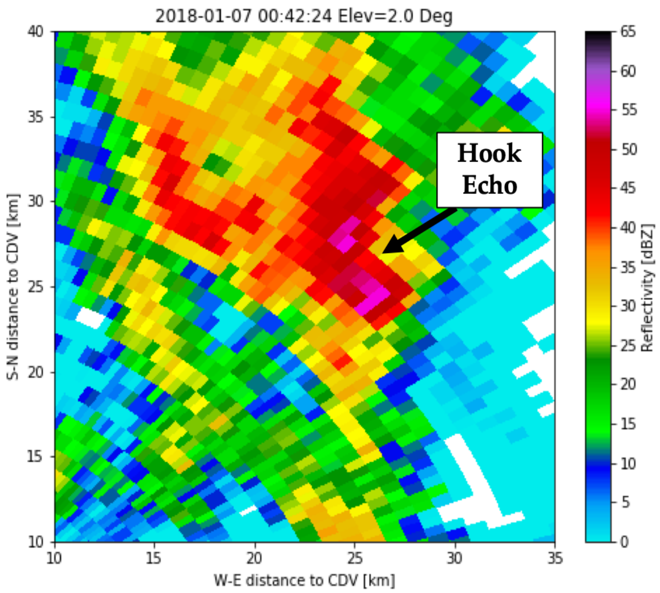

(a)

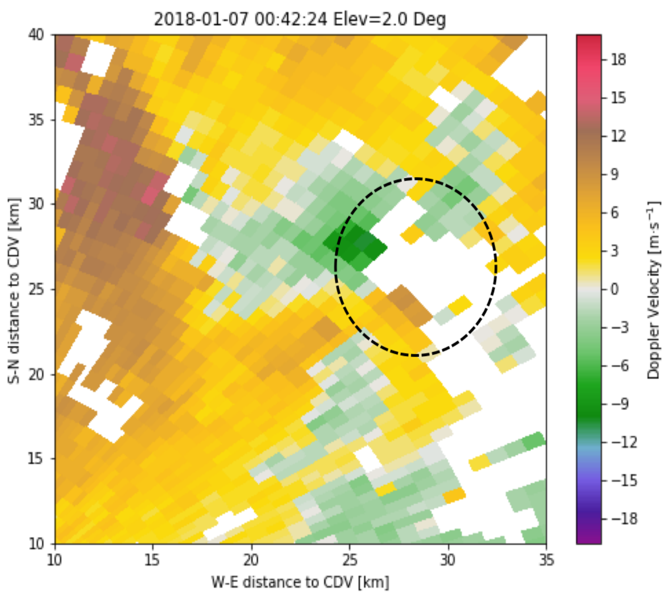

(b)

Figure 9.6: Raw CDV radar fields for the supercell case on 7 January 2018 at 00:42 UTC at 2° elevation angle. (a) Reflectivity [dBZ]. (b) Dual-PRF outliers-corrected Doppler velocity [$\mathrm{m\,s^{-1}}$]. Dashed circle indicates the area with missing pixels.

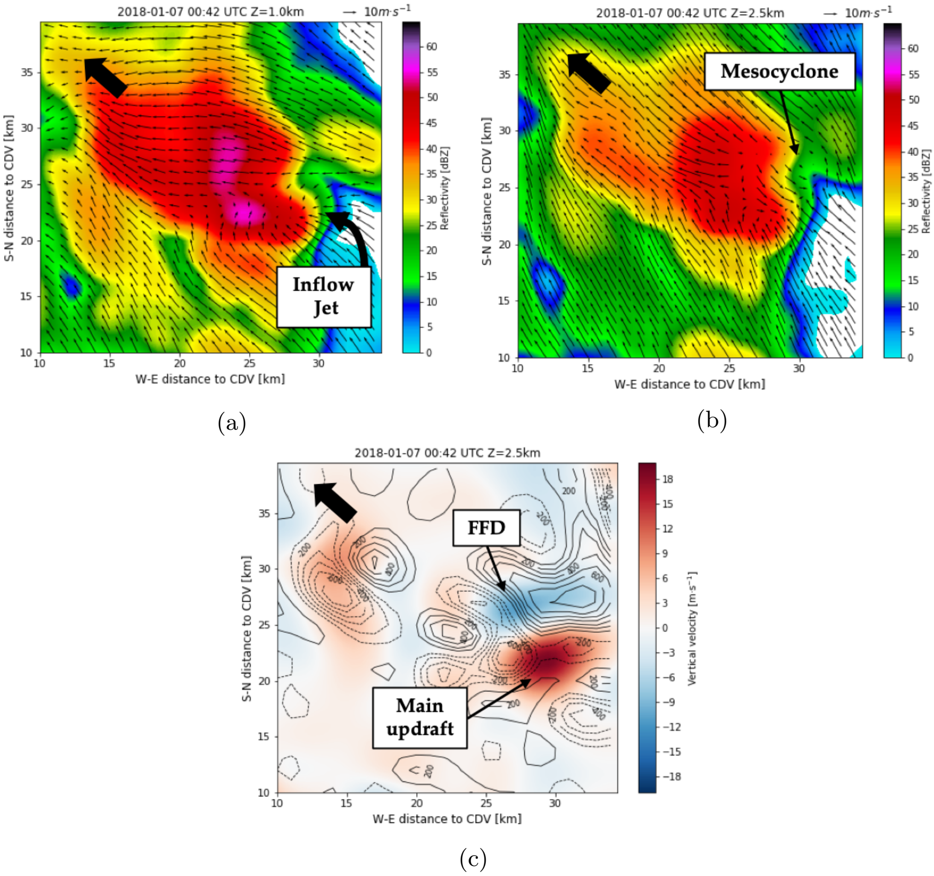

Figure 9.7: Retrieved SAMURAI fields for the supercell case on 7 January 2018 at 00:42 UTC . (a) Reflectivity [dBZ] and storm-relative horizontal wind field [$\mathrm{m\,s^{-1}}$] (in black arrows) at Z=1 km and (b) Z=2.5 km. Z represents the height AGL on respect to CDV. (c) Vertical velocity in color scale [$\mathrm{m\,s^{-1}}$] and vertical vorticity [$10^{-5}\ \mathrm{s^{-1}}$], represented in black contours (dashed and solid for negative and positive values, respectively). Contours are labeled every $200 \times 10^{-5}\ \mathrm{s^{-1}}$ (0 not shown). FFD stands for Forward-Flank Downdraft. The black big arrow indicates the steering flow.

9.2.3 Dynamical influence of topography

On July 10, 2013, a large splitting severe thunderstorm caused losses of more than 80 % of the corn crops and fruit tree fields due to large hailstones (3 to 4 cm) and wind gusts. The storm, analyzed in Chapter 6, and in del Moral et al. (2018b) from a radar-based tracking point of view, split into two perfect mirror images (Figure 9.8). After that, the two resulting daughter storms (marked as number 2 and 3 in Figure 9.9), propagated completely in the opposite direction (see arrows indicating left and right mover, and centroid time and locations in Figure 9.9). The split resulted in an enhanced left mover (notice that this term is related to the steering mean flow), which propagated for a long time (more than 2 hours) across topography and against the mean flow (large black arrow in Figure 9.9). Cells 4 and 5 took place in the final merging with cell 3, and formed a bigger linear system, although these are not considered in the present analysis, since we wanted to focus our attention in the first splitting mechanism.

Mesoscale mechanisms associated with splitting storms may imply a strong vertical shear which enables the vorticity tilting process. A common synoptic-scale flow that favors such conditions is a strong jet at 300 hPa with the exit region over the storm area, enhancing the instability and lifting conditions, along with a tilted and strong low-level jet (850 hPa) that may enhance the shear (see, for instance, the "Supercell Cookbook" at https://www.weather.gov/). Nevertheless, on July 10, 2013, the exit area of the at 300 hPa was located over eastern Mediterranean due to a cut-off low at that same level over north of Catalonia. This created a strong northwesterly entrance flow located over the northern coast of Spain (west of Catalonia), leaving the higher values of instability over the Ebro Valley instead of Catalonia (≈ 200 km west of the thunderstorm location) (not shown). The sounding of Zaragoza, ≈ 160 km west of the thunderstorm, and closer to the area with more instability, indicated a 0-6 km shear vector of $20.18\,\mathrm{m\,s^{-1}}$ (not shown). This is more conducive to multicellular systems rather than supercells (Weisman and Rotunno, 2000). Also, it indicated a westerly shear (269°), which did not coincide with the needed direction for the final NE and SW propagation (Figure 9.9).

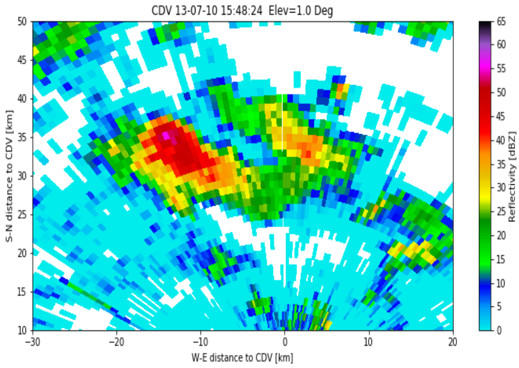

(a)

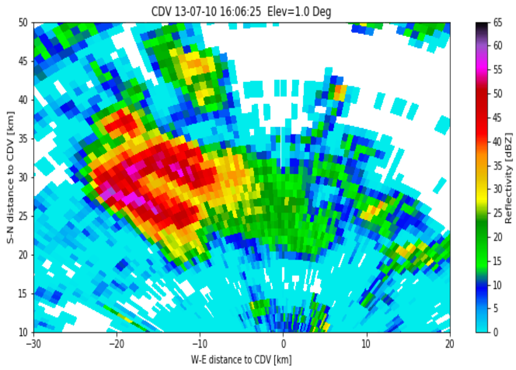

(b)

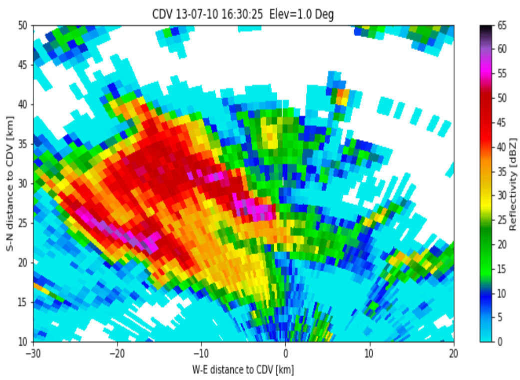

(c)

Figure 9.8: Raw CDV radar reflectivity for the splitting case on 10 July 2013 at 2° elevation angle. (a) 15:48:24 UTC (primary cell to the left). (b) 16:06:25 UTC (during splitting). (c) 16:30:25 UTC (daughter cells after splitting).

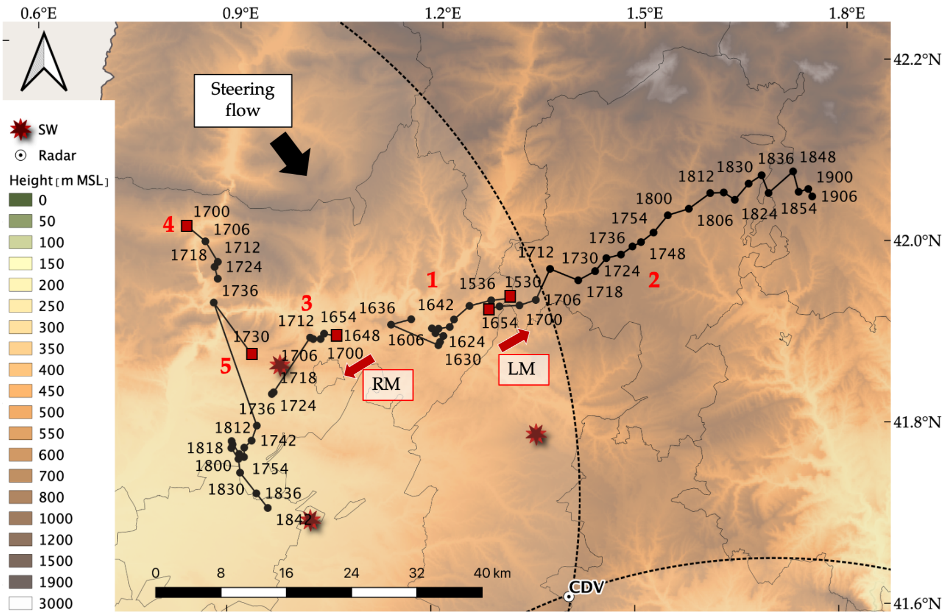

Figure 9.9: Track of the splitting storm on July 10, 2013 over topography. Part of the 30° CDV-LMI pair dual-lobes is depicted in dotted lines. Red stars indicate Severe Weather (SW) occurrences (wind gust and hail). Red numbers indicate the different cells that took place in the system identified by the algorithm presented in Chapter 6 and in del Moral et al. (2018b), being 1 (primary cell), 2 (left mover) and 3 (right mover), the ones of interest taking part in the splitting process. Cells 4 and 5 took place in the final merging with the cell 3, and formed a bigger linear system. Black squares indicate the starting point of the left (cell 2) and right (cell 3) movers, and red arrows indicate their propagation directions. The black big arrow indicates the mean NW steering flow (direction of propagation for the majority of the cells during that day).

The reflectivity and the horizontal wind field (upper and mid-row), as well as the vertical velocity and vertical absolute vorticity (lower row), before and after the splitting are shown in Figure 9.10. First, it is worth mentioning that the splitting does not start to be visible until 16:06 UTC (Figure 9.10b), and even at that time, the shape does not coincide with the usual splitting pattern. During the time steps before splitting (Figure 9.10a), the entire pattern is more similar to a multicell system since, during almost one hour, different small cells grow and dissipate near each other (see, for instance, Figure 9.10b, Figure 9.10d and Figure 9.10e). Figure 9.10a and Figure 9.10b show a strong shear in the storm area, with southeasterly flow at low levels, and a northwesterly strong flow at upper levels (coinciding with the synoptic maps at 300 hPa commented previously, ans which is seen in Figure 9.10d, Figure 9.10e). It is also in Figure 9.10d and Figure 9.10e that can be seen how, at Z=4 km, there is a formation of a convergence line of winds (square and dashed lines), indicating another region where new cells are formed. In a heterogeneous multicell environment, that configuration would help the formation of the new cells upstream of the low-level flow, resulting from the lifting mechanism of the gust front of the preceding cells (downshear flank of the outflow).This is visible in Figure 9.10h and Figure 9.10i, marked with an arch, where it can be seen how different updrafts appear upstream of the low-level wind, although not long-lasting. Despite that clear configuration, it is also seen how the general movement of the cells is towards the southwest (framed in black in Figure 9.10d and Figure 9.10e), demonstrating the possible role of the topography in the system movement and propagation.

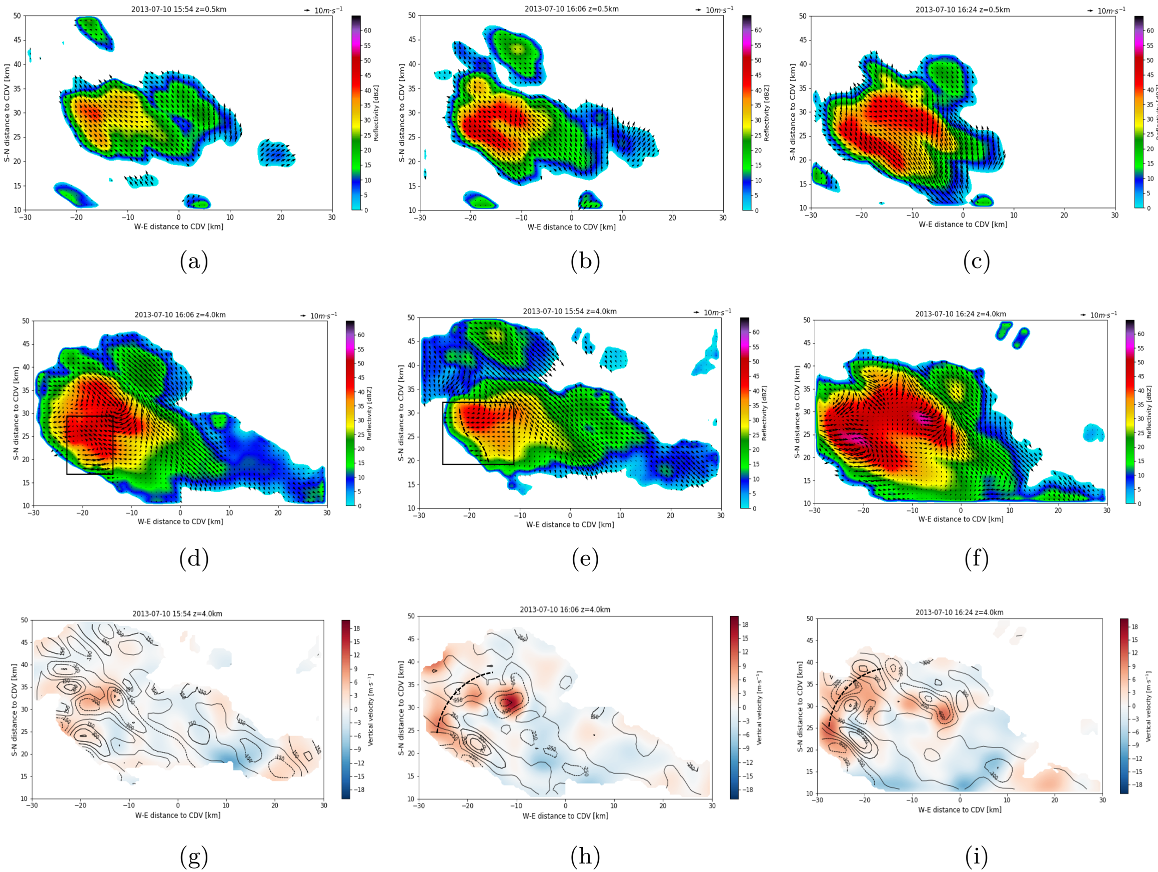

Figure 9.10: SAMURAI retrievals for the splitting case on 10 July 2013 at Z=0.5 km (upper row), and Z =4 km (mid and lower rows). (a-f) Reflectivity [dBZ] and storm-related horizontal wind field [m s^{-1}] (in black arrows). (g-i) Vertical velocity [m s^{-1}], represented in red and blue contours, for positive (upward) and negative (downward) velocities, respectively, and vertical vorticity [$\times$ 10^{-5} s^{-1}], represented in black contours (dashed and solid for negative and positive values, respectively). Contours are labeled every 200 $\times$ 10^{-5} s^{-1}

Figure 9.11 shows the reflectivity and horizontal wind field at 15:42 UTC at 3.5 km. It can be seen how there is a divergence of the wind (marked with black arrows in Figure 9.11a) with the formation of a convergence line at mid-levels (dashed line in Figure 9.11a). The streamlines coincide with the topography of the site, which follow the ridge orientation, as shown in Figure 9.11b. This seems to enhance the storm-relative winds, and therefore modifies the dynamics of the system. That configuration allows the creation of new cells in such direction (southwest).

Figure 9.12 shows the same time-step as Figure 9.11 with the horizontal reflectivity and wind at 0.5 km and a cross section from point A to B (Figure 9.12a). The cross section, along the southwest-northeast direction, depicts the formation of the new cells at mid-levels, where a new cell core can be seen (area with higher values of reflectivity) with a strong frontal lifting (updraft indicated in solid contour lines, Figure 9.12b). Although this configuration seems to be predominant in the initial time steps, causing the new cells to converge in the southwest region and creating a major flank, it follows a similar pattern in the opposite direction (northeast) where another convergence line is created and a major cell starts to form (see, for instance Figure 9.10e). That divergence at mid-levels, modulated by the topography, seems to be the cause of the splitting storm. It separates the entire system creating two major flanks where the cells will be enhanced afterwards, still maintaining the original downshear flank with the southeast flow against the ridge. This is seen with the inverted-U shape in the reflectivity field in Figure 9.10f. Also, at that moment, the two major resulting updrafts, created with the convergence at mid-levels, start to organize as single cells (two significant updrafts shown in shaded red in Figure 9.10h and Figure 9.10i). The strong divergence at mid-levels could also be the mechanism forcing the crosswise vorticity to tilt along the A-B axis in Figure 9.12a. This is the final cause of the creation of a two-vortex couplet at 16:18 UTC (not shown), visible also at 16:30 (Figure 9.10i). The result is two clear cells (Figure 9.10i), moving in opposite directions with cyclonic and anticyclonic circulations, therefore, supercell type.

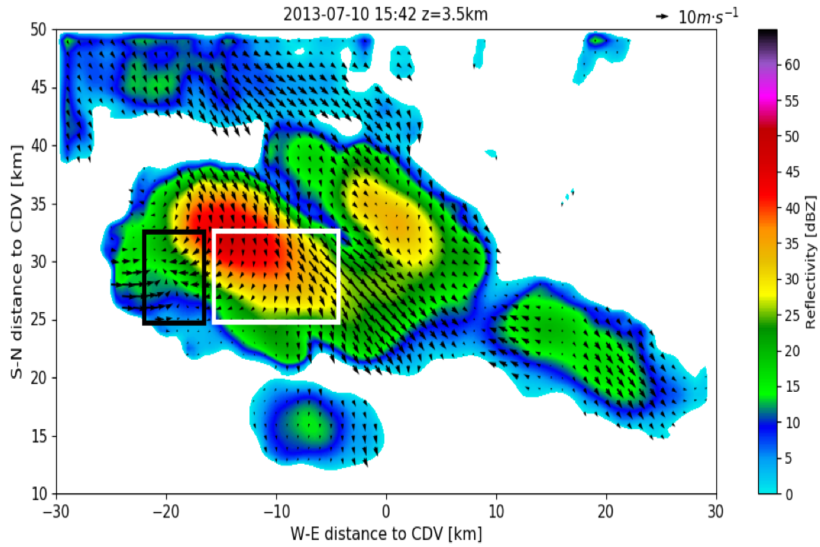

(a)

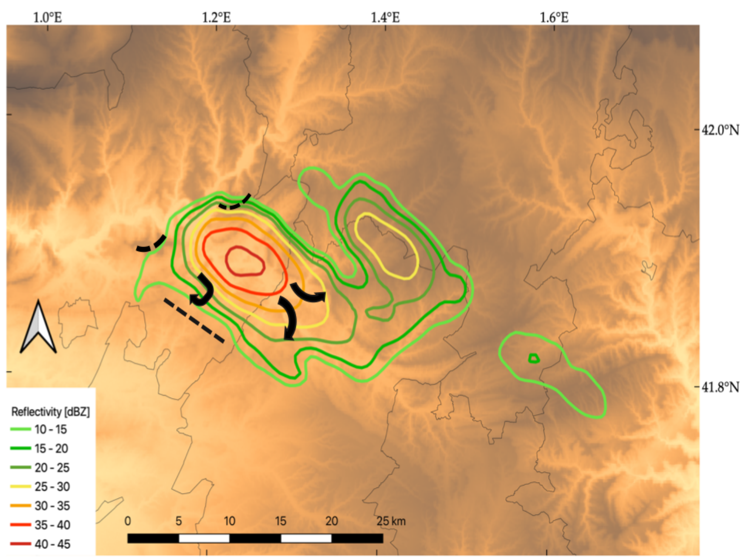

(b)

Figure 9.11: (a) Retrieved reflectivity and horizontal wind field at 15:42 UTC at Z=3.5 km for the storm on July 10, 2013. The black box and white indicates the area with converging and diverging winds,respectively. (b) Retrieved reflectivity as in (a) in contour lines, over topography. Black arrows indicate the wind flow over the the respective areas and dashed lines indicate the ridges affecting the storm and modulating the wind.

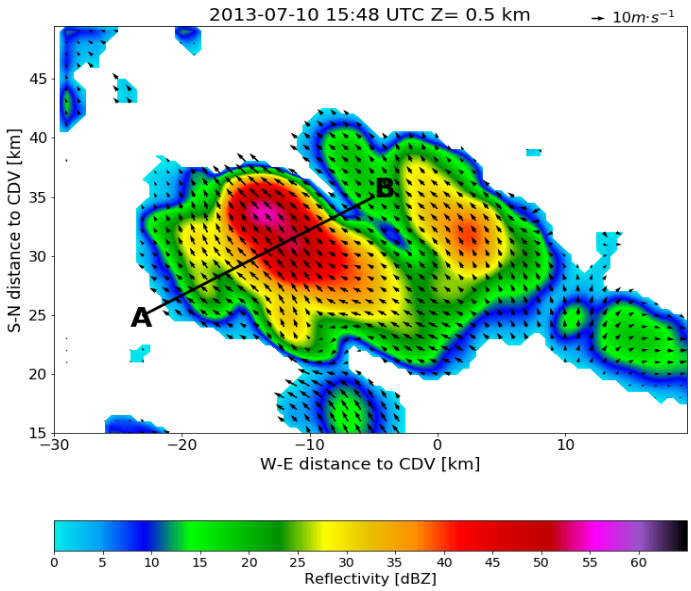

(a)

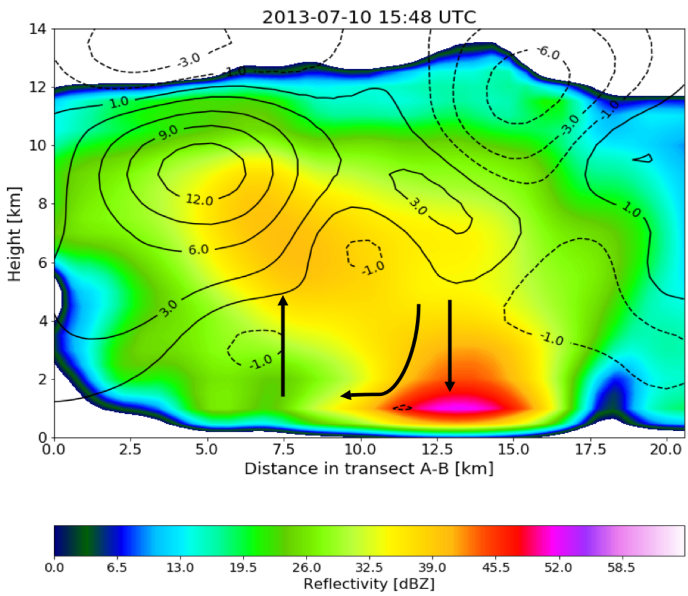

(b)

Figure 9.12: (a) Retrieved reflectivity (in dBZ) and horizontal wind field (arrows) at 15:48 UTC at 0.5 km for the storm on July 10, 2013. The black line indicates the transect for the vertical cross section in (b) (from A to B). (b) Reflectivity (in dBZ) vertical cross section along the transect [A-B]. Contour lines indicate positive (solid) and negative (dashed) vertical velocity (w, in m s^{-1}). The thick big arrows indicate the main drafts inside the storm.

The vertical structure of the initial stage (16:24 UTC) of the two resulting supercells is depicted in Figure 9.13. Figure 9.13b shows the vertical reflectivity structure with the vertical motion (positive in solid contours and negative in dashed contours), while Figure 9.13c shows the vertical motion (positive in red shade and negative in blue shade) with the vertical vorticity (positive in solid contours and negative in dashed contours). Both cross sections are made along the line C-D shown in Figure 9.13a, the axis of the main horizontal vorticity. Figure 9.13b clearly shows the two main cells, completely separated and tilted towards the direction of propagation. It can be also seen two couplets of updrafts-downdraft from mid-upper levels. This could be related to the main inflow direction and the rear-flank downdraft. Also, Figure 9.13c depicts two more couplets in this case of vertical vorticity. It is seen how the maxima (900×10^{-5} s^{-1}) and minima (-300×10^{-5} s^{-1}) values at 16:24 UTC are located around 4 km and orthogonal to the image plane. This indicates that the LM (relative to the main wind flow) is rotating cyclonically, and the RM anticyclonically.

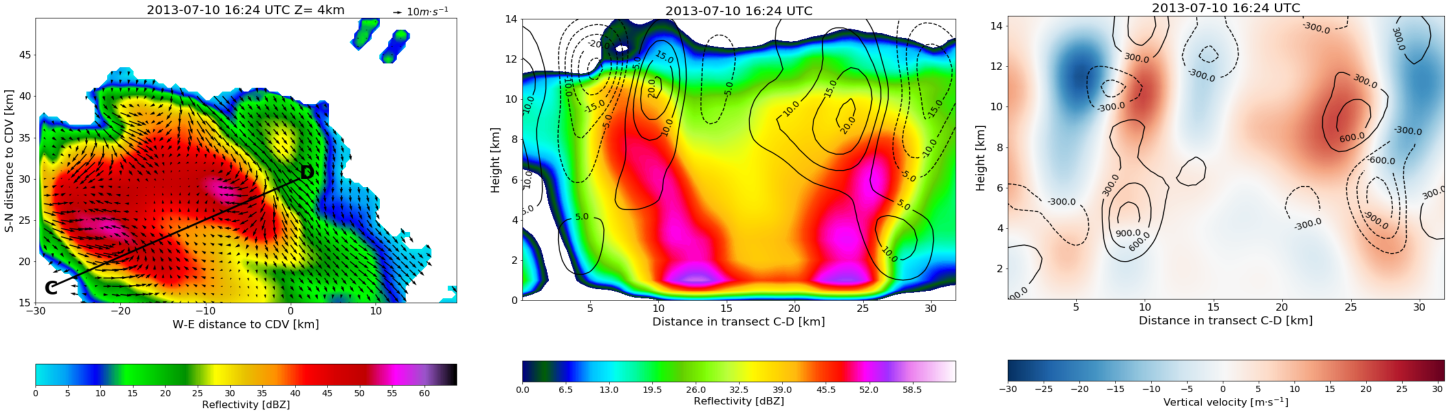

(a) (b) (c)

Figure 9.13: (a) Retrieved reflectivity (in dBZ) and horizontal wind field (arrows) at 16:24UTC at 4 km for the storm on July 10, 2013. The black line indicates the transect for the vertical cross section in (b) (from C to D). (b) Reflectivity (in dBZ) vertical cross section along the transect in [C-D] Contour lines indicate positive (solid) and negative (dashed) vertical velocity (w, in $\mathrm{m\,s^{-1}}$). (c) Vertical velocity (w, in $\mathrm{m\,s^{-1}}$) along the transect in [C-D]. Contour lines indicated positive (solid) and negative (dashed) vertical vorticity (ζ, in $[\times\ 10^{-5}\ \mathrm{s^{-1}}]$).

9.3 Conclusions

In the present chapter, an open-source variational multiple-Doppler software, SAMURAI, is applied in Catalonia to study in deep the dynamic features of two severe weather events. This work constitutes a pioneering study in a southern European country, thanks to the geographical configuration of the XRAD, the radar network of the Meteorological Service of Catalonia. It is the first time that SAMURAI is used for analyzing severe weather at a thunderstorm scale and in complex terrain, and this chapter shows the capabilities of the software for solving different situations in which the anomalies of the original data (de-aliasing and aggressive velocity filters removing part of the data, especially in strong-shear situations) do not allow to characterize the internal thunderstorm dynamics. These issues are common in most of the operational European weather radar networks.

With the analysis of the tornadic thunderstorm on January 7, 2018, the present work demonstrates that SAMURAI constitutes a powerful tool for storm analysis in dramatic situations: a tornado occurring within a valley (radar beam blocking), operational (fixed radar scan mode) and C-band radars (not enough resolution for resolving storm-scale features), and aggressive pre-filtering of radial velocity (loss of half of the mesocyclone in raw data). By using a variational method that includes two different data processing filters (Spline and Gaussian), we have been able to successfully retrieve the mid-level mesocyclone of the tornadic thunderstorm, as well as the couplet updraft-downdraft associated with the circulation. One of the good things about the way that SAMURAI handles mass continuity is the local application of the constraint rather than via integration of the equation itself. As a result, we can trust the winds above the terrain quite well, since no errors are propagated through the vertical. The need to improve how SAMURAI handles the winds near the surface remains, particularly when the storm is over topography. However, the work demonstrates that SAMURAI can be applied to retrieve mid-level circulations and provide information about key features of organized thunderstorms, such mesocyclones, updrafts and vorticity couplets. The software is being improved by applying directly the topography in the analysis which will enhance the retrieved near-surface winds in complex terrain.

Furthermore, the analysis of the anomalous (weak convective environment) splitting thunderstorm case on 10 July 2013 has shown that the technique allows the identification of the features and internal core interactions that lead to the separation of the two main cells. Although the procedure cannot yet be applied in real time, the use of this methodology in those cases with complicated internal dynamics results in an improvement in the knowledge of the nature of these anomalous thunderstorms (frequent in Catalonia). In the analyzed case we have detected that, contrary to most of the splitting storms reported in the literature that present strong shear in the environmental winds and a primary single cell, the final splitting process here reported was a response of a major system (multicell) interacting with its surrounding conditions, especially the topography. It was the result of an enhancement and organization of different cores in the rear flank of a multicell system, due to the proximity to a steep orographic ridge, which also enhanced the mid-upper level winds. The splitting process occurred after the organization of the main two supercells, which started at high levels, and no initial vertical vorticity couplet was depicted before the split. SAMURAI retrievals successfully provided information about the vertical structure and associated wind field of the thunderstorms during the entire life cycle.

Besides, with this analysis, it is demonstrated that in order to understand how severe thunderstorms evolve and behave during the entire life cycle it is necessary to put effort into retrieving the wind field at all levels, not just to focus on what happens near the surface. This is usually achieved with idealized numerical simulations at high resolution or with multiple-Doppler analyses in field campaigns with X-band radars providing better spatial resolution than operational radar networks. For the first time, complete wind fields have been achieved with an operational C-band radar network, providing a three-dimensional view of the wind field inside a thunderstorm in, the Iberian Peninsula, constituting an important success for the meteorological community.

Part IV
CONCLUSIONS

10

Summary and conclusions

In the present context of climate emergency worldwide, with greater impact in some regions such as the Mediterranean basin, it is necessary for the improvement and adaptation of the early weather systems. Just as important as the improvement in instrumentation and techniques, is the refinement of the knowledge of thunderstorm dynamics and related phenomena, as it has been demonstrated over the years with numerous study cases and projects. As stated in Chapter 2, the present thesis has been based from the beginning in a major hypothesis formulated after the wide experience of the meteorological community in the region, and that has become the foundation for the objectives proposed in this work:

The complex topography and the proximity to the sea play a major role in mesoscale dynamics, impacting directly in thunderstorms producing severe weather phenomena.

This hypothesis has led to defining the main objectives of the thesis that are solved in the following sections.

To advance in the knowledge of thunderstorm-scale dynamics in Catalonia (applicable also in other world regions), identifying the influence of complex topography and the sea in their life cycle, and especially in their propagation, as well as their capacity of producing severe weather, to improve the nowcasting of these thunderstorms and phenomena.

This objective represents the main purpose of the present work. In consequence, it has been achieved throughout the different chapters of this manuscript. In this sense, we can distinguish two different convective regimes in Catalonia, intensely studied in this work. First, the isolated deep convection occurs inland, presenting a significant influence of topography. On the other hand, the coastal shallow convection results in efficient precipitation, which is caused by the strong maritime component. In the first group, we can find highly developed thunderstorms, usually with severe hail and wind-related phenomena. These thunderstorms usually occur during spring and summer and are related to the diurnal cycle, therefore occurring in the afternoon or evening with high instability and buoyancy-related indexes. This group of thunderstorms is the one presenting more anomalous propagation patterns, especially of splitting, since their self-organization and their interaction with the surrounding thunderstorms and topography enhances their complex dynamics. Some of the examples of topography influence found in the present work are the intensification of low-level winds that can enhance weak shear environments, helping in the tilting of main updrafts or the rotation. Another factor is the channeling effect at low or mid-levels, that can change the steering wind of the thunderstorm and make it follow unexpected paths. Also, topography acts as a triggering factor for new-born thunderstorms, by enhancing the lifting of the cold pool of the preceding ones, or by creating boundary layers.

On the other hand, in the coastal convection group, we can find more not so developed thunderstorms (shallow convection) but efficient, due to a strong maritime influence that feeds the lower atmospheric layers with moisture. In this case, these thunderstorms usually affect the coastal regions in autumn, when there sea surface temperature is higher and therefore there is more precipitable water content in the atmosphere in unstable conditions. These thunderstorms are short-lived although these are organized in major systems like Mesoscale Convective Systems or convective lines. These usually travel from the sea to inland usually as convective trains and affecting the same area for long periods of time. In this case, the topography plays two different roles in the dynamics of these thunderstorms, which usually evolve into flash floods in the area. First, as a triggering mechanism of new cells when the instability is located over the shore, and therefore helping new-born cells to grow upstream of the rivers, and second, as a capping mechanism for those cells with slow motion, and enhancing the *in situ* convective precipitation.

10.1 Specific objectives

1. **To create a fast and reliable method to identify thunderstorm propagation patterns, to be applied not just in our region but also in areas where no weather radars are available:**

   This objective has been solved in Chapter 5 and published in del Moral et al. (2017). It has been demonstrated that convective structures can be defined based on the daily precipitation field, imposing a minimum of 15 mm in the 24 h QPE value and an extension of 6 km^2. This allows reducing noticeably the amount of data to analyze in climatological studies since there's no need to handle volumetric radar data with a temporal resolution of minutes (6 min in our region) to obtain a first picture of the convection and propagation in a region. This implies that the approach can be applied in a region without radar information if there exists other rainfall information from which could be derived the QPE (a rain gauge network, for instance). Furthermore, the technique allows obtaining results that can be used to study behavioral trends for convection in a daily temporal scale, which is comparable to most of the NWP models and climate change scenarios outputs.

2. **To retrieve a climatology of thunderstorms occurrence and anomalous propagation in the area of Catalonia, to establish the main patterns in our region:**

   As well as the previous objective, this is also solved in Chapter 5 and published in del Moral et al. (2017). The study conducted by analyzing the daily rainfall convection footprint between 2008 and 2015 in Catalonia shows that convective activity takes place mainly from May to September, this is, between spring and early autumn. Convection is mainly located near mountainous areas, especially in the east Pre-Pyrenees, due to the conjunction of moist advection from the Mediterranean Sea and the orographic lifting processes. This coincides with the maximum spatial distribution of lightning activity shown by Pineda et al. (2011), who defined the region as an area of convergence, and with the area with maximum daily precipitation shown by Llasat et al. (2007).

   Bearing in mind the life cycle of a thunderstorm, the rainfall footprint can be categorized in Elliptical (E) and Non-Elliptical (NE) shapes. It is demonstrated that E structures are associated with isolated thunderstorms with a defined life cycle (*cumulus*, *mature* and *dissipating* stage). On the other hand, NE structures are associated with thunderstorms with anomalous propagations and/or clusters of cells. As of the convective activity, the number of structures increases between spring and early autumn, being the NE ones, the most common pattern in the Catalan region.

The three most repeated NE patterns, this is, shape indicators of anomalous movements, are: circular, V-shape, and elongated. The first type is associated with convective structures with slow motion or topographically anchored. The rainfall footprint becomes circular-type due to the location of the most active region of the structure in the same place for a long period. The second type, V-shape, is associated with the splitting of thunderstorms and changes of the thunderstorm propagation during their life cycle. Some merging processes would be also described by this type of shape if the resulting thunderstorm stays stationary or follows the same path of one of the preceding ones. However, a variant of a V-shape structure appears if the resulting cell follows a perpendicular direction from the point where the merging process has occurred. The structure then results in a Y-shape. Finally, the third type is, as its name indicates, associated with structures with a long footprint. In isolated structures, this is the result of a long-lasting thunderstorm, as it could be a supercell or thunderstorm with a constant feeding mechanism or strong winds aloft that makes it propagate further in space in a shorter period of time.

It is important to remind that this first classification serves as a "first picture" of the possible anomalous movement associated to thunderstorms in the region, although for deep knowledge and explanation of the causes and triggering factors, it is needed a higher temporal and spatial resolution data to analyze (provided by the weather radar), which fits better to the nature of the phenomena.

3. **To improve the algorithm for identification and tracking of thunderstorms from the SMC. In concrete:**

   - **To differentiate thunderstorm tracks when there is a high convective activity (cell clusters).**
   - **To retrieve more realistic thunderstorm life cycles, getting better continuity in shape and intensity.**

- **To identify, in advance of occurrence, possible splitting of thunderstorms and/or merging processes.**

This objective is solved in Chapter 6 and published in del Moral et al. (2018b). Apart from the three sub-objectives presented above, other accomplishments have been obtained and are described as follows.

The algorithm has served as the main tool for the analysis done in Chapter 7 and Chapter 8. A new algorithm for convective cell identification and tracking has been developed, for severe weather surveillance purposes, enhancing the current operative algorithm at the SMC. This new algorithm adds a preprocessing stage of the radar image before the 2D identification, by removing structures close to 30 dBZ (minimum reflectivity value imposed to define a convective cell) that are smaller than 10 pixels ($40\,\mathrm{km}^2$). Also, it is added a filtering process of extremely intense echoes around the radar position. These two processes help to discard false echoes that could result in false small convective cells.

The 2D identification is done using a different rule for pixel labeling, considering more adjacent pixels (Queen's Case – 8 pixels), and a second seven reflectivity (30, 35, 40, 35, 50, 55, 60 dBZ) bottom-up threshold process. In the first case, it allows retrieving more realistic 2D cells by imposing less restrictive area definitions, which results in continuity and naturality of the final thunderstorm life cycle. In the second case, the second thresholding allows for a better distinction of the cells embedded in multicell systems, or on a day with a high density of isolated cells. This allows not to discard small cells growing near those that are more developed, and therefore differentiate final tracks in high convective activity.

The 3D or volumetric identification has been changed to an overlapping technique of the 2D structures in every CAPPI level, instead of centroid distance matching. This is still a 3D identification but retrieved differently from the previous algorithm. This facilitates the knowledge of possible internal processes, by analyzing the multiplicity of 2D structures in different CAPPIs throughout the entire volume of the 3D cell. In this sense, during the 3D identification, it appears the first possible warning of a splitting or merging process (M2D). This warning can help forecasters to put their attention on that thunderstorm and monitor its evolution.

Finally, the connection of 3D cells in the new tracking module is done by adding an area-dependent distance threshold for consecutive image association (t-6 min) and a maximization of multi-variable-dependent (ZMAX, HTOP40 and centroid distance) function for two consecutive image association (t-12 min). This tracking method allows to track thunderstorms that are born very close to others in a different phase of development, (high convective activity), to maintain realistic paths where thunderstorms are tracked from cumulus to dissipating stage, and to track anomalous movements such splitting or merging. It is in this module where one of the most remarkable warnings appear, indicating a possible merging (PM) and/or possible splitting (PS) process, giving extra valuable information when monitoring thunderstorms, and posing the focus in thunderstorms that can present severe weather. An extra warning is issued if new-born cells appear with really high vertical development (WTOP7). This serves as a "second chance" anomalous movement warning since it can indicate that a thunderstorm resulting from such processes has not matched the tracking requirements, although it needs to be considered as a potential for severe weather. It is important to remark that this process is not contradictory to the results from Tsonis and Austin (1981) explained in Chapter 1, since a fixed trend is not imposed, and parabolic curves are not used to extrapolate future echo sizes.

4. **To verify the improved identification and tracking algorithm in different convection regimes: severe weather and coastal adverse weather:**

   This objective is solved mainly in Chapter 7 and Chapter 8 and published in del Moral et al. (2018a) and del Moral et al. (2020a). In the first study it is presented the validation over 30 severe weather cases in Catalonia, from two different perspectives; the ability to identify in advance a split or merge process during the 3D identification module (M2D) and to identify it during the tracking module (PS and PM as a first warning and WTOP7 as second). The verification shows that about 85 % of the cases with anomalous propagation presented M2D warnings at some point in their entire life cycle, being more than 65 % displayed in advance of the split/merge process, with a 30 min lead-time in average. It is also demonstrated that the tracking module is the most reliable one since it has two chances of identification. As a first stage, evaluating the PS/PM warnings, the Probability of Detection (POD) score results in 0.67, which is increased to 0.83 when the second stage (WTOP7 warnings) is performed. This indicates the ability of the new algorithm to correctly detect those processes. Also, the algorithm resulted in having a good ability to separate the anomalous movement thunderstorms with those without anomalous movement (no Anomalous Movement, NAM, thunderstorms). This is tested with Peirce's Skill Score (PSS), that results in 0.58 and 0.73, for the first and second stage respectively.

The algorithm is also validated when used to study the convective regime in a coastal area (Chapter 8). In this case, it is applied to an extended period of time and focused in a particular densely populated region. The algorithm performs with accuracy when correctly identifying and tracking the convective cells in 4 years, with shallow and short-lived thunderstorms, this is, with completely different convective characteristics than the first validation (isolated deep convection).

5. **To identify the main thunderstorm features and the influence of the topography and the sea over a touristic coastal area with a high occurrence of flash floods:**

   The present and the following objectives are solved in Chapter 8 and published in del Moral et al. (2020a). In this case, the coastal town of Salou is used as a testbed area to analyze flash floods-producing convective events. This is a very densely populated area, surrounded by complex topography and a short response hydrologic basin, which will increase its vulnerability in the future. The new identification and tracking algorithm is applied for the period 2014-2018, showing the highest activity in this coastal area between September and November, presenting shallow convection (moderate reflectivity values and low vertical developments). In this case, the Mediterranean Sea is demonstrated to play a major role in the efficiency of the precipitation and Convection Initiation (CI), since thunderstorms are mainly initiated over the sea or the coastline, traveling or either to inland or parallel to the shore. This likely corresponds to a convective train effect in multicell or mesoscale systems, where new developing cells are being fed by the stationary cold pool of the preceding ones.

   Flash floods are usually originated upstream, with high precipitation rates that tend to saturate the streams and rivers. Also, the topography favors three main key aspects enhancing the adversity of the storms: it allows the triggering of the convection when the instability is not high enough, it helps in the formation of an instability line over which the thunderstorms grow, and it becomes a capping feature for the cells that get to pass the coastline. For the three analyzed cases, 2018 was the more different one, presenting cells with higher development and different speed and direction. The case was produced by *in situ* rain in the town of Salou.

6. **To identify how to adapt the early warning systems for flash floods in coastal areas for future global warming scenarios:**

   An adapted early warning system is proved to be needed in the coastal area of Salou, and that can be extrapolated to other regions of the Mediterranean with similar characteristics. The system should consider the fast recognition of convective cells since it is found that most are embedded in bigger systems and are short-lived. It should account for the intensity, that can be translated to precipitable water, but also the speed and propagation of the thunderstorms coupled with the topography of the region. It should be able to set different risk levels depending on two main areas; upstream and downstream of the catchment, since they need a differenced precipitation thresholds. Furthermore, the system should be able to release weather warnings if the cells are stationary in the same area for a long time.

7. **To explore the capabilities of an operative regional C-band radar network to retrieve dual-Doppler thunderstorm-scale winds in complex terrain:**

   This and the following objectives are solved in Chapter 9 and is currently being prepared as a manuscript to be published in *Remote Sensing*. This constitutes a pioneering study in a southern European country since is the first time that dual-Doppler retrievals are obtained. It is demonstrated that the geographical configuration of the XRAD, allows retrieving dual-Doppler winds in an area of 13.300 km^2 and 31.040 km^2 for the CDV-PBE and CDV-LMI pairs. This covers most of the area were severe and adverse weather in Catalonia occur, and that is more densely populated. Therefore, it constitutes a powerful tool, since is the first time that a purely dynamical analysis of a thunderstorm is done from observational data. This is achieved using an open-source variational multiple Doppler software, SAMURAI, which is the first time that is used for analyzing severe weather at a thunderstorm scale in complex terrain.

   With the analysis of the tornadic thunderstorm on January 7, 2018, it is demonstrated that SAMURAI constitutes a powerful tool for storm analysis in dramatic situations: a tornado occurring within a valley (radar beam blocking), operational (fixed radar scan mode) and C-band radars (not enough resolution for resolving storm-scale features), and aggressive pre-filtering of radial velocity (loss of half of the mesocyclone in raw data). By using a variational method that includes two different data processing filters (Spline and Gaussian), it has been possible to successfully retrieve the mid-level mesocyclone of the tornadic thunderstorm, as well as the couplet updraft-downdraft associated with the circulation.

8. **To demonstrate the big impact of the topography in the dynamics, propagation, and severity of thunderstorms, and the variability of phenomena in local scales in a case study:**

   The dynamical analysis of the anomalous (weak convective environment) splitting thunderstorm case on 10 July 2013 demonstrates that, contrary to most of the splitting storms reported in the literature that present strong shear in the environmental winds and a primary single cell, the final splitting process here reported is a response of a major system (multicell) interacting with its surrounding conditions, especially the topography. It is the result of enhancement and organization of different cores in the rear flank of a multicell system (cold pool-forced and topographically capped), due to the proximity to a steep orographic ridge, which also enhanced the mid-upper level winds. The splitting process occurred after the organization of the main two cells, which started at high levels, and no initial vertical vorticity couplet was depicted before the split.

10.2 Further considerations and future work

Some further considerations and future actions related to the work accomplished on the present thesis are described below.

The new identification and tracking algorithm:

The new algorithm runs over CAPPI products, as the current operative does. This might lead to think that there's a loss of information of the thunderstorms since it retrieves the cell properties from a derived combined product, instead of the original raw radar data. However, it is important to bear in mind that an identification and tracking algorithm serves as a fast-reliable base tool within a nowcasting system, and that needs to be able to run in real or quasi-real-time. This implies getting the best information in short periods of time, which is achieved with the CAPPI products at the SMC. In the present thesis, it has been pointed out the aggressive pre-processing filtering of the raw radar fields, as well as the complex topography of the territory, both factors that imply a deeper treatment of the raw data if we wanted to introduce it in the nowcasting system. These would add extra time to the operative chain, when, at the moment, it is not demonstrated to improve the final result.

The algorithm proposed in the current thesis is currently being optimized to be used as the operative one at the SMC, going through a pre-operative stage first, when it will be tested in real time and corrected all possible errors. It will be working in combination with the Lightning Jump algorithm from Farnell et al. (2017), as it is the current algorithm, and following the recommendations we added to del Moral et al. (2018b) that lightning data adds valuable data when nowcasting severe thunderstorms; it serves as a proxy for severity giving information of rapid updraft intensification.

Coastal convection

The present research also opens the door to more future work that needs to be done. It is necessary to extend the current work to other risk areas to know if the convective patterns found on the coast of Salou (south of Catalonia) are also found in regions with similar orographic and social configuration, such as the Maresme coast (north of Catalonia). In this sense, the warning system could be extended to the entire coastal region (sensible to future scenarios). Also, the authors consider that future studies should include research on some of the key features that have appeared in this preliminary one: the efficiency of the precipitation, the role of the sea and topography and the motion of the systems. This suggests doing a broad study of the thermodynamic and synoptic and mesoscale conditions of storms affecting the area, which could be done using the new ERA5 reanalysis dataset (from 1979 to within 3 months of real time) and for public use, recently released (Copernicus Climate Change Service, 2017). First, we consider that some of the convective patterns found could be related to warm precipitation (Lin et al., 2001; Liu and Zipser, 2009) and therefore a knowledge of features such as associated lightning and the height of the 0° isotherm would polish the actual convective definition in the area. The latter would help to understand where the melting level is located and therefore the contribution of liquid and/or ice particles in the rain, as well as efficiency. Finally, it would be important to know which has been the main weather type associated with these convective events in the past years, following the work done by Llasat et al. (2005) and Gilabert and Llasat (2018), and how this could change in future scenarios. This would allow computing the impact in low-level winds configuration and sea surface temperature changes and sharpen the future warning systems and adaptation measures. Also, this could confirm the results found previously by Atkinson and Wu Zhang (1996) about shallow convection (cells from 1 to 2 km, with an extension of less than few tens of kilometers), or Kirshbaum and Durran (2004) which investigated how the potential instability, the height of the mountain barrier, the altitude of the unstable layer or the wind shear may affect the development of this type of convection.

The XRAD radar data

Although it is demonstrated that the good geographical configuration of the XRAD has been crucial for the analysis done in this thesis, there still exist some issues that need to be addressed if the Catalan community wants to obtain the most of the radar data (and all the meteorological services that may find themselves in the same situation). During the project, the aggressive operative pre-processing filters have become a real handicap. Although the surveillance operations at the SMC are good, there is so much more that could be obtained if the real raw data was stored. This would not just improve the retrievals when using software like SAMURAI, but also when visually analyzing the data on an operative basis. Also, it would be useful to store the spectral width daily, since it constitutes an important field to take into account when doing wind retrievals quality control or synthesis. Furthermore, there is still unexplored imagery, such as clear air returns, that could give really valuable information when nowcasting convective initiation. Some clear air patterns were hardly seen during the visual analysis of some events, especially in the northeastern region (next to the sea): some gravity waves were visible before the first precipitation echoes appeared, and gave information in advance of possible growing storms. Since the XRAD already has one long-range surveillance sub-task (PPI VOL_A, see Chapter 4), it would be a good opportunity to explore the aforementioned echoes during that volume scan. Getting to know the location and evolution of gravity or mass boundaries occurring in the lower troposphere, can greatly improve the nowcasting results.

Dual-Doppler retrievals with SAMURAI

One of the good things about the way that SAMURAI handles mass continuity is the local application of the constraint rather than via integration of the equation itself. As a result, we can trust the winds above the terrain quite well, since no errors are propagated through the vertical. The software is being currently improved by applying directly the topography in the analysis, which will enhance the retrieved near-surface winds in complex terrain. This is going to be tested soon in the upcoming PRECIP2020 campaign in Taiwan next summer (https://www.eol.ucar.edu/field_projects/precip2020) and we hope that the results will be soon applicable in our region. The SAMURAI algorithm has been demonstrated to be a powerful tool to study our storms, although it is not applicable in real time since it acts as a data assimilation modeling process and requires a high amount of computational time. However, the new LROSE Cyclone version has added the FRACTL (Fast Reorder and CEDRIC Technique in LROSE multi-Doppler retrieval), a traditional multiple Doppler retrieval with integrated interpolation. It adopts the REORDER (Oye and Case, 1995) algorithm to interpolate data to a traditional Cartesian or Cylindrical grid, and the CEDRIC algorithm (Custom Editing and Display of Reduced Information on Cartesian space, NCAR, 1998)) for the analysis, both from NCAR. FRACTL is fast and can solve $\approx$ 3M gates in less than 5 minutes, and therefore, it can be used as a quasi-real-time algorithm. It is important to mention that to use the FRACTL technique, it is needed for the total availability of the original raw radar data since no filtering process is done. Also, the total area of implementation can be compromised because of topography.

The SAMURAI technique has been demonstrated successfully with two inland cases. We plan to consider other events in the coastal areas, where the dynamics can be affected by other factors, such as sea breezes, mesoscale convergence lines, or maritime boundaries and not only by the internal dynamic of the thunderstorms or the interaction with other convective systems and the complex topography. The Mediterranean coast has become a hotspot for heavy rains and severe weather in recent years, and future scenarios demonstrate that the frequency of such events will increase with global warming. There is a current research focus in the Mediterranean basins, especially in densely populated areas, that require concrete action plans and improved early warning systems for future adaptation. The tools presented here and the configuration of the XRAD will allow the Catalan community to further study the convection affecting coastal areas, which may also benefit other risk areas such as Italy or the coast of Greece, where there is not a good radar network configuration to retrieve multiple-Doppler analyses.

Application of WRF model to our study cases

In the past months, it has been also explored the capabilities of high-resolution model WRF simulations (1 km) for real cases in Catalonia. Preliminary results have been obtained by analyzing some of the cases explored with the dual-Doppler retrievals, getting also thermodynamic information. Also, some tests on removing, increasing or decreasing the main topographic features near the thunderstorms are currently being done to see the topographic influence. This is an ongoing project and more future research needs to be done, to know if the changes obtained so far are a product of natural phenomena or noise-related effects within the model itself.

Some personal thoughts...

Finally, and not so related to a scientific point of view, I would like to express some of my concerns about the meteorological community in our country. After being engaged in some international projects with different countries involved, it is clear for me that to move forward in science and achieve our goals, it is needed a sense of community between, especially, the public community (research groups at the universities, weather services, etc.). There is a lot we can learn from our partners and a lot we can achieve together if we concentrate efforts. The political and economic situation in Spain, and in concrete in Catalonia, is from my perspective, affecting our capabilities of achieving that. It constantly feels we are just competing against each other and focusing on personal achievements instead of what took us all to explore this field; how to help our society to live together with what nature is saving for us, and how to adapt to what is coming. In the current climate emergency situation that we are living in, especially in the Mediterranean basin, there is a strong need to build bridges within the community, and walk together to face that future. It is important to credit all the people who are working towards the same purpose, debate with colleagues, exchange our science concerns, and explore new ideas, instead of sitting and watch how slowly we just lose all the achievements that have been done in years of history.

Part V

APPENDIX

APPENDIX A

International research collaborations

During a Ph.D., it is recommended to do a research stay abroad with an international research group to learn other ways of working, other techniques, export and import knowledge, and create professional links with the international community. This doesn't just help in personal and professional growth but also helps the entire community. In this extra chapter of my dissertation, it is briefly presented the field campaigns I have participated in, and my stay in the United States of America. All of these experiences have boosted my professional career and have highly enhanced the thesis that is presented in this manuscript.

I.a Advanced Study Program - NCAR

My international stay has been done at the National Center for Atmospheric Research (NCAR), in the United States, under the excellence grant of the Advanced Study Program for Graduate Visitors. I was granted to visit NCAR for six months, in concrete the Earth Observing Laboratory (EOL), to work with Dr. Tammy Weckwerth on dual-Doppler retrievals and storm dynamics and severity. During all the period I could focus exclusively on my Ph.D. work, acquiring new knowledge and working together with a lot of first-line researchers on radar retrievals and the influence of the topography in the Catalan storms. Although working directly with my mentor Dr.Tammy Weckwerth, I could benefit from the help of a lot of scientists from inside NCAR and universities and research teams in the area, like, for instance, the Atmospheric Science department at Colorado State University (CSU), or the Cooperative Institute for Research in the Atmosphere (CIRA), a joined National Oceanic and Atmospheric Administration (NOAA) and CSU research organism. All the networking and workshops I have participated in during my stay, has led to international collaborations. This is the case, for instance, of the paper we are currently preparing about the last chapter of the dissertation, covering the multiple-Doppler retrieval in the Catalan region (del Moral et al., 2020b),or the submitted paper at the Bulletin of the American Meteorological Society (BAMS) (Rehbein et al., 2020) about the International Satellite Workshop I was granted to participate in, held by CIRA, the National Aeronautics and Space Administration (NASA) and NOAA (Fort Collins, CO, July 2019). Also, it has opened the door to future projects, like the new postdoctoral position I am starting next August at NCAR, in a joined NOAA and NCAR project, under the supervision of Dr. Tammy Weckwerth (Principal Investigator, PI), Dr. Glen Romine and Dr. Dave Turner (Co-PIs): Lower-Tropospheric Thermodynamic and Wind Profiling Impact Study.

I.b RELAMPAGO

In autumn 2018 I had the opportunity to join the intensive operations period of the international field campaign *Remote sensing of Electrification, Lightning, And Mesoscale/microscale Processes with Adaptive Ground Observations*, (RELAMPAGO, `https://sites.google.com/illinois.edu/relampago/home`). It took place from 1 November to 15 December 2018 in Argentina, to study the convective storms producing high impact weather in the vicinity of the Sierras de Córdoba near Córdoba and the Andes foothills near Mendoza. During one month and a half, I joined the Center for Severe Weather Research team (CSWR, `http://cswr.org`) directed by Dr. Joshua Wurman and Dr. Karen Kosiba. The team was in charge of operating the mobile Doppler radars (Doppler on Wheels, DOWs) and the fast deployment instrumentation PODs and mesonet trucks, as well as to launch several soundings during the entire field campaign. The CSWR team (Figure A.1) was formed by about 30 people, starting from the CSWR permanent researchers to collaborators from the U.S., Brazil, Argentina and me, from Spain. Some of the instrumentation we had to work with were the mesonet stations (Figure A.2) and the Portable Observation Devices (PODs, Figure A.3b). A mesonet is a mobile AWS installed on a pick-up truck. On the front side over the hood of the car, there is a mast with anemometers and other wind sensors, and in the trunk, there

Figure A.1: CSWR and collaborators team during the RELAMPAGO field campaign on top of DOW8. Author: Miguel Ottaviano

are the disdrometers (Figure A.3a) and the PODs (Figure A.3b), which are fast deployment field instrumentation. These include sensors to measure velocity and wind direction, humidity, temperature, atmospheric pressure, and size and drop distribution. This instrumentation was usually deployed in the cold pool of severe storms, or outflow/inflow boundaries, to study not just the mature stages of severe convection but also the pre-environment. The other star instruments where the Doppler On Wheels or DOWS. These are mobile doppler radar mounted on trucks. The CSWR has three X-band DOWs (Figure A.4) and a new C-band DOW or COW (Figure A.5). All of them are Doppler, dual-polarimetric and dual-frequency. My experience was mostly with the COW, since I, along with another student from Utah University, were in complete charge of it during the operations (Intensive Operation Practice, IOP). The main physical difference between the DOWS and the COWS is the antenna size since due to working in different wavelengths, the COW needs a bigger diameter. For this reason, the COW was not completely mobile and was deployed in a fixed location during all the field campaign. Due to a smaller attenuation than the DOWs, and a bigger coverage, the COW was strategically deployed in the middle of the region of study, acting as a surveillance radar able to

Figure A.2: Scout or Mesonet with anemometer on the front mast. Author: Anna del Moral

scan from the CI over the Sierras de Córdoba to the MSCs covering the region late at night. Our tasks with the COW were setting-up the radar, changing manually the scanning strategies when the weather was changing, and collecting and reporting all the data. The radar was our particular small laboratory (Figure A.6a) in where we passed days and nights, and in where I got to learn not just dynamics and mesoscale convection, but also electronics and radar hardware management, always coordinated with the Operations Center, with Dr. Kosiba and Dr.Wurman and with all the teams that were out there in the field collecting data (Figure A.6b). Furthermore, I was able to explore the dual-pol capabilities, completely new for me (none of the XRAD radars in Catalonia are dual-polarization), and the southern hemisphere supercell characteristics on organization and motion (Figure A.7). The RELAMPAGO field campaign was a huge international field campaign with first-line PIs and researchers, where I had the opportunity to attend workshops and weather briefings during the campaign. My experience there led me to participate during the spring and summer of 2019 in other field projects with the same team. These are described in the next section.

(a)

(b)

Figure A.3: (a) Parsivel disdrometers and (b) PODs. Author: Anna del Moral

Figure A.4: DOW 8 scanning a supercell during one of the first IOPs. Author: McKenna W. Stanford

Figure A.5: C-band DOW (COW) scanning during a CI mission. Foto: Anna del Moral Author: Anna del Moral

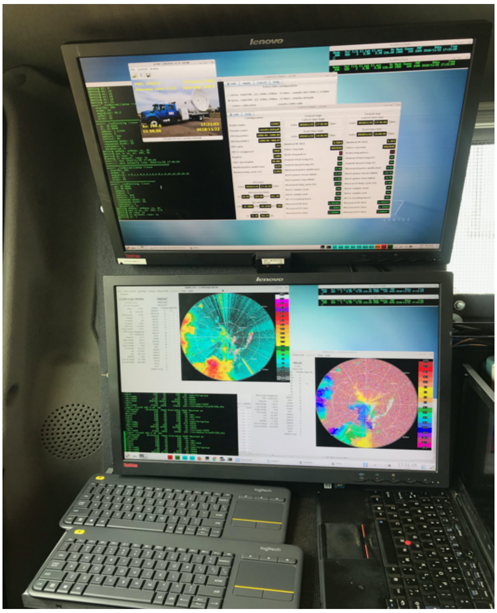

(a)

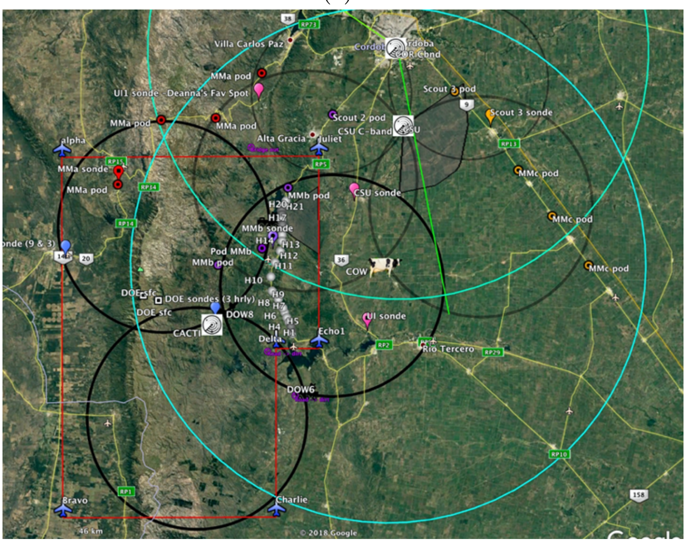

(b)

Figure A.6: (a) COW control monitor during a mission day, visualizing the reflectivity and Doppler velocities. (b) Deployment map of all the teams in RELAMPAGO during an IOP. Author: Karen Kosiba

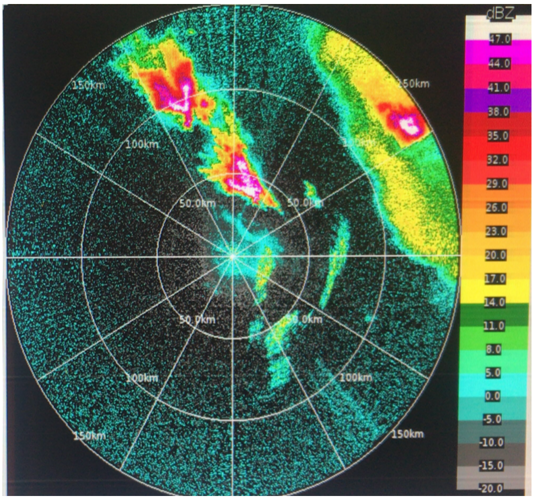

(a)

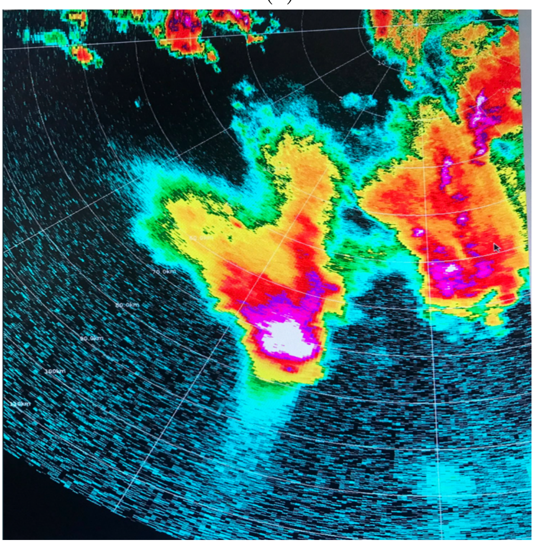

(b)

Figure A.7: (a) Two supercells visible to the south of the COW during IOP 13, in December 2018. The image is rotated 180°. (b) Three Body Scater Spike (TBSS) hail signature in one of the supercells during an overnight IOP on 11 November 2018, scanned from DOW7. Author: Anna del Moral

I.c t-TWIRL and HAL

During the spring and summer of 2019, while in the United States, I collaborated with some of the CSWR field projects, to collect data in severe weather situations. In concrete, in tornados and hurricane environments. On one hand, I participated in a "tiny" 2019 version of the *Tornado Winds from In-situ and Radars at Low-levels* (t-TWIRL) project, during the event on 20 May 2019, a tornado outbreak affecting the Plains in the U.S.A (Figure A.8a, Figure A.8b and Figure A.9). The mission during this event was done with one DOW and two Mesonets, with the main target of deploying PODs into the path of a possible tornado. Although we could not deploy any POD, the DOW could scan closely the Mangum tornado in Oklahoma (EF2), and really valuable radar data was obtained (Figure A.10).

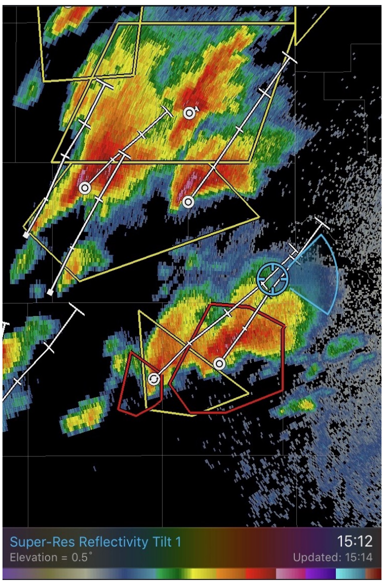

(a)

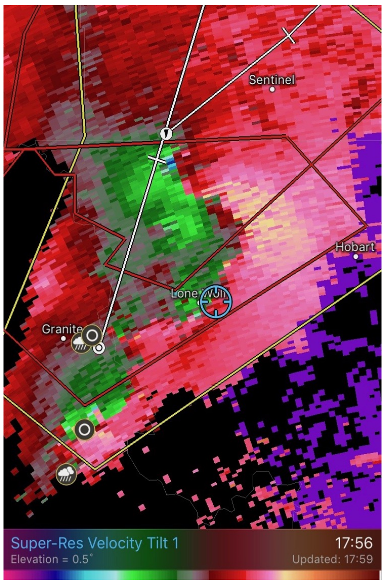

(b)

Figure A.8: (a) Several supercell storms in the 0.5° elevation angle reflectivity field for Frederick radar (KFDR) radar at 15.12 local time, in Oklahoma Panhandle on 20 May, 2019 (RadarScope ©App.).(b) Two tornado-proucing supercells near Mangum and Sentinell in Oklahoma, depicted with the 0.5° radial velocity for Frederick radar (KFDR) on May 20 2019 at 17.56 local time. The blue circle and cone indicate our real-time location and direciton respectively. White dots indicate radar circulations, white lines show the forecasted storm tracks, and yellow and red polygons indicate severe storm warning and tornado warning, respectively. Author: Anna del Moral

On the other hand, during the first week of September in 2019, I participated

Figure A.9: Partial wall cloud from the tornado-producing Sentinell supercell in Figure A.8b at 15.56 local time, seen from the mesonet while on route trying to get position to deploy PODs. Author: Anna del Moral

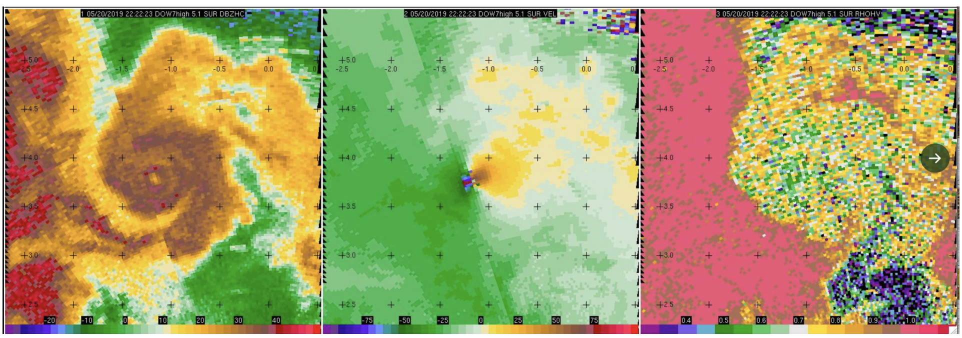

Figure A.10: Mangum, OK, EF2 tornado scanned by DOW7 at 22.22 UTC (17.22 local time) at a distance of $\approx$ 3.7 km. Right, middle and left pannel show reflectivity, radial velocity and copolar correlation coefficient (ρ_{HV}) at 5.1° elevtion angle. The latter is a dual-polarimetric coefficient giving debris information in tornados. Author: Karen Kosiba

in the *Hurricanes At Landfall* (HAL) project, in Stuart, Florida. We drove from Colorado to Florida in a mission with two DOWS and one mesonet to collect data from the CAT 5 hurricane Dorian when doing landfall on the coast of Florida (Figure A.11). The hurricane did not finally do landfall in Florida, since it was stuck for days over the northwest of the Bahamas, destroying everything to its pass. However, we could obtain valuable soundings from the outer bands and the dry slots affecting the coast of Florida, and also DOW7 could scan really good data of the hurricane bands when in front of the coast.

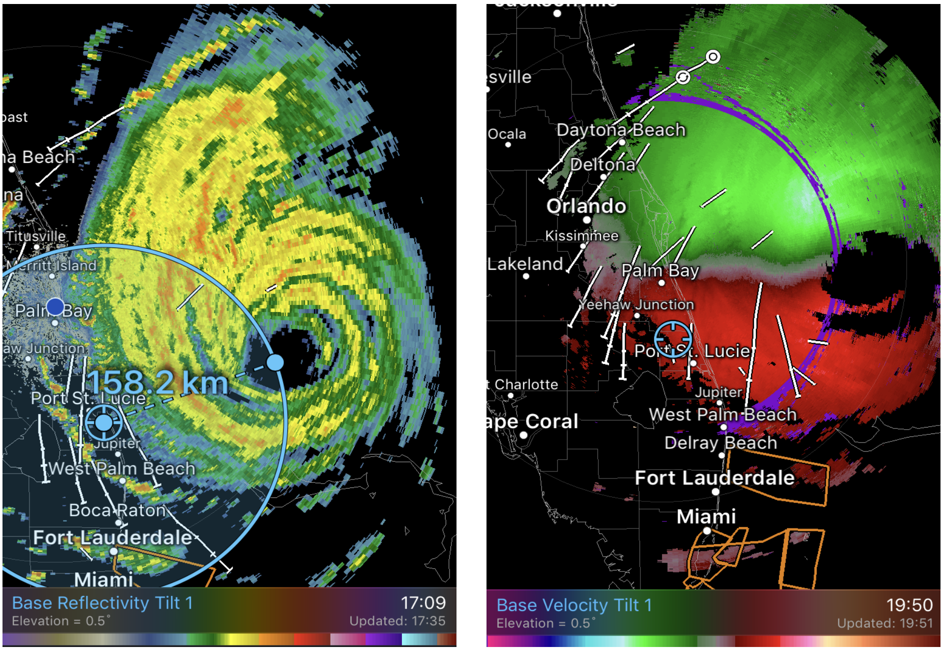

(a) (b)

Figure A.11: (a) Reflectivity field for hurricane Dorian seen from Melbourne radar (KMLB) in FLorida, at a 0.5° elevation angle and at 17.09 local time, on 3 September, 2019 (RadarScope ©App.).(b) Radial velocity for hurricane Dorian seen from the same radar at 19.50 local time. The blue circle and cone indicate our real-time location and direction respectively. White dots indicate radar circulations, white lines show the forecasted storm tracks, and orange polygons indicate severe storm warning. Author: Anna del Moral

Figure A.12: Part of the team launching a sounding in Stuart Beach, Florida, during a hurricane dry slot of the outer band on 3 September 2019. Author: Karen Kosiba

References

ACA, 2019: *Agència Catalana de l'Aigua (ACA)*. Generalitat de Catalunya. Departament de Territori i Sostenibilitat, URL http://agendadelaigua.cat.

Altube, P., 2016: *Procedures for improved weather radar data quality control. Ph.D. Thesis.* Universitat de Barcelona.

Altube, P., J. Bech, O. Argemí, and T. Rigo, 2015: Quality control of antenna alignment and receiver calibration using the sun: Adaptation to midrange weather radar observations at low elevation angles. *Journal of Atmospheric and Oceanic Technology*, **32 (5)**, 927–942.

Altube, P., J. Bech, O. Argemí, T. Rigo, N. Pineda, S. Collis, and J. Helmus, 2017: Correction of dual-PRF Doppler velocity outliers in the presence of aliasing. *Journal of Atmospheric and Oceanic Technology*, **34 (7)**, 1529–1543.

AMS, 2020: *Remote Sensing. Glossary of Meteorology*. American Meteorological Society, URL http://glossary.ametsoc.org/wiki/Remote_sensing.

Aran, M., J. Pena, and M. Torà, 2011: Atmospheric circulation patterns associated with hail events in Lleida (Catalonia). *Atmospheric research*, **100 (4)**, 428–438.

Aran, M., J. C. Peña, N. Pineda, X. Soler, and N. Pérez-Zanón, 2015: Ten-year lightning patterns in Catalonia using Principal Component Analysis.

Armijo, L., 1969: A theory for the determination of wind and precipitation velocities with Doppler radars. *Journal of the Atmospheric Sciences*, **26 (3)**, 570–573.

Atkinson, B., and J. Wu Zhang, 1996: Mesoscale shallow convection in the atmosphere. *Reviews of Geophysics*, **34 (4)**, 403–431.

Ballart, D., F. Figuerola, M. Aran, and T. Rigo, 2009: Analysis of warm convective rain events in Catalonia. *11th Plinius Conference on Mediterranean Storms, September 7-10, 2009 in Barcelona, Spain.*

Barnolas, M., T. Rigo, and M. C. Llasat, 2010: Characteristics of 2D convective structures in Catalonia (NE Spain): an analysis using radar data and GIS. *Hydrology and Earth System Sciences, 2010, vol. 14, p. 129-139.*

Bech, J., J. Arús, S. Castán, N. Pineda, T. Rigo, J. Montanyà, and O. van der Velde, 2015: A study of the 21 March 2012 tornadic quasi linear convective system in Catalonia. *Atmospheric Research*, **158**, 192–209.

Bech, J., R. Pascual, T. Rigo, N. Pineda, J. López, J. Arús, and M. Gayà, 2007: An observational study of the 7 September 2005 Barcelona tornado outbreak. *Natural Hazards & Earth System Sciences*, **7 (1)**.

Bell, M. M., M. T. Montgomery, and K. A. Emanuel, 2012: Air-sea enthalpy and momentum exchange at major hurricane wind speeds observed during cblast. *Journal of the atmospheric sciences*, **69 (11)**, 3197–3222.

Berenguer, M., D. Sempere-Torres, C. Corral, and R. Sánchez-Diezma, 2006: A fuzzy logic technique for identifying nonprecipitating echoes in radar scans. *Journal of Atmospheric and Oceanic Technology*, **23 (9)**, 1157–1180.

Berenguer, M., and I. Zawadzki, 2009: A study of the error covariance matrix of radar rainfall estimates in stratiform rain. Part II. Scale dependence. *Weather and forecasting*, **24 (3)**, 800–811.

Berenguer Ferrer, M., D. Sempere Torres, and M. Hurlimann Ziegler, 2015: Debris-flow forecasting at regional scale by combining susceptibility mapping and radar rainfall. *Natural hazards and earth system sciences*, **15**, 587–602.

Biggerstaff, M. I., and S. A. Listemaa, 2000: An improved scheme for convective/stratiform echo classification using radar reflectivity. *Journal of applied meteorology*, **39 (12)**, 2129–2150.

Bluestein, H. B., and M. H. Jain, 1985: Formation of mesoscale lines of pirecipitation: Severe squall lines in Oklahoma during the spring. *Journal of the Atmospheric Sciences*, **42 (16)**, 1711–1732.

Bodine, D. J., and J. M. Kurdzo, 2018: Ground-Based Radar Technologies for Tornado Observations. *Remote Sensing of Clouds and Precipitation*, Springer, 65–112.

Bonelli, P., and P. Marcacci, 2008: Thunderstorm nowcasting by means of lightning and radar data: algorithms and applications in northern Italy. *Natural Hazards and Earth System Sciences*, **8 (5)**, 1187–1198.

Bousquet, O., and M. Chong, 1998: A multiple-Doppler synthesis and continuity adjustment technique (MUSCAT) to recover wind components from Doppler radar measurements. *Journal of Atmospheric and Oceanic Technology*, **15 (2)**, 343–359.

Bousquet, O., T. Montmerle, and P. Tabary, 2008a: Using operationally synthesized multiple-Doppler winds for high resolution horizontal wind forecast verification. *Geophysical research letters*, **35 (10)**.

Bousquet, O., and P. Tabary, 2014: Development of a nationwide real-time 3-D wind and reflectivity radar composite in France. *Quarterly Journal of the Royal Meteorological Society*, **140 (679)**, 611–625.

Bousquet, O., P. Tabary, and J. Parent du Châtelet, 2007: On the value of operationally synthesized multiple-Doppler wind fields. *Geophysical research letters*, **34 (22)**.

Bousquet, O., P. Tabary, and J. Parent du Châtelet, 2008b: Operational multiple-Doppler wind retrieval inferred from long-range radial velocity measurements. *Journal of applied meteorology and climatology*, **47 (11)**, 2929–2945.

Braud, I., and Coauthors, 2014: Multi-scale hydrometeorological observation and modelling for flash flood understanding. *Hydrology and Earth System Sciences*, **18 (9)**, 3733–3761.

Brovelli, P., S. Sénési, E. Arbogast, P. Cau, S. Cazabat, M. Bouzom, and J. Reynaud, 2005: Nowcasting thunderstorms with Sigoons a significant weather object oriented nowcasting system. *Proceedings of the international symposium on nowcasting and very short range forecasting (WSN05), Toulouse, France.*

Bunkers, M. J., 2002: Vertical wind shear associated with left-moving supercells. *Weather and forecasting*, **17 (4)**, 845–855.

Bunkers, M. J., B. A. Klimowski, J. W. Zeitler, R. L. Thompson, and M. L. Weisman, 2000: Predicting supercell motion using a new hodograph technique. *Weather and forecasting*, **15 (1)**, 61–79.

Byers, H. R., and R. R. Braham, 1949: *The thunderstorm: report of the Thunderstorm Project*. US Government Printing Office.

Carbone, R., M. Carpenter, and C. Burghart, 1985: Doppler radar sampling limitations in convective storms. *Journal of Atmospheric and Oceanic Technology*, **2 (3)**, 357–361.

CCS, 2018: Estadística de riesgos extraordinarios 1971-2017. Tech. rep., Consorcio de Compensación de Seguros.

Ceperuelo, M., M. C. Llasat, L. López, E. García-Ortega, and J. Sánchez, 2006: Study of 11 September 2004 hailstorm event using radar identification of 2-D systems and 3-D cells.

Ceperuelo, M., T. Rigo, M. C. Llasat, and J. L. Sánchez, 2009: Improving hail identification in the Ebro Valley region using radar observations. Probability equations and warning thresholds. *Atmospheric Research*, **93 (1)**, 474 – 482, doi:https://doi.org/10.1016/j.atmosres.2008.09.039, 4th European Conference on Severe Storms.

Chisholm, A., 1972: The kinematics of multicell and supercell Alberta hailstorms. *Alberta Hail Studies, 1972*, 24–31.

Chong, c., M, and Coauthors, 2000: Real-time wind synthesis from Doppler radar observations during the Mesoscale Alpine Programme. *Bulletin of the American Meteorological Society*, **81 (12)**, 2953–2962.

Chong, M., and S. Cosma, 2000: A formulation of the continuity equation of MUSCAT for either flat or complex terrain. *Journal of Atmospheric and Oceanic Technology*, **17 (11)**, 1556–1565.

Copernicus Climate Change Service, C., 2017: *ERA5: Fifth generation of ECMWF atmospheric reanalyses of the global climate*. Copernicus Climate Change Service Climate Data Store, URL https://cds.climate.copernicus.eu/cdsapp#!/home.

Corral, C., M. Berenguer, D. Sempere-Torres, L. Poletti, F. Silvestro, and N. Rebora, 2019: Comparison of two early warning systems for regional flash flood hazard forecasting. *Journal of hydrology*, **572**, 603–619.

Corral, C., D. Velasco, D. Forcadell, D. Sempere-Torres, and E. Velasco, 2009: Advances in radar-based flood warning systems. The EHIMI system and the experience in the Besòs flash-flood pilot basin.

Cortès, M., M. C. Llasat, J. Gilabert, M. Llasat-Botija, M. Turco, R. Marcos, J. P. Martín Vide, and L. Falcón, 2017: Towards a better understanding of the evolution of the flood risk in Mediterranean urban areas: the case of Barcelona. *Natural Hazards*, 1–22, doi:10.1007/s11069-017-3014-0, URL http://link.springer.com/10.1007/s11069-017-3014-0.

Cortès, M., M. Turco, M. Llasat-Botija, and M. C. Llasat, 2018: The relationship between precipitation and insurance data for floods in a Mediterranean region (northeast Spain). *Natural Hazards And Earth System Sciences, 2018, vol. 18, p. 857-868.*

Cotton, W. R., G. Bryan, and S. C. van den Heever, 2011: Mesoscale convective systems. *International Geophysics*, Vol. 99, Elsevier, 455–526.

Cred, C., 2019: Natural disasters in 2018: An opportunity to prepare. Tech. rep., Tech. Rep. 50, 2018.

Cummins, K. L., and M. J. Murphy, 2009: An overview of lightning locating systems: History, techniques, and data uses, with an in-depth look at the US NLDN. *IEEE transactions on electromagnetic compatibility*, **51 (3)**, 499–518.

Davies-Jones, R. P., 1979: Dual-Doppler radar coverage area as a function of measurement accuracy and spatial resolution. *Journal of Applied Meteorology*, **18 (9)**, 1229–1233.

del Moral, A., M. C. Llasat, and T. Rigo, 2017: Identification of anomalous motion of thunderstorms using daily rainfall fields. *Atmospheric Research*, **185**, 92–100.

del Moral, A., M. C. Llasat, and T. Rigo, 2020a: Connecting flash flood events with radar-derived convective storm characteristics on the Northwestern Mediterranean coast: Knowing the present for better future scenarios adaptation. *Atmospheric Research*, **238**, 104–863.

del Moral, A., T. Rigo, and M. C. Llasat, 2018a: Performance of a new algorithm for nowcasting anomalous trajectories. *Proceedings fo the 10th European Conference on Radar in Meteorology and Hydrology (ERAD 2018): 1-6 July 2018, Ede-Wageningen, The Netherlands.*

del Moral, A., T. Rigo, and M. C. Llasat, 2018b: A radar-based centroid tracking algorithm for severe weather surveillance: Identifying split/merge processes in convective systems. *Atmospheric Research*, **213**, 110–120.

del Moral, A., T. M. Weckwerth, T. Rigo, M. M. Bell, and M. C. Llasat, 2020b: C-band dual-Doppler retrievals in complex terrain: Improving the knowledge of severe storm dynamics in Catalonia. *Remote Sensing*, in preparation.

Dennis, E. J., and M. R. Kumjian, 2017: The impact of vertical wind shear on hail growth in simulated supercells. *Journal of the Atmospheric Sciences*, **74 (3)**, 641–663.

Dixon, M., and G. Wiener, 1993: TITAN: Thunderstorm identification, tracking, analysis, and nowcasting: A radar-based methodology. *Journal of atmospheric and oceanic technology*, **10 (6)**, 785–797.

Dolan, B. A., and S. A. Rutledge, 2007: An integrated display and analysis methodology for multivariable radar data. *Journal of applied meteorology and climatology*, **46 (8)**, 1196–1213.

Doswell, C. A., 2001: Severe convective storms: An overview. *Severe convective storms*, Springer, 1–26.

Doswell III, C. A., 1985: The Operational Meteorology of Convective Weather. Volume 2. Storm Scale Analysis. Tech. rep., AIR WEATHER SERVICE SCOTT AFB IL.

Doswell III, C. A., H. E. Brooks, and R. A. Maddox, 1996: Flash flood forecasting: An ingredients-based methodology. *Weather and Forecasting*, **11 (4)**, 560–581.

Doviak, R. J., P. S. Ray, R. G. Strauch, and L. J. Miller, 1976: Error estimation in wind fields derived from dual-Doppler radar measurement. *Journal of Applied Meteorology*, **15 (8)**, 868–878.

Doviak, R. J., and D. S. Zrnic, 2014: *Doppler Radar and Weather Observations*. Academic Press.

Eurostat, 2016: Eurostat regional yearbook. Tech. rep. URL http://ec.europa.eu/eurostat/statistics-explained/index.php/Regional_yearbook_introduction.

Fabry, F., 2015: *Radar meteorology: principles and practice*. Cambridge University Press.

Farnell, C., 2018: *Anàlisi, diagnosi i predicció d'episodis severs a Catalunya. Focalització en les pedregades del Pla de Lleida. Ph.D. Thesis*. Universitat de Barcelona.

Farnell, C., and M. C. Llasat, 2013: Proposal of three thermodynamic variables to discriminate between storms associated with hail and storms with intense rainfall in Catalonia (Proposta de tres variables termodinàmiques per discriminar entre tempestes amb pedregades i tempestes amb pluges intenses). *Tethys: Journal of Mediterranean Meteorology & Climatology, 2013, vol. 10, p. 25-34*.

Farnell, C., T. Rigo, and N. Pineda, 2017: Lightning jump as a nowcast predictor: Application to severe weather events in Catalonia. *Atmospheric Research*, **183**, 130–141, doi:10.1016/j.atmosres.2016.08.021.

Fiori, E., A. Comellas, L. Molini, N. Rebora, F. Siccardi, D. Gochis, S. Tanelli, and A. Parodi, 2014: Analysis and hindcast simulations of an extreme rainfall event in the Mediterranean area: The Genoa 2011 case. *Atmospheric Research*, **138**, 13–29.

Foerster, A. M., and M. M. Bell, 2017: Thermodynamic retrieval in rapidly rotating vortices from multiple-Doppler radar data. *Journal of Atmospheric and Oceanic Technology*, **34 (11)**, 2353–2374.

Foerster, A. M., M. M. Bell, P. A. Harr, and S. C. Jones, 2014: Observations of the eyewall structure of Typhoon Sinlaku (2008) during the transformation stage of extratropical transition. *Monthly Weather Review*, **142 (9)**, 3372–3392.

Frame, J., P. Markowski, Y. Richardson, J. Straka, and J. Wurman, 2009: Polarimetric and dual-Doppler radar observations of the Lipscomb County, Texas, supercell thunderstorm on 23 May 2002. *Monthly weather review*, **137 (2)**, 544–561.

Friedrich, K., and M. Hagen, 2004: On the use of advanced Doppler radar techniques to determine horizontal wind fields for operational weather surveillance. *Meteorological Applications*, **11 (2)**, 155–171.

Fujita, T. T., 1981: Tornadoes and downbursts in the context of generalized planetary scales. *Journal of the Atmospheric Sciences*, **38 (8)**, 1511–1534.

Gao, J., M. Xue, K. Brewster, and K. K. Droegemeier, 2004: A three-dimensional variational data analysis method with recursive filter for Doppler radars. *Journal of Atmospheric and oceanic technology*, **21 (3)**, 457–469.

Gaume, E., M. Borga, M. C. Llassat, S. Maouche, M. Lang, and M. Diakakis, 2016: Mediterranean extreme floods and flash floods.

Gayà, M., M. C. Llasat, and J. Arús Dumenjó, 2011: Tornadoes and waterspouts in Catalonia (1950-2009). *Natural Hazards and Earth System Sciences, 2011, Vol. 11, p. 1875-1883.*

Geerts, B., and Coauthors, 2017: The 2015 plains elevated convection at night field project. *Bulletin of the American Meteorological Society*, **98 (4)**, 767–786.

Gilabert, J., and M. C. Llasat, 2018: Circulation weather types associated with extreme flood events in Northwestern Mediterranean. *International Journal of Climatology*, **38 (4)**, 1864–1876.

Godart, A., S. Anquetin, E. Leblois, and J.-D. Creutin, 2011: The contribution of orographically driven banded precipitation to the rainfall climatology of a Mediterranean region. *Journal of applied meteorology and climatology*, **50 (11)**, 2235–2246.

Grasmick, C., B. Geerts, D. D. Turner, Z. Wang, and T. Weckwerth, 2018: The relation between nocturnal MCS evolution and its outflow boundaries in the stable boundary layer: An observational study of the 15 July 2015 MCS in PECAN. *Monthly Weather Review*, **146 (10)**, 3203–3226.

Han, L., S. Fu, L. Zhao, Y. Zheng, H. Wang, and Y. Lin, 2009: 3D convective storm identification, tracking, and forecasting: An enhanced TITAN algorithm. *Journal of Atmospheric and Oceanic Technology*, **26 (4)**, 719–732.

Hering, A., C. Morel, G. Galli, S. Sénési, P. Ambrosetti, and M. Boscacci, 2004: Nowcasting thunderstorms in the Alpine region using a radar based adaptive thresholding scheme. *Proceedings of ERAD*, Vol. 1.

Holleman, I., and H. Beekhuis, 2003: Analysis and correction of dual PRF velocity data. *Journal of Atmospheric and Oceanic Technology*, **20 (4)**, 443–453.

Homar, V., M. Gaya, R. Romero, C. Ramis, and S. Alonso, 2003: Tornadoes over complex terrain: An analysis of the 28th August 1999 tornadic event in eastern Spain. *Atmospheric research*, **67**, 301–317.

Houston, A. L., B. Argrow, M. C. Coniglio, E. W. Frew, E. N. Rasmussen, C. C. Weiss, and C. L. Ziegler, 2020: Targeted Observation by Radars and UAS of Supercells (TORUS): Summary of the 2019 field campaign. *100th American Meteorological Society Annual Meeting*, AMS.

Houston, A. L., and R. B. Wilhelmson, 2007: Observational analysis of the 27 May 1997 central Texas tornadic event. Part I: Prestorm environment and storm maintenance/propagation. *Monthly weather review*, **135 (3)**, 701–726.

Houze Jr, R. A., 2018: 100 years of research on mesoscale convective systems. *Meteorological Monographs*, **59**, 17–1.

Hu, J., and Coauthors, 2019: Tracking and characterization of convective cells through their maturation into stratiform storm elements using polarimetric radar and lightning detection. *Atmospheric research*, **226**, 192–207.

Keeler, R. J., J. Lutz, and J. Vivekanandan, 2000: S-Pol: NCAR's polarimetric Doppler research radar. *IGARSS 2000. IEEE 2000 International Geoscience and Remote Sensing Symposium. Taking the Pulse of the Planet: The Role of Remote Sensing in Managing the Environment. Proceedings (Cat. No. 00CH37120)*, IEEE, Vol. 4, 1570–1573.

Kessler, E., 1966: Computer program for calculating average lengths of weather radar echoes and pattern bandedness. *Journal of the Atmospheric Sciences*, **23 (5)**, 569–574.

Kiktev, D., and Coauthors, 2017: FROST-2014. The Sochi winter olympics international project. *Bulletin of the American Meteorological Society*, **98 (9)**, 1908–1929.

Kirshbaum, D. J., and D. R. Durran, 2004: Factors governing cellular convection in orographic precipitation. *Journal of the atmospheric Sciences*, **61 (6)**, 682–698.

Klemp, J. B., and R. B. Wilhelmson, 1978: The simulation of three-dimensional convective storm dynamics. *Journal of the Atmospheric Sciences*, **35 (6)**, 1070–1096.

Kosiba, K. A., and J. Wurman, 2014: Finescale dual-Doppler analysis of hurricane boundary layer structures in Hurricane Frances (2004) at landfall. *Monthly Weather Review*, **142 (5)**, 1874–1891.

Kumjian, M. R., and A. V. Ryzhkov, 2008: Polarimetric signatures in supercell thunderstorms. *Journal of applied meteorology and climatology*, **47 (7)**, 1940–1961.

Lemon, L. R., and C. A. Doswell III, 1979: Severe thunderstorm evolution and mesocyclone structure as related to tornadogenesis. *Monthly Weather Review*, **107 (9)**, 1184–1197.

Lhermitt, R., and L. Miller, 1970: Doppler Radar Methodology for Observation of Convective Storms. *Bulleting of the American Meteorological Society*, American Meteorological Society, Vol. 51, 772.

Li, H.-J., and Y.-W. Kiang, 2005: Radar and Inverse Scattering. *The Electrical Engineering Handbook*, W.-K. Chen, Ed., Academic Press, Burlington, 671 – 690, doi:https://doi.org/10.1016/B978-012170960-0/50047-5, URL http://www.sciencedirect.com/science/article/pii/B9780121709600500475.

Ligda, M. G., 1953: *Horizontal Motion of Small Precipitation Areas as Observed by Radar. Tech. Rep. 21*. Department of Meteorology, M.I.T.

Lin, Y.-L., S. Chiao, T.-A. Wang, M. L. Kaplan, and R. P. Weglarz, 2001: Some common ingredients for heavy orographic rainfall. *Weather and forecasting*, **16 (6)**, 633–660.

Lin, Y.-L., R. L. Deal, and M. S. Kulie, 1998: Mechanisms of cell regeneration, development, and propagation within a two-dimensional multicell storm. *Journal of the atmospheric sciences*, **55 (10)**, 1867–1886.

Liu, C., and E. J. Zipser, 2009: "Warm rain" in the tropics: Seasonal and regional distributions based on 9 yr of TRMM data. *Journal of climate*, **22 (3)**, 767–779.

Llabrés-Brustenga, A., A. Rius, R. Rodríguez-Solà, M. C. Casas-Castillo, and A. Redaño, 2019: Quality control process of the daily rainfall series available in Catalonia from 1855 to the present. *Theoretical and Applied Climatology*, **137 (3-4)**, 2715–2729.

Llasat, M. C., 2001: An objective classification of rainfall events on the basis of their convective features: application to rainfall intensity in the northeast of Spain. *International Journal of Climatology: A Journal of the Royal Meteorological Society*, **21 (11)**, 1385–1400.

Llasat, M. C., 2009: High magnitude storms and floods. *The Physical Geography of the Mediterranean, edited by: Woodward, JC, Oxford University Press, Oxford*, 513–540.

Llasat, M. C., M. Barriendos, A. Barrera, and T. Rigo, 2005: Floods in Catalonia (NE Spain) since the 14th century. Climatological and meteorological aspects from historical documentary sources and old instrumental records. *Journal of Hydrology*, **313 (1-2)**, 32–47.

Llasat, M. C., M. Ceperuelo, and T. Rigo, 2007: Rainfall regionalization on the basis of the precipitation convective features using a raingauge network and weather radar observations. *Atmospheric research*, **83 (2-4)**, 415–426.

Llasat, M. C., M. Llasat-Botija, A. Rodriguez, and S. Lindbergh, 2010: Flash floods in Catalonia: a recurrent situation. *Advances in Geosciences*, **26**, 105–111.

Llasat, M. C., R. Marcos, M. Llasat-Botija, J. Gilabert, M. Turco, and P. Quintana-Seguí, 2014: Flash flood evolution in north-western Mediterranean. *Atmospheric Research*, **149**, 230–243.

Llasat, M. C., R. Marcos, M. Turco, J. Gilabert, and M. Llasat-Botija, 2016: Trends in flash flood events versus convective precipitation in the Mediterranean region: The case of Catalonia. *Journal of Hydrology*, **541**, 24–37, doi:10.1016/j.jhydrol.2016.05.040.

Llasat, M. C., T. Rigo, and M. Barriendos, 2003: The 'Montserrat-2000' flash-flood event: a comparison with the floods that have occurred in the northeastern Iberian Peninsula since the 14th century. *International Journal of Climatology: A Journal of the Royal Meteorological Society*, **23 (4)**, 453–469.

Lloyd, C., 2010: *Spatial data analysis: an introduction for GIS users*. Oxford university press.

López, L., E. García-Ortega, B. Gil, and J. Sánchez, 2008: The Multicellular Hailstorm on 19 July 2006 in Maluenda (Ebro Valley, Spain). *Fifth European Conference on Radar in Meteorology and Hydrology. Helsinki, Finland.*

López, L., and J. Sánchez, 2009: Discriminant methods for radar detection of hail. *Atmospheric Research*, **93 (1-3)**, 358–368.

LROSE Development Team, 2019: *LROSE: Lidar Radar Open Source Environment*. National Science Foundation, URL https://www.http://lrose.net/index.html.

Markowski, P., C. Hannon, J. Frame, E. Lancaster, A. Pietrycha, R. Edwards, and R. L. Thompson, 2003: Characteristics of vertical wind profiles near supercells obtained from the Rapid Update Cycle. *Weather and forecasting*, **18 (6)**, 1262–1272.

Markowski, P., and Y. Richardson, 2011: *Mesoscale meteorology in midlatitudes*, Vol. 2. John Wiley & Sons.

Marquis, J., Y. Richardson, J. Wurman, and P. Markowski, 2008: Single-and dual-Doppler analysis of a tornadic vortex and surrounding storm-scale flow in the Crowell, Texas, supercell of 30 April 2000. *Monthly Weather Review*, **136 (12)**, 5017–5043.

Marshall, J. S., and W. M. K. Palmer, 1948: The distribution of raindrops with size. *Journal of meteorology*, **5 (4)**, 165–166.

Martín, F., O. Carretero, and F. Elizaga, 2001: Lightning and radar data observations of convective perturbations in the western Mediterranean areas. *Proceedings of 3rd EGS Plinius Conference in Baja Sardinia, Italy, GNDCI pub*, 1–3.

Martín, F., O. Carretero, I. San Ambrosio, and F. Elizaga, 2002: Identification and analysis of a supercell storm in the Mediterranean area from radar-based perspective. *Proceedings of European Conference on Severe Storms in Praga*.

Martín, F., F. Elizaga, O. Carretero, and I. San Ambrosio, 2007: *Diagnóstico y predicción de la convección profunda (in Spanish). In: Technical Note n. 35 of the Analysis and Forecasting Technical Service of the Spanish Weather Service.*

Martín, J. R., M. M. García, F. De, P. Dávila, and L. R. Soriano, 2014: Regimes of intense precipitation in the Spanish Mediterranean area. *Atmospheric Research*, **137**, 66–79, doi:10.1016/j.atmosres.2013.09.010.

May, P. T., 2001: Mesocyclone and microburst signature distortion with dual PRT radars. *Journal of Atmospheric and Oceanic Technology*, **18 (7)**, 1229–1233.

May, P. T., and A. Ballinger, 2007: The statistical characteristics of convective cells in a monsoon regime (Darwin, Northern Australia). *Monthly weather review*, **135 (1)**, 82–92.

Mazur, V., W. D. Rust, and J. C. Gerlach, 1986: Evolution of lightning flash density and reflectivity structure in a multicell thunderstorm. *Journal of Geophysical Research: Atmospheres*, **91 (D8)**, 8690–8700.

McDonald, J. R., K. C. Mehta, D. A. Smith, and J. A. Womble, 2010: The enhanced fujita scale: development and implementation. *Forensic Engineering 2009: Pathology of the Built Environment*, 719–728.

Meischner, P., 2005: *Weather radar: principles and advanced applications*. Springer Science & Business Media.

Miller, L., and R. Kropfli, 1980: Part II: Experimental Design and Procedures. *Bulletin of the American Meteorological Society*, **61**, 1173–1177.

Miller, L., and R. Strauch, 1974: A dual Doppler radar method for the determination of wind velocities within precipitating weather systems. *Remote Sensing of Environment*, **3 (4)**, 219–235.

Miller, P. W., and T. L. Mote, 2017: Standardizing the definition of a 'pulse' thunderstorm. *Bulletin of the American Meteorological Society*, **98 (5)**, 905–913.

Mulholland, J. P., S. W. Nesbitt, and R. J. Trapp, 2019: A Case Study of Terrain Influences on Upscale Convective Growth of a Supercell. *Monthly Weather Review*, **147 (12)**, 4305–4324.

NCAR, 1998: *CEDRIC. Custom Editing and Display of Reduced Information in Cartesian space*. National Center for Atmospheric Research.

Nesbitt, S. W., P. V. Salio, A. Varble, R. J. Trapp, R. R. Roberts, F. Dominguez, L. Machado, and C. Saulo, 2017: Improving high impact weather and climate prediction for societal resilience in Subtropical South America: Proyecto RELAMPAGO-CACTI. *Agu fall meeting abstracts*.

Novák, P., L. Březková, and P. Frolík, 2009: Quantitative precipitation forecast using radar echo extrapolation. *Atmospheric research*, **93 (1-3)**, 328–334.

Ooyama, K. V., 1987: Scale-controlled objective analysis. *Monthly Weather Review*, **115 (10)**, 2479–2506.

Ooyama, K. V., 2002: The cubic-spline transform method: Basic definitions and tests in a 1d single domain. *Monthly weather review*, **130 (10)**, 2392–2415.

Oye, D., and M. Case, 1995: *REORDER. A Program for Gridding Radar Data, Installation and Use Manual for the Unixe Version*. National Center for Atmospheric Research.

Oye, R., C. Mueller, and S. Smith, 1995: Software for radar translation, visualization, editing, and interpolation. *Preprints, 27th Conf. on Radar Meteorology, Vail, CO, Amer. Meteor. Soc*, 359–361.

Panagos, P., and Coauthors, 2015: Rainfall erosivity in Europe. *Science of the Total Environment*, **511**, 801–814.

Panziera, L., and U. Germann, 2010: The relation between airflow and orographic precipitation on the southern side of the Alps as revealed by weather radar. *Quarterly Journal of the Royal Meteorological Society: A journal of the atmospheric sciences, applied meteorology and physical oceanography*, **136 (646)**, 222–238.

Papadimitriou, C. H., and K. Steiglitz, 1998: *Combinatorial optimization: algorithms and complexity*. Courier Corporation.

Papagiannaki, K., K. Lagouvardos, V. Kotroni, and A. Bezes, 2015: Flash flood occurrence and relation to the rainfall hazard in a highly urbanized area. *Natural Hazards & Earth System Sciences*, **15 (8)**.

Parker, M. D., and R. H. Johnson, 2000: Organizational modes of midlatitude mesoscale convective systems. *Monthly weather review*, **128 (10)**, 3413–3436.

Pastor, F., J. A. Valiente, and M. Estrela, 2015: Sea surface temperature and torrential rains in the Valencia region: modelling the role of recharge areas. *Natural Hazards & Earth System Sciences Discussions*, **3 (2)**.

Peleg, N., and E. Morin, 2012: Convective rain cells: Radar-derived spatiotemporal characteristics and synoptic patterns over the eastern Mediterranean. *Journal of Geophysical Research: Atmospheres*, **117 (D15)**.

Pereira, L. G., and S. A. Rutledge, 2006: Diurnal cycle of shallow and deep convection for a tropical land and an ocean environment and its relationship to synoptic wind regimes. *Monthly weather review*, **134 (10)**, 2688–2701.

Peters, J. M., E. R. Nielsen, M. D. Parker, S. M. Hitchcock, and R. S. Schumacher, 2017: The impact of low-level moisture errors on model forecasts of an MCS observed during PECAN. *Monthly Weather Review*, **145 (9)**, 3599–3624.

Petrucci, O., and Coauthors, 2019: Flood fatalities in Europe, 1980–2018: Variability, features, and lessons to learn. *Water*, **11 (8)**, 1682.

Pineda, N., M. Aran, A. Andres, M. Busto, C. Farnell, and M. Torà, 2009: Study of the September 17th 2007 severe hailstorm in Pla d'Urgell. *Part II: meteorological analysis, Tethys*, **6**, 83–103.

Pineda, N., and T. Rigo, 2017: The rainfall factor in lightning-ignited wildfires in Catalonia. *Agricultural and Forest Meteorology*, **239**, 249–263.

Pineda, N., T. Rigo, J. Bech, and X. Soler, 2007: Lightning and precipitation relationship in summer thunderstorms: Case studies in the North Western Mediterranean region. *Atmospheric research*, **85 (2)**, 159–170.

Pineda, N., S. T. Soler, and E. Vilaclara, 2011: *Aproximació a la climatologia de llamps a Catalunya: anàlisi de les dades de l'SMC per al període 2004-2008*. Generalitat de Catalunya, Departament de Territori i Sostenibilitat.

Potvin, C. K., L. J. Wicker, and A. Shapiro, 2012: Assessing errors in variational dual-Doppler wind syntheses of supercell thunderstorms observed by storm-scale mobile radars. *Journal of Atmospheric and Oceanic Technology*, **29 (8)**, 1009–1025.

Preparata, F. P., and M. I. Shamos, 2012: *Computational geometry: an introduction*. Springer Science & Business Media.

Price, C., and Coauthors, 2011: Using lightning data to better understand and predict flash floods in the Mediterranean. *Surveys in geophysics*, **32 (6)**, 733.

Probert-Jones, J., 1962: The radar equation in meteorology. *Quarterly Journal of the Royal Meteorological Society*, **88 (378)**, 485–495.

Purser, R. J., W.-S. Wu, D. F. Parrish, and N. M. Roberts, 2003: Numerical aspects of the application of recursive filters to variational statistical analysis. Part I: Spatially homogeneous and isotropic Gaussian covariances. *Monthly Weather Review*, **131 (8)**.

Python Core Team, 2001: *Python Language Reference*. Python Software Foundation, URL https://www.python.org/.

QGIS Development Team, 2009: *QGIS Geographic Information System*. Open Source Geospatial Foundation, URL http://qgis.org.

R Core Team, 2019: *R: A Language and Environment for Statistical Computing*. R Foundation for Statistical Computing, URL https://www.R-project.org/.

Ramis, C., J. M. López, and J. Arús, 1999: Two cases of severe weather in Catalonia (Spain). A diagnostic study. *Meteorological Applications*, **6 (1)**, 11–27.

Rasmussen, C., and G. D. Hager, 2001: Probabilistic data association methods for tracking complex visual objects. *IEEE Transactions on Pattern Analysis and Machine Intelligence*, **23 (6)**, 560–576.

Rauber, R. M., and S. L. Nesbitt, 2018: *Radar Meteorology: A First Course*. John Wiley & Sons.

Ray, P. S., and K. L. Sangren, 1983: Multiple-Doppler radar network design. *Journal of climate and applied meteorology*, **22 (8)**, 1444–1454.

Ray, P. S., and K. K. Wagner, 1976: Multiple Doppler radar observations of storms. *Geophysical Research Letters*, **3 (3)**, 189–191.

Rehbein, A., M. Rugna, M. P. Hobouchian, A. del Moral, S. J. Goodman, D. T. Lindsey, and J. Thomas, 2020: A Workshop on the Next Generation Environmental Satellite Constellation. *Bulletin of the American Meteorological Society*, submitted and Under Review.

Rigo, T., M. Aran, J. Bech, C. Farnell, J. Mateo, N. Pineda, R. Ripoll, and A. Serra, 2015: Discriminating downburst-producing and hail-bearing thunderstorms using total lightning and weather radar observations. *In proceedings in the 8th European Conference on Severe Storms,ECCS*.

Rigo, T., M. Berenguer, and M. C. Llasat, 2019: An improved analysis of mesoscale convective systems in the western Mediterranean using weather radar. *Atmospheric research*, **227**, 147–156.

Rigo, T., and M. C. Llasat, 2002: Analysis of convective structures that produce heavy rainfall events in Catalonia (NE of Spain), using meteorological radar. *Proceeding of ERAD*, 45–48.

Rigo, T., and M. C. Llasat, 2004: A methodology for the classification of convective structures using meteorological radar: Application to heavy rainfall events on the Mediterranean coast of the Iberian Peninsula. *Natural Hazards and Earth System Sciences*, 59–68.

Rigo, T., and M. C. Llasat, 2005: Radar analysis of the life cycle of Mesoscale Convective Systems during the 10 June 2000 event. *Natural Hazards and Earth System Sciences*, **5**, 959–970.

Rigo, T., and M. C. Llasat, 2007: Analysis of mesoscale convective systems in Catalonia using meteorological radar for the period 1996–2000. *Atmospheric Research*, **83 (2-4)**, 458–472.

Rigo, T., and M. C. Llasat, 2016: Forecasting hailfall using parameters for convective cells identified by radar. *Atmospheric Research*, **169**, 366–376.

Rigo, T., and N. Pineda, 2016: Inferring the severity of a multicell thunderstorm evolving to supercell, by means of radar and total lightning. *E-Journal of Severe Storms Meteorology*, **11 (2)**.

Rigo, T., N. Pineda, and J. Bech, 2010: Analysis of warm season thunderstorms using an object-oriented tracking method based on radar and total lightning data. *Natural Hazards and Earth System Sciences*, 1881–1893.

Rinehart, R., 1981: A pattern recognition technique for use with conventional weather radar to determine internal storm motions. *Atmos. Technol*, **13**, 119–134.

Roberts, R. D., D. Burgess, and M. Meister, 2006: Developing tools for nowcasting storm severity. *Weather and forecasting*, **21 (4)**, 540–558.

Rodríguez, O., and J. Bech, 2018: Sounding-derived parameters associated with tornadic storms in Catalonia. *International Journal of Climatology*, **38 (5)**, 2400–2414.

Rotunno, R., and R. Ferretti, 2003: Orographic effects on rainfall in MAP cases IOP 2b and IOP 8. *Quarterly Journal of the Royal Meteorological Society: A journal of the atmospheric sciences, applied meteorology and physical oceanography*, **129 (588)**, 373–390.

Rotunno, R., and J. Klemp, 1985: On the rotation and propagation of simulated supercell thunderstorms. *Journal of the Atmospheric Sciences*, **42 (3)**, 271–292.

Sánchez-Diezma, R., D. Sempere-Torres, J. Bech, and E. Velasco, 2002: Developement of a hydrometeorological flood warning system (EHIMI) based on radar data. *Second European Conference on Radar Meteorology (ERAD), Delft, Netherlands.*

Schmidt, J. M., and Coauthors, 2019: Radar Detection of Individual Raindrops. *Bulletin of the American Meteorological Society*, **(2019)**.

Schultz, C. J., W. A. Petersen, and L. D. Carey, 2009: Preliminary development and evaluation of lightning jump algorithms for the real-time detection of severe weather. *Journal of Applied Meteorology and Climatology*, **48 (12)**, 2543–2563.

Schumacher, C., and R. A. Houze Jr, 2003: The TRMM precipitation radar's view of shallow, isolated rain. *Journal of Applied Meteorology*, **42 (10)**, 1519–1524.

Schumacher, R. S., and R. H. Johnson, 2005: Organization and environmental properties of extreme-rain-producing mesoscale convective systems. *Monthly weather review*, **133 (4)**, 961–976.

Schuster, S. S., R. J. Blong, and M. S. Speer, 2005: A hail climatology of the greater Sydney area and New South Wales, Australia. *International Journal of Climatology: A Journal of the Royal Meteorological Society*, **25 (12)**, 1633–1650.

Seifoddini, H., and M. Djassemi, 1991: The production data-based similarity coefficient versus jaccard's similarity coefficient. *Computers & industrial engineering*, **21 (1-4)**, 263–266.

Sempere-Torres, D., M. Berenguer, and S. Park, 2016: From Rainfall Nowcasting to Flash Flood Early Warning Systems: recent and ongoing advancements in Europe. *AGU Fall Meeting Abstracts*.

Senf, F., F. Dietzsch, A. Hünerbein, and H. Deneke, 2015: Characterization of initiation and growth of selected severe convective storms over central Europe with MSG-SEVIRI. *Journal of Applied Meteorology and Climatology*, **54 (1)**, 207–224.

Shi, J., P. Wang, D. Wang, and H. Jia, 2019: Radar-Based Automatic Identification and Quantification of Weak Echo Regions for Hail Nowcasting. *Atmosphere*, **10 (6)**, 325.

Short, D. A., and K. Nakamura, 2000: TRMM radar observations of shallow precipitation over the tropical oceans. *Journal of Climate*, **13 (23)**, 4107–4124.

Skamarock, W. C., J. B. Klemp, J. Dudhia, D. O. Gill, D. M. Barker, W. Wang, and J. G. Powers, 2008: *A description of the Advanced Research WRF version 3. NCAR Technical note-475+ STR*.

Sui, C.-H., X. Li, and M.-J. Yang, 2007: On the definition of precipitation efficiency. *Journal of the Atmospheric Sciences*, **64 (12)**, 4506–4513.

Tessendorf, S. A., and Coauthors, 2019: A transformational approach to winter orographic weather modification research: The SNOWIE Project. *Bulletin of the American Meteorological Society*, **100 (1)**, 71–92.

Trapero, L., J. Bech, T. Rigo, N. Pineda, and D. Forcadell, 2009: Uncertainty of precipitation estimates in convective events by the Meteorological Service of Catalonia radar network. *Atmospheric research*, **93 (1-3)**, 408–418.

Trentmann, J., and Coauthors, 2009: Multi-model simulations of a convective situation in low-mountain terrain in central Europe. *Meteorology and atmospheric physics*, **103 (1-4)**, 95–103.

Tsonis, A., and G. Austin, 1981: An evaluation of extrapolation techniques for the short-term predicton of rain amounts. *Atmosphere-Ocean*, **19**, 54–65, URL http://www.tandfonline.com/action/journalInformation?journalCode=tato20.

Tuovinen, J.-P., A.-J. Punkka, J. Rauhala, H. Hohti, and D. M. Schultz, 2009: Climatology of severe hail in Finland: 1930–2006. *Monthly Weather Review*, **137 (7)**, 2238–2249.

Vaisala, 2014a: *Suncal utility: UTILITIES MANUAL: IRIS and RDA, Chap. 11*. Helsinki, Finland, Vaisala Oyj.

Vaisala, 2014b: *USER'S MANUAL: Digital IF receiver/Doppler signal processor, RVP8*. Helsinki, Finland, Vaisala Oyj.

Velasco-Forero, C. A., D. Sempere-Torres, E. F. Cassiraga, and J. J. Gómez-Hernández, 2009: A non-parametric automatic blending methodology to estimate rainfall fields from rain gauge and radar data. *Advances in Water Resources*, **32 (7)**, 986 – 1002.

Wallemacq, P., 2018: *Economic losses, poverty and disasters: 1998-2017*. Centre for Research on the Epidemiology of Disasters, CRED.

Weckwerth, T. M., J. Hanesiak, J. W. Wilson, S. B. Trier, S. K. Degelia, W. A. Gallus Jr, R. D. Roberts, and X. Wang, 2019: Nocturnal convection initiation during PECAN 2015. *Bulletin of the American Meteorological Society*, **100 (11)**, 2223–2239.

Weckwerth, T. M., C. R. Pettet, F. Fabry, S. J. Park, M. A. LeMone, and J. W. Wilson, 2005: Radar refractivity retrieval: Validation and application to short-term forecasting. *Journal of Applied Meteorology*, **44 (3)**, 285–300.

Weckwerth, T. M., and R. M. Wakimoto, 1992: The initiation and organization of convective cells atop a cold-air outflow boundary. *Monthly weather review*, **120 (10)**, 2169–2187.

Weisman, M. L., and R. Rotunno, 2000: The use of vertical wind shear versus helicity in interpreting supercell dynamics. *Journal of the atmospheric sciences*, **57 (9)**, 1452–1472.

Wilhelmson, R., 1974: The life cycle of a thunderstorm in three dimensions. *Journal of the Atmospheric Sciences*, **31 (6)**, 1629–1651.

Wilk, K., L. Lemon, and D. Burgess, 1979: Interpretation of radar echoes from severe thunderstorms: A series of illustrations with extended captions. *Prepared for training of FAA ARTCC Coordinators, National Severe Storms Laboratory.*

Wilks, D. S., 2011: *Statistical methods in the atmospheric sciences*, Vol. 100. Academic press.

Willoughby, H. E., E. Rappaport, and F. Marks, 2007: Hurricane forecasting: The state of the art. *Natural Hazards Review*, **8 (3)**, 45–49.

Wilson, J. W., 1966: *Movement and predictability of radar echoes*. US Department of Commerce, Environmental Science Services Administration.

Wilson, J. W., N. A. Crook, C. K. Mueller, J. Sun, and M. Dixon, 1998: Nowcasting thunderstorms: A status report. *Bulletin of the American Meteorological Society*, **79 (10)**, 2079–2100.

Wilson, J. W., E. E. Ebert, T. R. Saxen, R. D. Roberts, C. K. Mueller, M. Sleigh, C. E. Pierce, and A. Seed, 2004: Sydney 2000 forecast demonstration project: convective storm nowcasting. *Weather and forecasting*, **19 (1)**, 131–150.

Wilson, J. W., Y. Feng, M. Chen, and R. D. Roberts, 2010: Nowcasting challenges during the Beijing Olympics: Successes, failures, and implications for future nowcasting systems. *Weather and forecasting*, **25 (6)**, 1691–1714.

Witt, A., and J. Johnson, 1993: An enhanced storm cell identification and tracking algorithm. *Preprints, 26th Conf. on Radar Meteorology, Norman, OK, Amer. Meteor. Soc*, 141–143.

Witze, A., 2018: Argentina's mega-storms attract army of meteorologists. *Nature*, **563 (7730)**, 166–167.

W.M.O, 1992: *International Meteorological Vocabulary*. World Meteorological Organization, URL http://wmo.multitranstms.com/MultiTransWeb/Web.mvc.

Wurman, J., 1994: Vector winds from a single-transmitter bistatic dual-Doppler radar network. *Bulletin of the American Meteorological Society*, **75 (6)**, 983–994.

Wurman, J., S. Heckman, and D. Boccippio, 1993: A bistatic multiple-Doppler radar network. *Journal of Applied Meteorology*, **32 (12)**, 1802–1814.

Wurman, J., K. Kosiba, P. Markowski, Y. Richardson, D. Dowell, and P. Robinson, 2010: Finescale single-and dual-Doppler analysis of tornado intensification, maintenance, and dissipation in the Orleans, Nebraska, supercell. *Monthly Weather Review*, **138 (12)**, 4439–4455.

Yair, Y., B. Lynn, C. Price, V. Kotroni, K. Lagouvardos, E. Morin, A. Mugnai, and M. C. Llasat, 2010: Predicting the potential for lightning activity in Mediterranean storms based on the Weather Research and Forecasting (WRF) model dynamic and microphysical fields. *Journal of Geophysical Research: Atmospheres*, **115 (D4)**.

Yang, Y. H., and P. King, 2010: Investigating the potential of using radar echo reflectivity to nowcast cloud-to-ground lightning initiation over southern Ontario. *Weather and Forecasting*, **25 (4)**, 1235–1248.

Zhang, G., J. Vivekanandan, and E. Brandes, 2001: A method for estimating rain rate and drop size distribution from polarimetric radar measurements. *IEEE Transactions on Geoscience and Remote Sensing*, **39 (4)**, 830–841.

Zipser, E. J., and K. R. Lutz, 1994: The vertical profile of radar reflectivity of convective cells: A strong indicator of storm intensity and lightning probability? *Monthly Weather Review*, **122 (8)**, 1751–1759.